NOAA Project
Report

Development of two tsunami inundation maps and continuation of the meteotsunami characterization for the GOM

Final Report to the
National Tsunami Hazard Mitigation Program (NTHMP)
in Completion of Project Awards
NA19NWS4670015

Authors

Juan J Horrillo	Texas A&M University at Galveston
Wei Cheng	
Richards Sunny	
Alwin Jose	
Yuchen Shang	

Collaborators:
Brad Baker — Santa Rosa County Emergency Management Director

Under the guidance of
NTHMP Mapping and Modeling Subcommittee

National Tsunami Hazard Mitigation Program

National Oceanic and Atmospheric Administration

Ocean Engineering
Texas A&M University at Galveston
Galveston, Texas, 77553

November 2020

Contents

List of Figures

List of Tables

1 Executive Summary

Potential tsunami sources for the GOM are local submarine landslides, which have been examined in the past by the Atlantic and Gulf of Mexico Tsunami Hazard Assessment Group [ten Brink et al., 2009b]. In their findings, they stated that submarine landslides in the GOM are considered a potential tsunami hazard. However, the probability of such an event (tsunamis generated by large landslides) is low. The probability of occurrence is related to ancient (geological) massive landslides which were probably active prior to 7,000 years ago when large quantities of sediments were emptied into the Gulf of Mexico. Nowadays, sediment continues to empty into the Gulf of Mexico mainly from the Mississippi River. This sediment supply contributes to the slope steepening and the increase of fluid pore pressure in sediments, which may lead to further landslide activities and hence, the reason for this study in determining the potential tsunami hazard and its effects in the Gulf of Mexico.

For the triggering mechanism (tsunami generation) we use five geological sources, i.e., the Eastbreaks, Mississippi Canyon, West Florida landslides, and two Yucatán landslides introduced in [Horrillo et al., 2018]. A probabilistic approach was implemented in our previous study, see [Horrillo et al., 2015], to fill gaps along the continental shelf between the geological landslide sources by adding synthetic landslide sources (four in total) to cover the entire northern part of the GOM. Our probabilistic approach confirmed a recurrence period of major landslide events of around 8000 years, consistent with findings by [Geist et al., 2013].

These geological and probabilistic tsunami sources (nine in total) are used as the maximum credible events that could happen in the region according to the local bathymetry, seafloor slope, and sediment information. These credible events are then used to determine the inundation impact on selected communities along the GOM. The extent and magnitude of the tsunami inundation in those selected locations are achieved by using a combination of 3D and 2D coupled-numerical models. For instance, the 3D model, TSUNAMI3D, is used for tsunami generation to determine the initial dynamic wave or initial source and results are passed as an input to the 2D non-hydrostatic model, NEOWAVE, to determine the tsunami wave propagation and the detailed runup and inundation extent in each of the communities. Tsunami flooding inland-extent, maximum inundation water depth, momentum flux and direction, current velocity and vorticity can then be determined within the inundation-prone areas of the selected communities. Also, tsunami inundation and hurricane category flooding can be compared to access tsunami hazard in unmapped locations.

This project focused on the implementation of recent developments in the tsunami science recommended by the National Tsunami Hazard Mitigation Program - Modeling Mapping Subcommittee - Strategic Plan (NTHMP-MMS-SP) into our current Gulf of Mexico (GOM) tsunami mitigation products. Four main developments for tsunami mitigation have been created under this project for communities in the GOM that will provide guidance to state emergency managers for tsunami hazard mitigation and warning purposes.

The first is the development of tsunami inundation maps in Jamaica Beach, TX and South Tampa Bay, FL. Maximum tsunami inundation extent, water height, and momentum flux magnitude and direction are determined from each landslide sources, as well as the maximum of maximum inundation maps from all nine landslide sources. The two new

tsunami inundation map products add to the existing 12 mapped locations, which provide so far good coverage of the most populous coastal areas along the GOM.

The second is a continuing study of the comparison between existing SLOSH hurricane flooding data and our tsunami inundation result, in order to provide temporal-low-order estimate for tsunami hazard areas (community) where inundation studies have not yet been assigned/executed or where little bathymetric and elevation data exists. The adopted approach to define a quick estimate of tsunami vulnerability areas in the GOM has been taken from the existing hurricane storm surge flooding results along coastal areas, in which storm flooding map products are based on hurricane category. The existing storm surge flooding maps cover almost the entire GOM coastal regions and thus they are very well known among GOM regional emergency managers and other parties.

The third is to produce the velocity and vorticity magnitude maps for all the landslide scenarios, for Jamaica Beach, TX and South Tampa Bay, FL. Based on these maritime maps, location of strong currents and their damaging levels are identified. The tsunami hazard maritime products such as tsunami current magnitude, vorticity, safe/hazard zones would be central for future developments of maritime hazard maps, maritime emergency response and as well as infrastructure planning. We hope that the results herein may assist the maritime communities, port managers and other NTHMP's interested parties.

The fourth task is a continuation of the study to obtain an understanding of meteotsunami through the characterization of physical parameters in a specific region susceptible to meteotsunami in the GOM. The generation and propagation/amplification patterns of meteotsunami waves in eastern GOM are studied using maximum anomaly tracking, and coastal communities vulnerable to meteotsunami inundation are identified through a suite of idealized numerical experiments covering the entire eastern GOM, with parameters from different incident wave direction, forward speed and trajectory position.

Although the recurrence of destructive tsunami events have been verified to be quite low in the GOM, our work has confirmed that submarine landslide events with similar characteristics to those used here, have indeed the potential to cause severe damage to GOM coastal communities. Therefore, this work is intended to provide guidance to local emergency managers to help managing urban growth, evacuation planning, and public education with final objective to mitigate potential tsunami hazards in the GOM.

2 Introduction

2.1 Background

The U.S. Tsunami Warning System has included Gulf of Mexico (GOM) coasts since 2005 in order to enable local emergency management to act in response to tsunami warnings. To plan for the warning response, emergency managers must understand what specific areas within their jurisdictions are threatened by tsunamis. Coastal hazard areas susceptible to tsunami inundation can be determined by historical events, by modeling potential tsunami events (worst-case scenarios), or by using a probabilistic approach to determine the rate of recurrence or likelihood of exceeding a certain threshold. As the GOM coastal regions

have no significant recent historical tsunami records, numerical modeling and probabilistic methodologies for source identification must be used to determine coastal hazard zones.

Potential tsunami sources for the GOM are local submarine landslides [ten Brink et al., 2009b]; sources outside the GOM are considered a very low threat and may not significantly impact GOM coastal communities or infrastructure [Knight, 2006]. Although a massive tsunamigenic underwater landslide in the GOM is considered a potential hazard, the frequency of such events (though not well-constrained) is probably quite low based on historical evidence [Dunbar and Weaver, 2008] and available data on ages of failures which suggest they were probably active prior to 7,000 years ago when large quantities of sediments were emptied into the GOM [ten Brink et al., 2009b]. However, sediments continue to empty into the GOM, mainly from the Mississippi River, contributing to slope steepening and the increase of fluid pore pressure in sediments which may lead to unstable slopes that can be subsequently triggered to failure by seismic loading [Masson et al., 2006, ten Brink et al., 2009a, Dugan and Stigall, 2010, Harbitz et al., 2014]. In addition, the unique geometry of the GOM basin makes even unlikely tsunami events potentially hazardous to the entire Gulf Coast. Waves tend to refract along continental slopes; thus, given the curved geomorphology of the GOM shelf and the concave shape of the coastline, any outgoing tsunami wave could potentially affect the opposite coast in addition to the coast close to the landslide source.

Five large-scale geological submarine landslides with tsunamigenic potential have been identified within the GOM [ten Brink et al., 2009b, Chaytor et al., 2016], representing possible worst-case tsunami scenarios affecting GOM coasts in the past. In order to generate a more complete picture of landslide tsunami potential in the GOM, a probabilistic approach has been implemented to develop four additional synthetic landslide sources which fill gaps along the continental shelf between the geological landslide sources [Pampell-Manis et al., 2016]. These probabilistic tsunami sources are considered to be the maximum credible events that could happen in a particular region of the GOM according to the local bathymetry, seafloor slope, sediment information, and seismic loading. The probabilistic maximum credible events together with the geological sources form a suite of tsunami sources that have been used within coupled 3D and 2D numerical models to model tsunami generation and propagation throughout the GOM and to develop high-resolution inundation maps for the inundation-prone areas of two new communities along the Gulf Coast: Jamaica Beach, TX and South Tampa Bay, FL. These inundation studies showed that tsunamis triggered by massive submarine landslides have the potential to cause widespread and significant inundation of coastal cities. All of the 16 communities from both previous and current work and nine landslide sources are shown in Fig. 1.

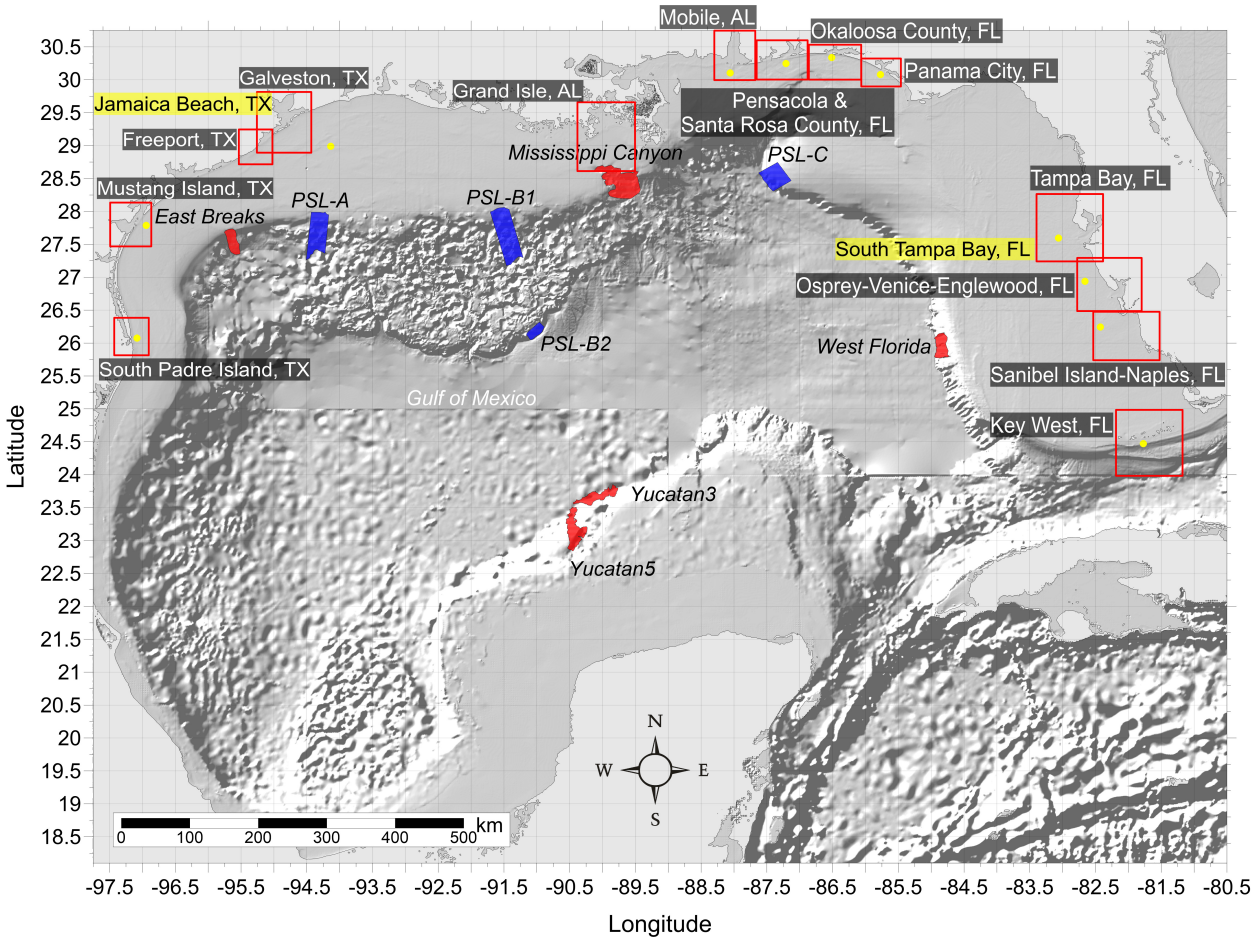

Figure 1: Selected communities or geography regions along the US GOM coastline where tsunami maps have been developed. Red rectangles denote 3 arcsecond (∼90m) domains of coastal communities where tsunami inundation has been modeled (highlighted South Tampa Bay, FL and Jamaica Beach, TX are developed in the current project); red hatched areas are geological landslide sources; blue hatched areas are Probabilistic Submarine Landslide (PSL) sources; yellow dots are locations of numerical wave gauges. The zero-meter elevation contour is drawn to show the GOM coastline.

While high-resolution tsunami inundation studies have been completed for these 16 communities and are planned for additional locations, vulnerability assessments are still essential for coastal locations where inundation studies have not yet been performed or planned, or where there is a lack of high-resolution bathymetric and/or elevation data. Therefore, we aim to extend the results of the completed mapping studies in order to provide estimates of tsunami inundation zones for hazard mitigation efforts in unmapped locations. Inundation maps with even low resolution are useful to emergency managers to create first-order evacuation maps, and some methods currently exist to provide low-resolution estimates of hazard zones for regions which do not currently have or warrant high-resolution maps. For example, guidance given by the National Tsunami Hazard Mitigation Program (NTHMP) Mapping and Modeling Subcommittee in "Guidelines and Best Practices to Establish Areas of Tsunami Inundation for Non-modeled or Low-hazard Regions" (available from `https://nws.weather.gov/nthmp/documents/3nonmodeledregionguidelines.pdf`) recommends that coastal areas and areas along ocean-connected waterways that are below 10 m (33 ft) elevation are at risk for most tsunamis, and rare and large tsunamis may inundate above this elevation. However, in low-lying coastal regions such as along the Gulf Coast, the 10 m (33 ft) elevation contour is too far inland to be reasonably applicable for estimating potential tsunami inundation zones. The guidance additionally suggests that low-lying areas are prone to inundation within 3 km (1.9 mi) inland for locally-generated tsunamis and within 2 km (1.3 mi) inland for distant sources. While these distances may be reasonable for some regions of the Gulf Coast, prevalent bathymetric and topographic features such as barrier islands/peninsulas complicate the method of delineating inundation-prone areas based on distance from the shoreline. As a result, the purpose of the current work is to improve the methodology which compares modeled tsunami inundation to modeled/predicted hurricane storm surge. Specifically, we aim to identify the hurricane category which produces modeled maximum storm surge that best approximates the maximum tsunami inundation in the two new locations modeled in this project. Even though many physical aspects of storm surge inundation are completely different from those of tsunamis (time scale, triggering mechanism, inundation process, etc.), good agreement or clear trends between tsunami and storm surge flooding on a regional scale can be used to provide first-order estimates of potential tsunami inundation in communities where detailed inundation maps have not yet been developed or are not possible due to unavailability of high-resolution bathymetry/elevation data. Additionally, since tsunamis are not well-understood as a threat along the Gulf Coast, while hurricane hazards are well-known, this method of predicting tsunami inundation from storm surge provides a way for GOM emergency managers to better prepare for potential tsunami events based on more understandable and accessible information. This hurricane-tsunami comparison was first carried out in Horrillo et al. [2016] (award number NA14NWS4670049) where five previously mapped locations were studied, namely South Padre Island, TX, Galveston, TX, Mobile, AL, Panama City, FL, and Tampa, FL; then as a regular procedure for all the newly mapped locations during the following mapping projects.

Recent tsunamis have shown that the maritime community requires additional information and guidance about tsunami hazards and post-tsunami recovery [Wilson et al., 2012, 2013]. To accomplish mapping and modeling activities to meet NTHMP's planning/response purposes for the maritime community and port emergency management and other customer

requirements, it is necessary to continue the process to include maritime products in our current inundation map development. These activities will include tsunami hazard maritime products generated by GOM's tsunami sources (submarine landslides) that may impact specifically ship channels, bay inlets, harbors, marinas, and oil infrastructures (e.g., designated lightering and oil tanker waiting zones), which has already been applied in other tsunami risk regions, e.g., California, Oregon and Washington. It is worth noting that Galveston was the first city where we implemented the maritime products [Horrillo et al., 2016]. South Padre Island, TX, Mobile, AL, Panama City, FL, and Tampa, FL, Pensacola, FL, Key West, FL, Okaloosa County, FL, Santa Rosa County, FL and Mustang Island, TX, were implemented in project NA15NWS4670031 and NA16NWS4670039 [Horrillo et al., 2017], and then as a regular procedure for all the newly mapped locations during the following mapping projects.

2.2 Regional and Historical Context

Jamaica Beach, TX

Jamaica Beach is a small city on western Galveston Island, surrounded by Galveston City both to the west and east, and the West Bay and the GOM to the north and south. According to 2010 census, Jamaica Beach's population was 983. In this study, the finest grid (1/3 arcsecond) extends further west to Sun Bay Dr., and east to approximately Sydnor Bayou on the Galveston Island, as well as all three Deer Islands, Tiki Island and Flamingo Isles north of the bay. Jamaica Beach study area can be accessed via San Luis Pass from the San Luis Pass Island west of the bay, and from Galveston Island to the east and hence I-45 from the mainland. This area joins the Freeport and Galveston inundation mapping areas modeled from previous studies [Horrillo et al., 2016, 2019] in providing a seamless inundation map coverage from Freeport to Galveston.

Hurricane Ike was a Category 4 hurricane before it made landfall first over eastern Cuba on September 8, 2008. The hurricane weakened but then picked up intensity to become Category 2 before making its second landfall on Galveston, TX. Though at Category 2 near Texas, Hurricane Ike created in storm surge (about 5 m) in Galveston (including Jamaica Beach) comparable to Category 5 hurricanes. As a result, Ike caused upwards of $37 billion damage and 160 deaths (directly and indirectly) across Texas, Cuba and Bahamas, etc. Several houses in Jamaica Beach were flooded. The Blue Water Highway connecting San Luis Pass was also severely damaged making it impassible.

South Tampa Bay, FL

In this study, the South Tampa Bay 1/3 arcsecond computational domain encompasses the barrier islands south of Tampa Bay, FL: Anna Maria Island, Longboat Key, Lido Key and north Siesta Key, and extends much further inland to account for potential flooding near the bays and channels. The study areas belong to the Manatee and Sarasota counties, and are adjacent to Osprey-Venice inundation mapping area modeled from previous study [Horrillo et al., 2018]. Anna Maria Island is connected to the mainland via Anna Maria

Island Bridge (Manatee Ave) and Cortez Bridge (Cortez Rd W), and to Longboad Key via Gulf Mexico Dr.(SR 789). While there is no direct road access from the mainland, Longboat Key is adjacent to Lido Key (via John Ringling Pkwy bridge), which is accessible to the mainland via John Ringling Causeway. Unlike the other islands, Siesta Key is not connected from Lido Key, instead it is accessible from the mainland via Siesta Dr to the north and Stickney Point Rd to the south. East of the barrier island system, the back bay becomes gradually narrower from the Tampa bay in the north to Sarasota Bay and Roberts Bay in the south. Sarasota-Bradenton International Airport is the closest airport, which is located across Sarasota bay on SH 41. According to 2005 census, the three cities, Anna Maria, Holmes Beach and Bradenton Beach, recorded a combined population of 8,500. The town of Longboat Key has a population of 6,888 and Siesta Key 6,565, according to the 2010 census.

Florida is frequented by hurricanes due to its unique location and long coastlines. Our study location in southwestern Florida is no exception. This area has been visited by many major hurricanes, and recent ones are briefly summarized as follows. Hurricane Irma became category 4 when it landed Florida in 2017, down from category 5 when it first hit Cuba, which greatly reduced the damage. Nonetheless, Irma still remains as one of the costliest storms in the history of Florida. Wind from Hurricane Irma damaged many homes and uprooted and knocked over trees, and caused power outage to Manatee County and Sarasota County. The last major hurricane that hit Florida before Irma was Hurricane Wilma which made landfall in Collier County, FL on October 24, 2005. Mandatory evacuations were ordered for Collier County residents southwest of US 41. The peak of storm surge occurred in the Naples area, and the Naples Airport was damaged significantly. Charlotte and Manatee only suffered minor damage from Wilma. Hurricane Charley, a category 4 hurricane, made landfall in southwest Florida in mid-August, 2004, and caused ten deaths and severe damage to buildings and crops, making it the second costliest hurricane at the time. Southwestern Florida, including Sarasota and Charlotte County, has seen the most severe damage. Other major hurricanes that have made landfall in Florida but did not make much impact in southwestern Florida include Hurricane Ivan in 2004, Hurricane Dennis in 2005.

2.3 Summary

Although the probability of a large-scale tsunami event in the GOM is low, this and previous studies have indicated that tsunami events with characteristics similar to those detailed in Horrillo et al. [2015] have the potential to cause severe flooding and damage to GOM coastal communities that is similar to or even greater than that seen from major hurricanes, particularly in open beach and barrier island regions. Tsunami hazard maritime products such as tsunami current magnitude, vorticity, safe/hazard zones would be central for future developments of maritime hazard maps, maritime emergency response as well as infrastructure planning. The results of this work are intended to provide guidance to local emergency managers to help with managing urban growth, evacuation planning, and public education with the vision to mitigate potential GOM tsunami hazards.

This report is organized as follows. Section 3 briefly describes all 9 landslide sources used for tsunami modeling (3.1) and the numerical models used for simulations (3.2). Section 4 covers the inundation and momentum flux maps for Jamaica Beach, TX and South Tampa

Bay, FL. The comparison between tsunami inundation and hurricane storm surge inundation is given in Section 5 for the two new Gulf Coast communities. Current velocity and vorticity maps are described in Section 6 for the two new communities. Section 7 presents numerical results for a meteotsunami parameter study of eastern GOM/Florida gulf coast, with analysis on generation and propagation/amplification patterns of meteotsunami waves and identification of coastal communities vulnerable to meteotsunami inundation. Concluding remarks on general trends seen among the communities and practical applications for other regions are given in Section 8.

3 Tsunami Inundation Modeling

3.1 Landslide Tsunami Sources

Nine large-scale landslide configurations were created assuming an unstable (gravity-driven) sediment deposit condition. Five of these landslide configurations are geological events identified by ten Brink et al. [2009b]: the Eastbreaks, Mississippi Canyon, and West Florida submarine landslides; and Chaytor et al. [2016]: the Yucatán #3 and Yucatán #5 landslides, which are shown as red hatched regions in Fig. 1. The Yucatán Shelf/Campeche Escarpment was the last remaining area of the GOM that had not been evaluated for landslide tsunami hazards, until high-resolution mapping data collected in 2013 [Paull et al., 2014] shows that the Yucatan Shelf/Campeche Escarpment margin has been subjected to intense modifications by Cenozoic mass wasting processes. Although no known tsunami events have been linked to these Yucatan sources, numerical modeling result shows that they are capable of generating tsunamis that could propagate throughout the GOM Basin [Chaytor et al., 2016]. The other four were obtained using a probabilistic methodology based on work by Maretzki et al. [2007] and Grilli et al. [2009] and extended for the GOM by Pampell-Manis et al. [2016]. The probabilistic landslide configurations were determined based on distributions of previous GOM submarine landslide dimensions through a Monte Carlo Simulation (MCS) approach. The MCS methodology incorporates a statistical correlation method for capturing trends seen in observational data for landslide size parameters while still allowing for randomness in the generated landslide dimensions. Slope stability analyses are performed for the MCS-generated trial landslide configurations using landslide and sediment properties and regional seismic loading (Peak Horizontal ground Acceleration, PHA) to determine landslide configurations which fail and produce a tsunami. The probability of each tsunamigenic failure is calculated based on the joint probability of the earthquake PHA and the probability that the trial landslide fails and produces a tsunami wave above a certain threshold. Those failures which produce the largest tsunami amplitude and have the highest probability of occurrence are deemed the most extreme probabilistic events, and the dimensions of these events are averaged to determine maximum credible probabilistic sources. The four maximum credible Probabilistic Submarine Landslides (PSLs) used as tsunami sources for this study are termed PSL-A, PSL-B1, PSL-B2, and PSL-C and are shown as blue hatched regions in Fig. 1. For a more complete discussion of GOM submarine landslide sources, the reader can consult Horrillo et al. [2015, 2018], Pampell-Manis et al. [2016].

Table 1: Submarine Landslide general information.

Submarine Landslide	Location (Lon, Lat)	Age/Recurrence (Years)	Area (km^2)	Volume (km^3)	Excavation Depth (m)	Modeled Volume (km^3)
East Breaks	-95.68, 27.70	$\sim 10000 - 25000$	~ 519.52	~ 21.95	~ 160	26.7
Mississippi	-90.00, 28.60	$\sim 7500 - 11000$	~ 3687.26	~ 425.54	~ 300	425
West Florida	-84.75, 25.95	> 10000	~ 647.57	~ 16.2	~ 150	18.4
Yucatan #3	-90.07, 23.00	–	~ 578	~ 38	~ 278	39.3
Yucatan #5	-89.80, 23.54	–	~ 1094	~ 70.2	~ 385	69.5
PSL-A	-94.30, 27.98	$\sim 7700 - 7800$	~ 1686	~ 57	~ 67	58
PSL-B1	-91.56, 28.05	$\sim 5400 - 5500$	~ 3118	~ 69	~ 44	57.3
PSL-B2	-91.01, 26.17	$\sim 4700 - 4800$	~ 282	~ 45	~ 323	68
PSL-C	-87.20, 28.62	$\sim 550 - 650$	~ 1529	~ 315	~ 404	357

3.2 Numerical Models

For the nine landslide tsunami sources considered here, tsunami wave development and subsequent propagation and inundation of coastal communities was modeled using coupled 3D and 2D numerical models [Horrillo et al., 2015]. The tsunami generation phase was modeled using the 3D model TSUNAMI3D [Horrillo, 2006, Horrillo et al., 2013], which solves the finite difference approximation of the full Navier-Stokes equations and the incompressibility (continuity) equation. Water and landslide material are represented as Newtonian fluids with different densities, and the landslide-water and water-air interfaces are tracked using the Volume of Fluid (VOF) method of Hirt and Nichols [1981], which is simplified to account for the large horizontal/vertical aspect ratio of the tsunami wave and the selected computational cell size required to construct an efficient 3D grid. The pressure term is split into hydrostatic and non-hydrostatic components. Although TSUNAMI3D has the capability of variable grids, the nesting capability necessary for modeling detailed inundation of coastal regions is too computationally intensive within the fully 3D model; thus, detailed inundation modeling is achieved by coupling the 3D model to a 2D model. Once the tsunami wave generated by the 3D model is fully developed, the wave is passed as an initial condition to the 2D model for modeling wave propagation and coastal inundation. The generated wave is considered fully developed when the total wave energy (potential plus kinetic) reaches a maximum and before the wave leaves the computational domain, as discussed in López-Venegas et al. [2015]. The 2D model used here is NEOWAVE [Yamazaki et al., 2008], a depth-integrated and non-hydrostatic model built on the nonlinear shallow water equations which includes a momentum-conserved advection scheme to model wave breaking and two-way nested grids for modeling higher-resolution wave runup and inundation. Propagation and inundation are calculated via a series of nested grids of increasing resolution, from 15 arcsecond (450 m) resolution for a domain encompassing the entire northern GOM (Fig. 1), to finer resolutions of 3 arcseconds (90 m, from NOAA NCEI Coastal Relief Models), 1 arcsecond (30 m), and 1/3 arcsecond (10 m, from NOAA NCEI Tsunami Inundation Digital Elevation Models [DEMs]) to model detailed inundation of the most populated/ inundation-prone areas of each coastal community. The 3 arcsecond (90 m) subdomains encompassing each coastal community studied here are shown by red rectangles in Fig. 1.

4 Tsunami Maps

Tsunami inundation depth and extent has been modeled for two selected coastal communities: Jamaica Beach, TX and South Tampa Bay, FL. Inundation (flooding) is determined by subtracting land elevation from water elevation, and elevations used are in reference to the Mean High Water (MHW) tidal datum. For this study, the tsunami inundation depth/extent modeled for each community is the maximum-of-maximums (MOM) inundation, which is calculated as the maximum inundation depth from an ensemble of inundation depths produced by each of the nine tsunami sources considered. That is, once inundation in a community has been modeled for each of the nine sources, the overall maximum inundation depth in each computational grid cell is taken as the MOM tsunami inundation in that cell. This approach gives a worst-case scenario of estimated tsunami inundation for each coastal community.

In this section, the numerical results (inundation and momentum flux maps) for each landslide source are presented for Jamaica Beach, TX and South Tampa Bay, FL. The MOM inundation map from all sources and the maximum inundation map by source are also shown. A summary table of each location's numerical gauge (at an approximate water depth of 20 m) shows maximum wave amplitude and arrival time after each landslide failure.

It is worth noting, however, that for both communities, the MOM tsunami inundation is produced solely by the Mississippi Canyon submarine landslide failure. That geological failure is the largest in both area and volume of material removed, and therefore produces the highest amplitude wave of all sources simulated.

4.1 Jamaica Beach, TX

Table 2: Maximum tsunami wave amplitude and corresponding arrival time after landslide failure at Jamaica Beach, TX numerical wave gauge: 28°59'16.32"N, 94°8'8.89"W (Fig. 1), approximate water depth 18 m.

Tsunami Source	Maximum Wave Amplitude (m)	Arrival Time After Landslide Failure (hr)
East Breaks	1.86	1.9
PSL-A	1.88	1.2
PSL-B1	1.96	2.0
PSL-B2	0.64	2.4
Mississippi Canyon	4.08	2.5
PSL-C	3.47	3.1
West Florida	0.53	3.5
Yucatán #3	1.47	2.8
Yucatán #5	1.51	2.7

Jamaica Beach, TX
East Breaks submarine landslide
Maximum Momentum Flux

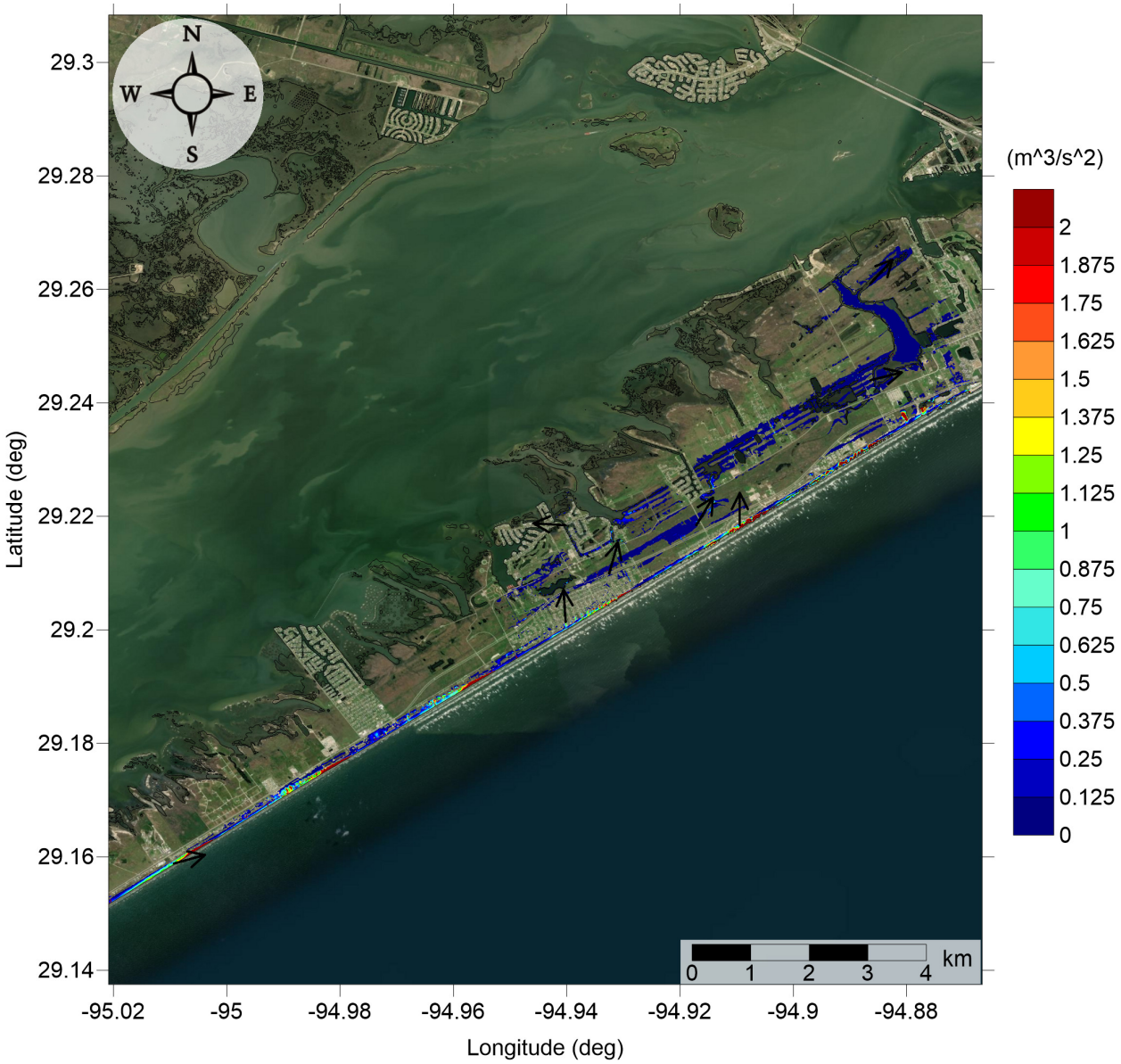

Figure 2: Maximum momentum flux (m^3/s^2) caused by the East Breaks submarine landslide in Jamaica Beach, TX. Arrows represent direction of maximum momentum flux. Contour drawn is the zero-meter contour for land elevation.

Jamaica Beach, TX
East Breaks submarine landslide
Maximum Inundation Depth

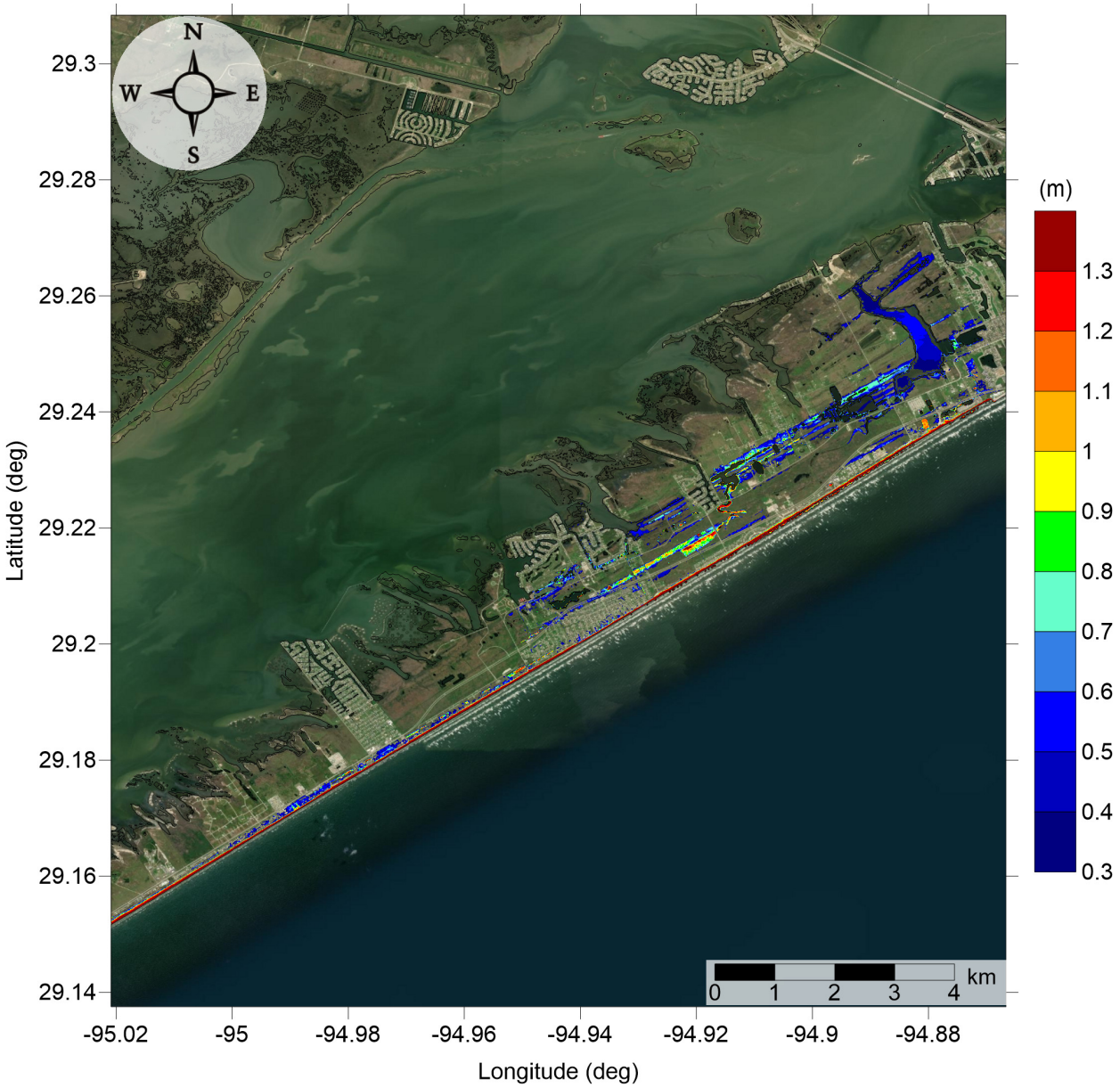

Figure 3: Maximum inundation depth (m) caused by the East Breaks submarine landslide in Jamaica Beach, TX. Contour drawn is the zero-meter contour for land elevation.

Jamaica Beach, TX
Probabilistic Submarine Landslide A
Maximum Momentum Flux

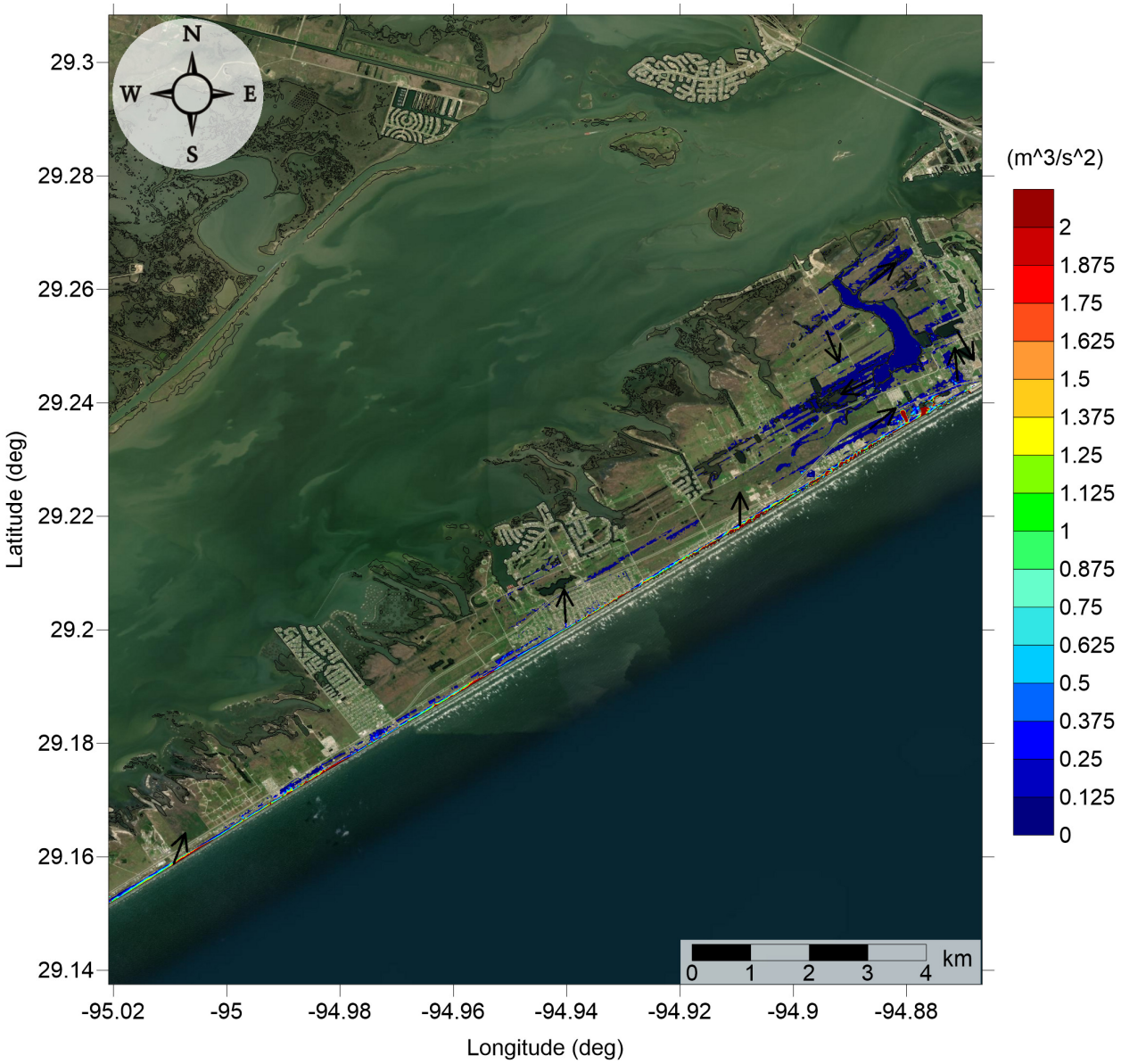

Figure 4: Maximum momentum flux (m^3/s^2) caused by the Probabilistic Submarine Landslide A in Jamaica Beach, TX. Arrows represent direction of maximum momentum flux. Contour drawn is the zero-meter contour for land elevation.

Jamaica Beach, TX
Probabilistic Submarine Landslide A
Maximum Inundation Depth

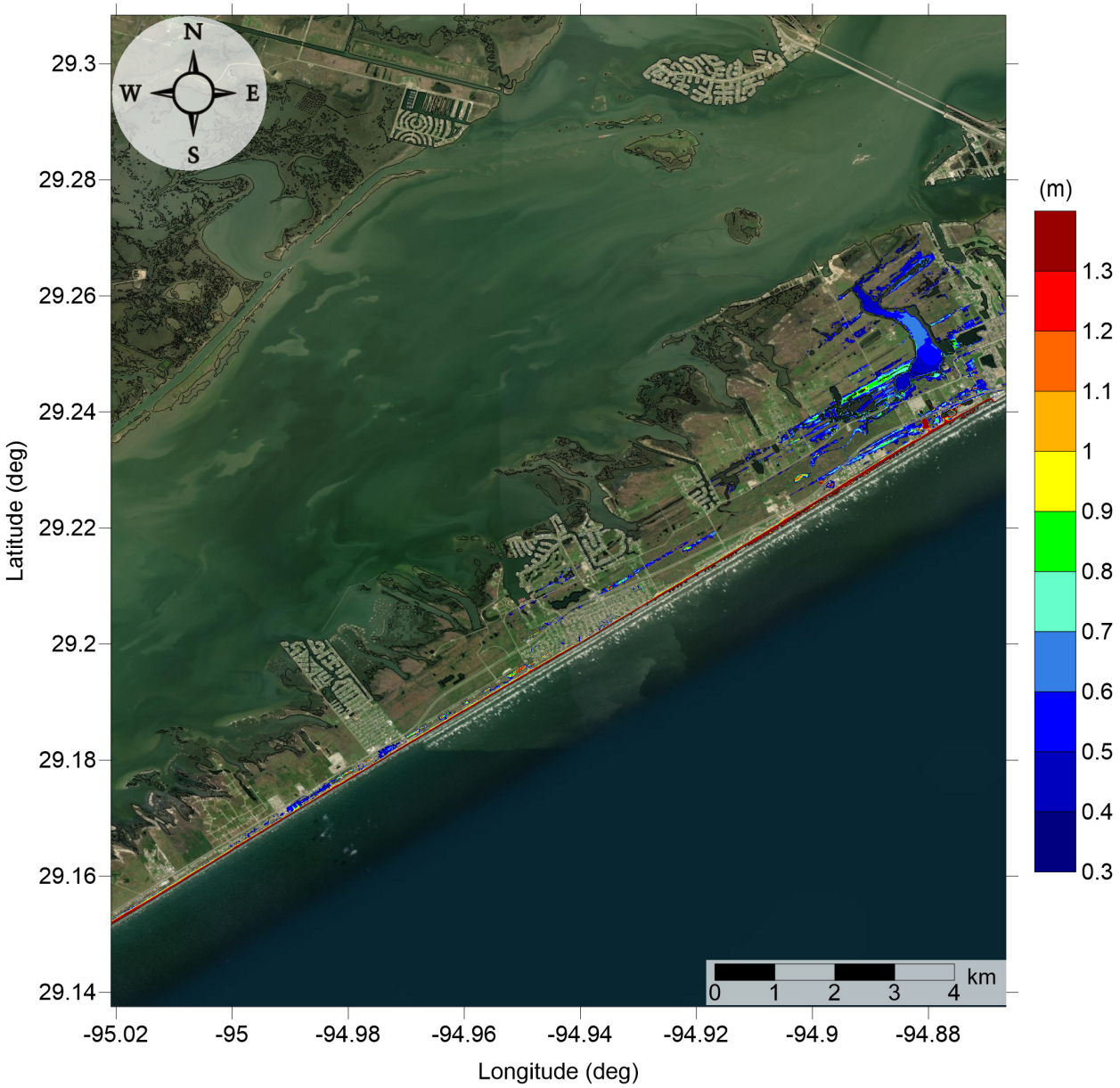

Figure 5: Maximum inundation depth (m) caused by the Probabilistic Submarine Landslide A in Jamaica Beach, TX. Contour drawn is the zero-meter contour for land elevation.

Jamaica Beach, TX
Probabilistic Submarine Landslide B1
Maximum Momentum Flux

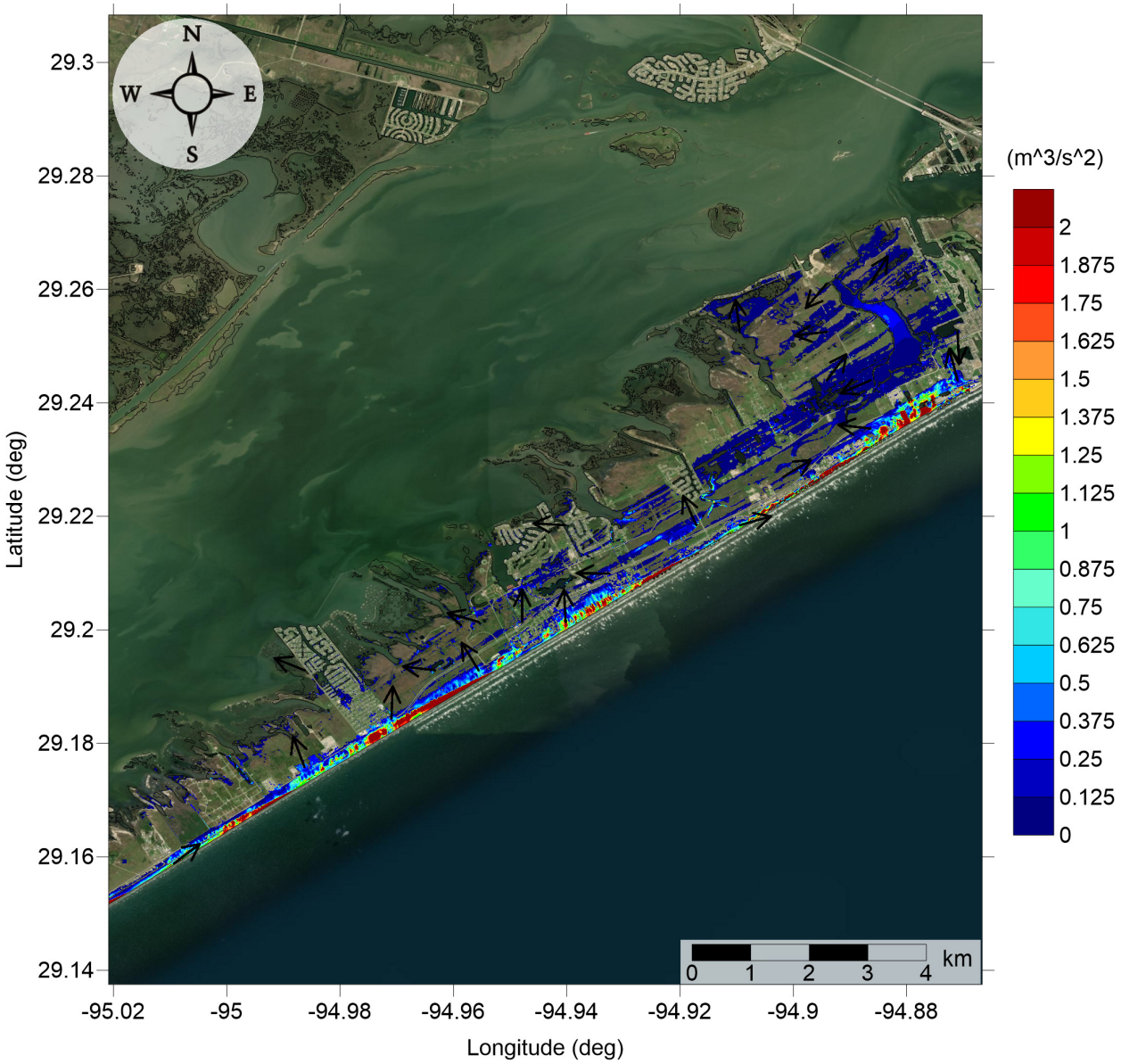

Figure 6: Maximum momentum flux (m^3/s^2) caused by the Probabilistic Submarine Landslide B1 in Jamaica Beach, TX. Arrows represent direction of maximum momentum flux. Contour drawn is the zero-meter contour for land elevation.

Jamaica Beach, TX
Probabilistic Submarine Landslide B1
Maximum Inundation Depth

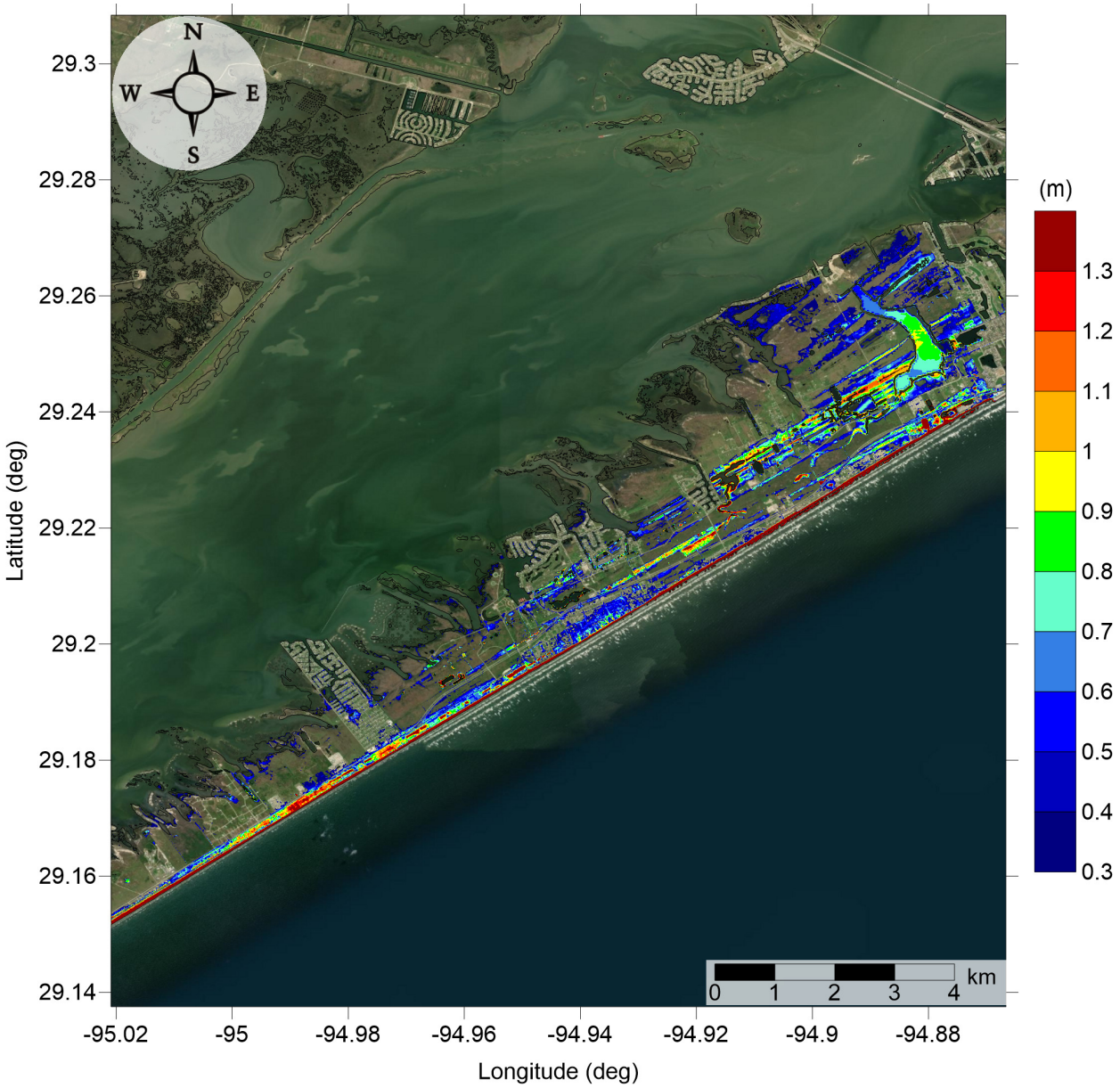

Figure 7: Maximum inundation depth (m) caused by the Probabilistic Submarine Landslide B1 in Jamaica Beach, TX. Contour drawn is the zero-meter contour for land elevation.

Jamaica Beach, TX
Probabilistic Submarine Landslide B2
Maximum Momentum Flux

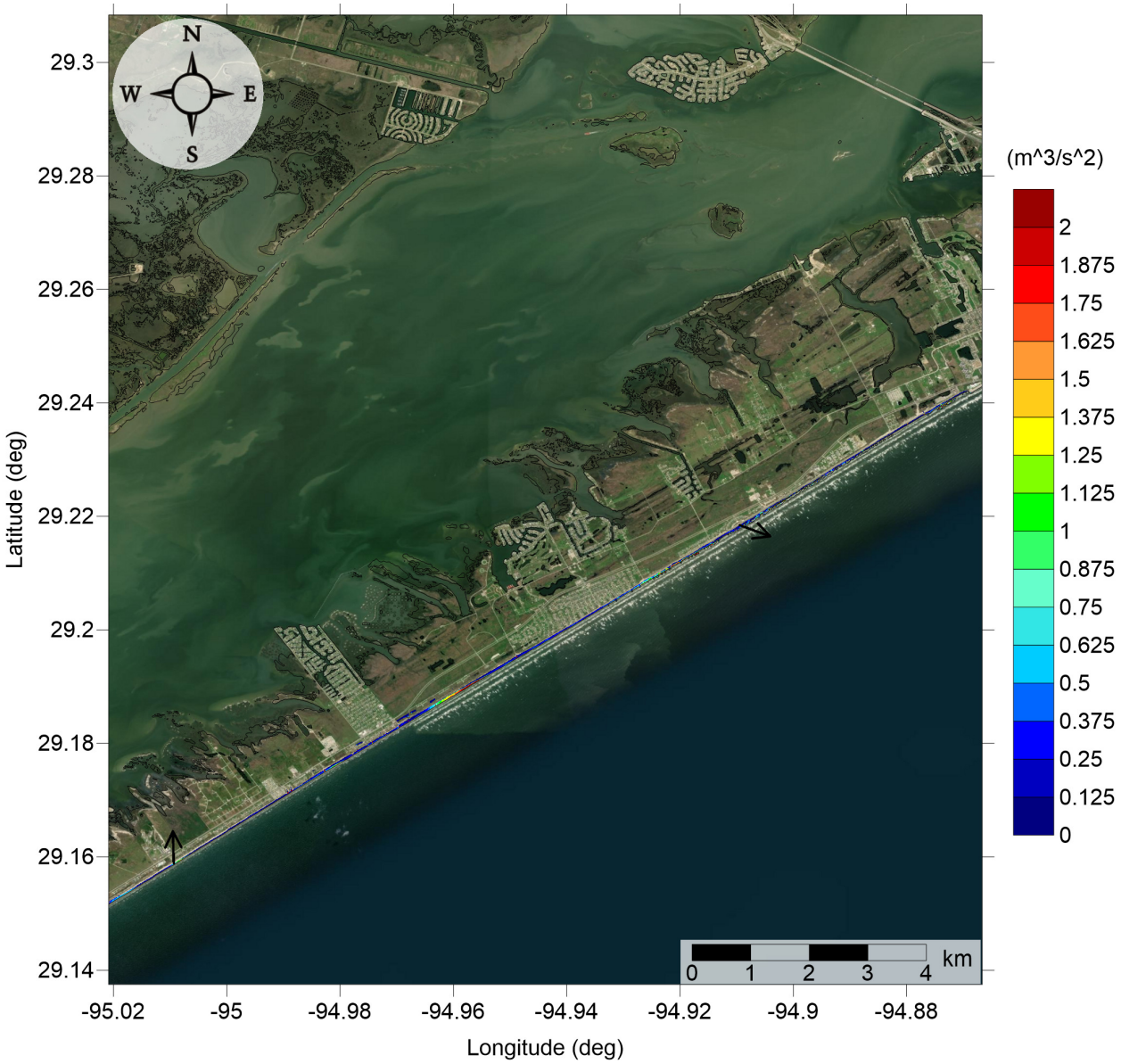

Figure 8: Maximum momentum flux (m^3/s^2) caused by the Probabilistic Submarine Landslide B2 in Jamaica Beach, TX. Arrows represent direction of maximum momentum flux. Contour drawn is the zero-meter contour for land elevation.

Jamaica Beach, TX
Probabilistic Submarine Landslide B2
Maximum Inundation Depth

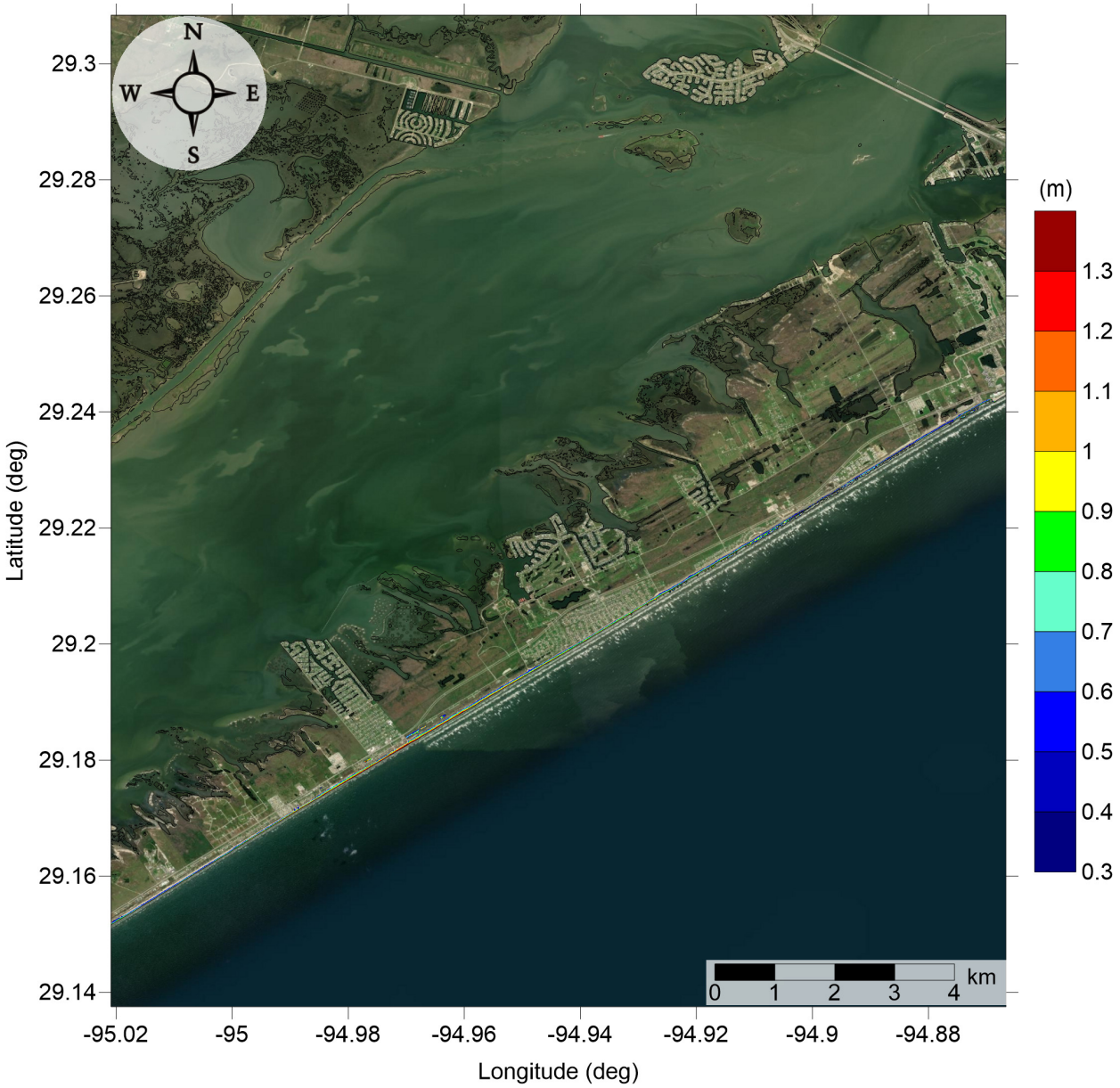

Figure 9: Maximum inundation depth (m) caused by the Probabilistic Submarine Landslide B2 in Jamaica Beach, TX. Contour drawn is the zero-meter contour for land elevation.

Jamaica Beach, TX
Mississippi Canyon submarine landslide
Maximum Momentum Flux

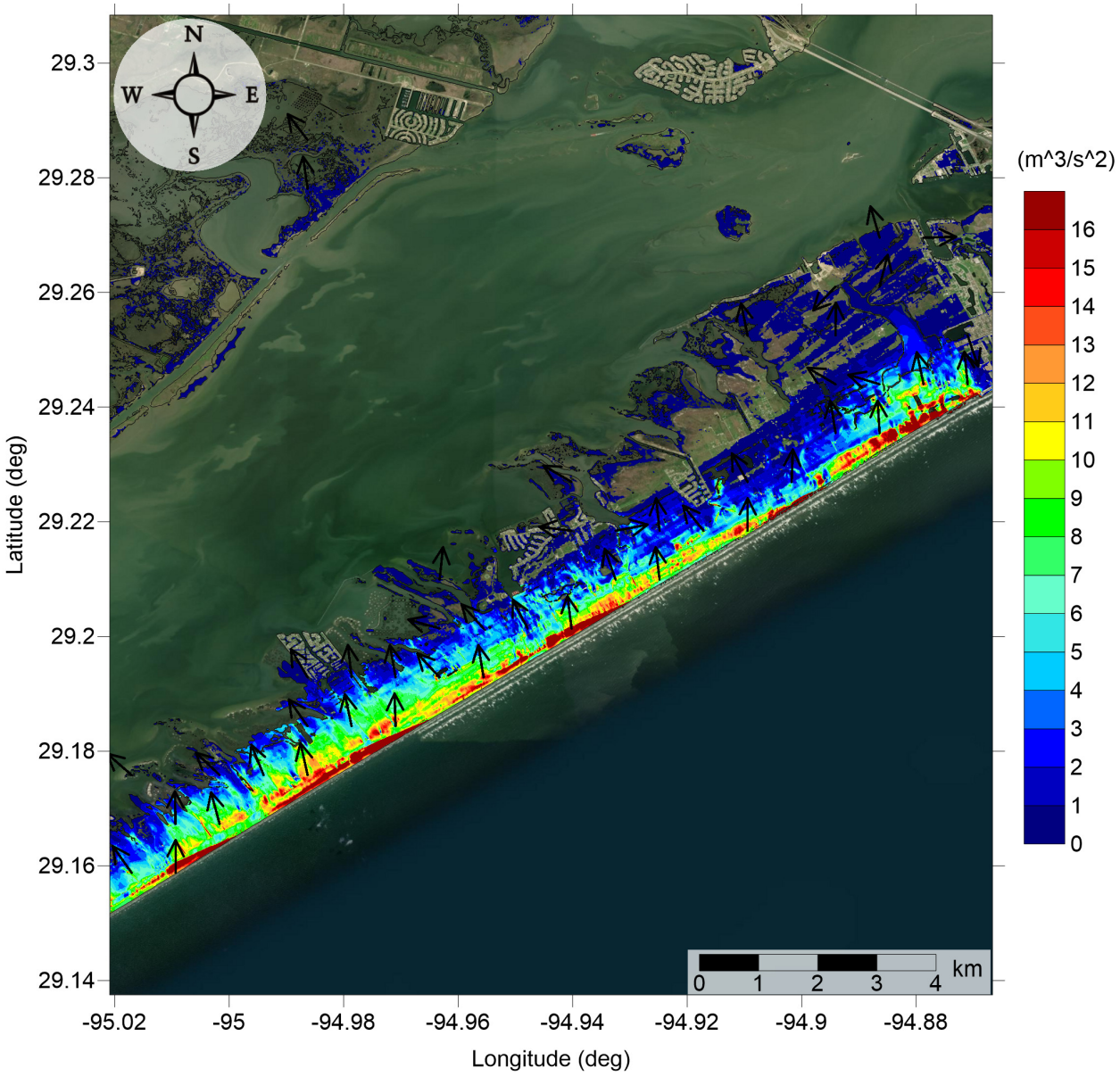

Figure 10: Maximum momentum flux (m^3/s^2) caused by the Mississippi Canyon submarine landslide in Jamaica Beach, TX. Arrows represent direction of maximum momentum flux. Contour drawn is the zero-meter contour for land elevation.

Jamaica Beach, TX
Mississippi Canyon submarine landslide
Maximum Inundation Depth

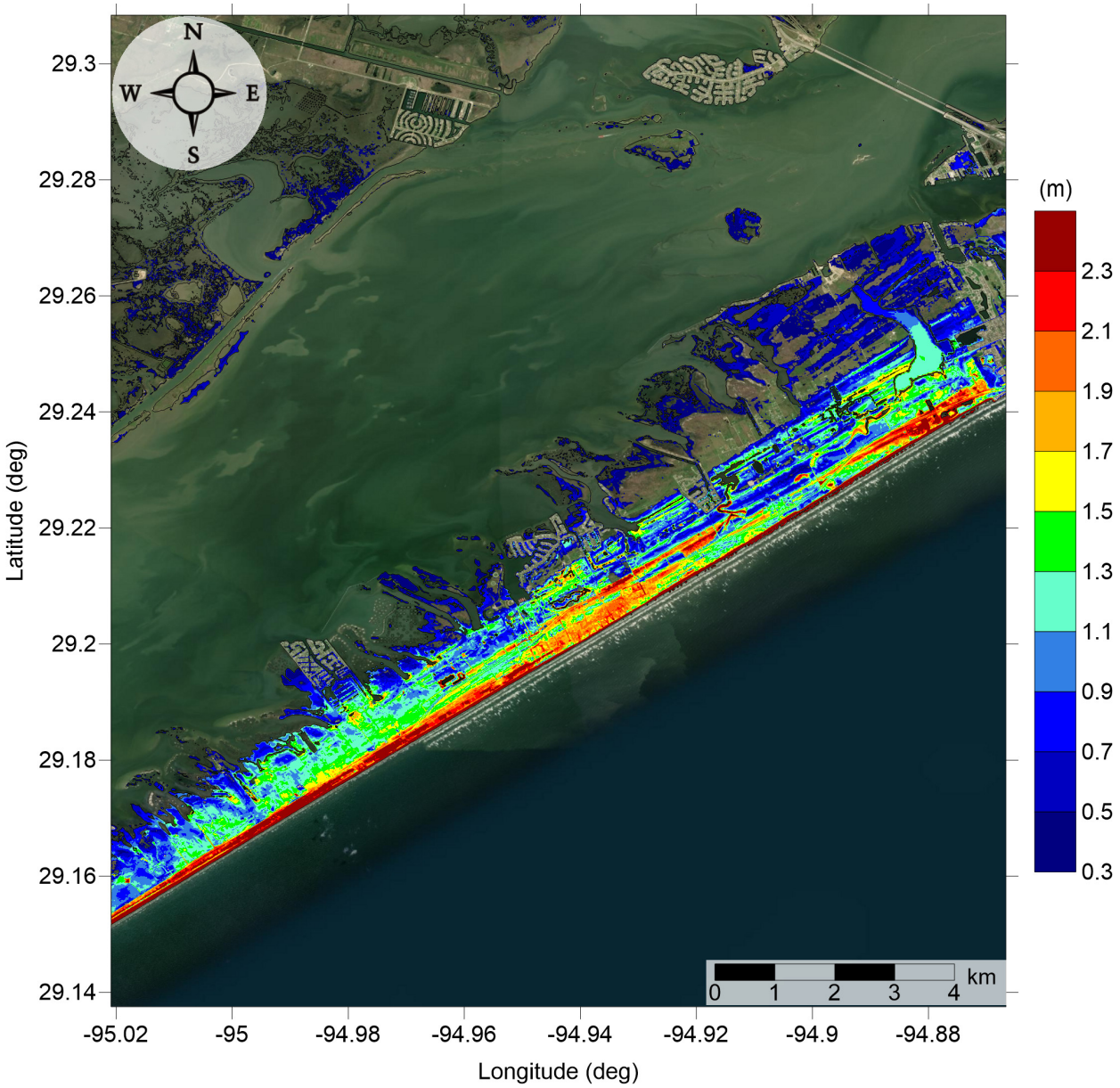

Figure 11: Maximum inundation depth (m) caused by the Mississippi Canyon submarine landslide in Jamaica Beach, TX. Contour drawn is the zero-meter contour for land elevation.

Jamaica Beach, TX
Probabilistic Submarine Landslide C
Maximum Momentum Flux

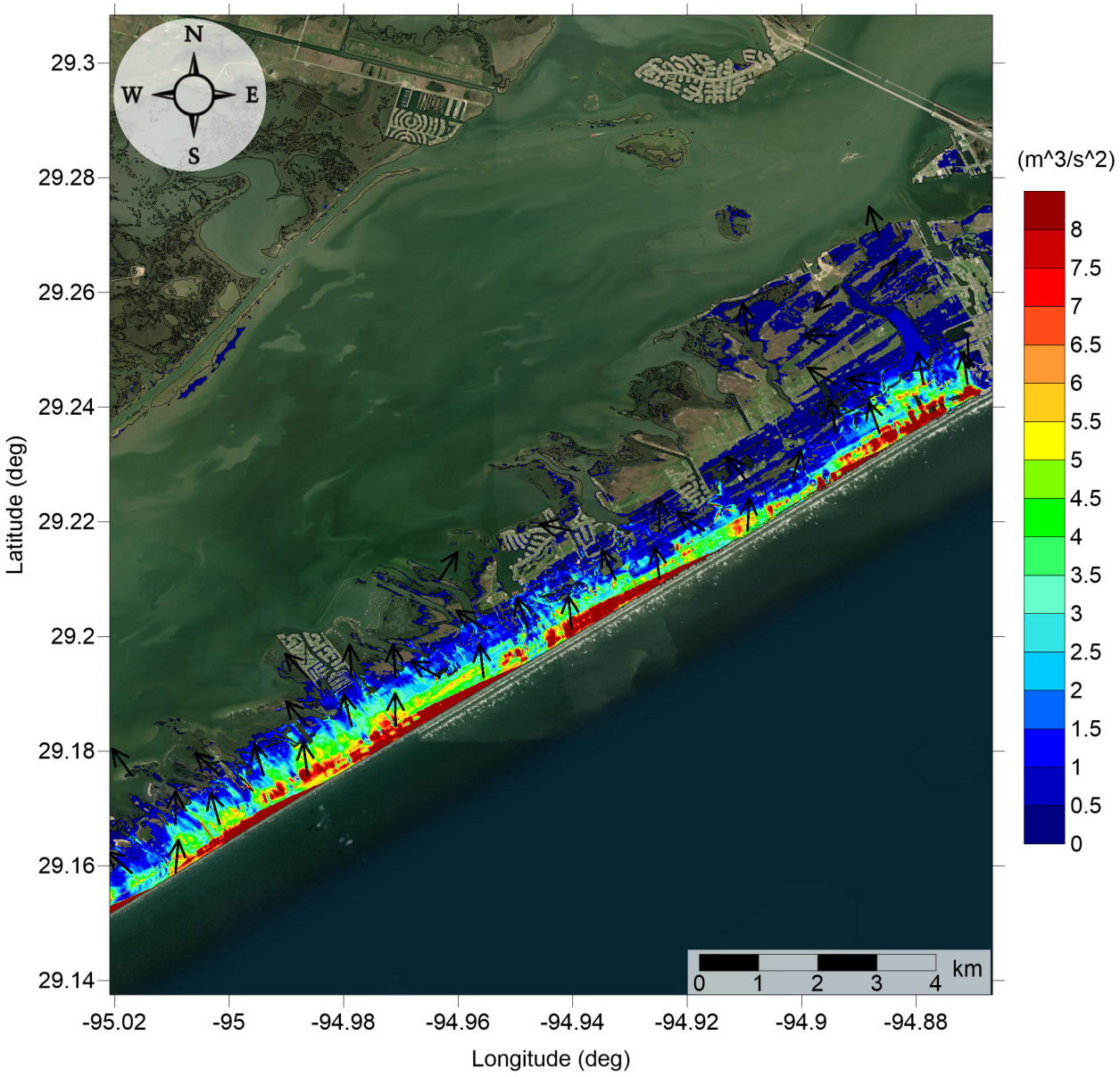

Figure 12: Maximum momentum flux (m^3/s^2) caused by the Probabilistic Submarine Landslide C in Jamaica Beach, TX. Arrows represent direction of maximum momentum flux. Contour drawn is the zero-meter contour for land elevation.

Jamaica Beach, TX
Probabilistic Submarine Landslide C
Maximum Inundation Depth

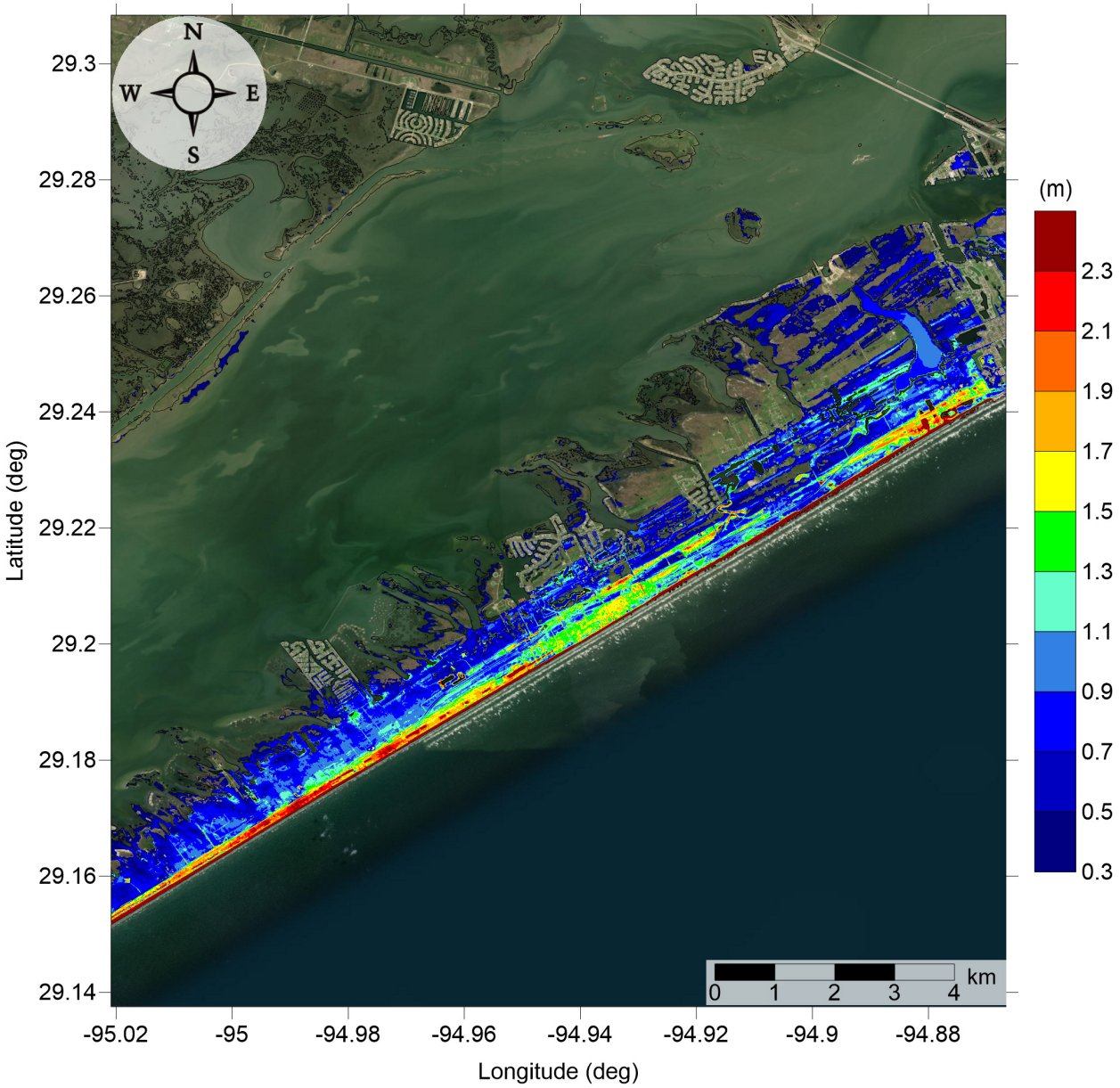

Figure 13: Maximum inundation depth (m) caused by the Probabilistic Submarine Landslide C in Jamaica Beach, TX. Contour drawn is the zero-meter contour for land elevation.

Jamaica Beach, TX
West Florida submarine landslide
Maximum Momentum Flux

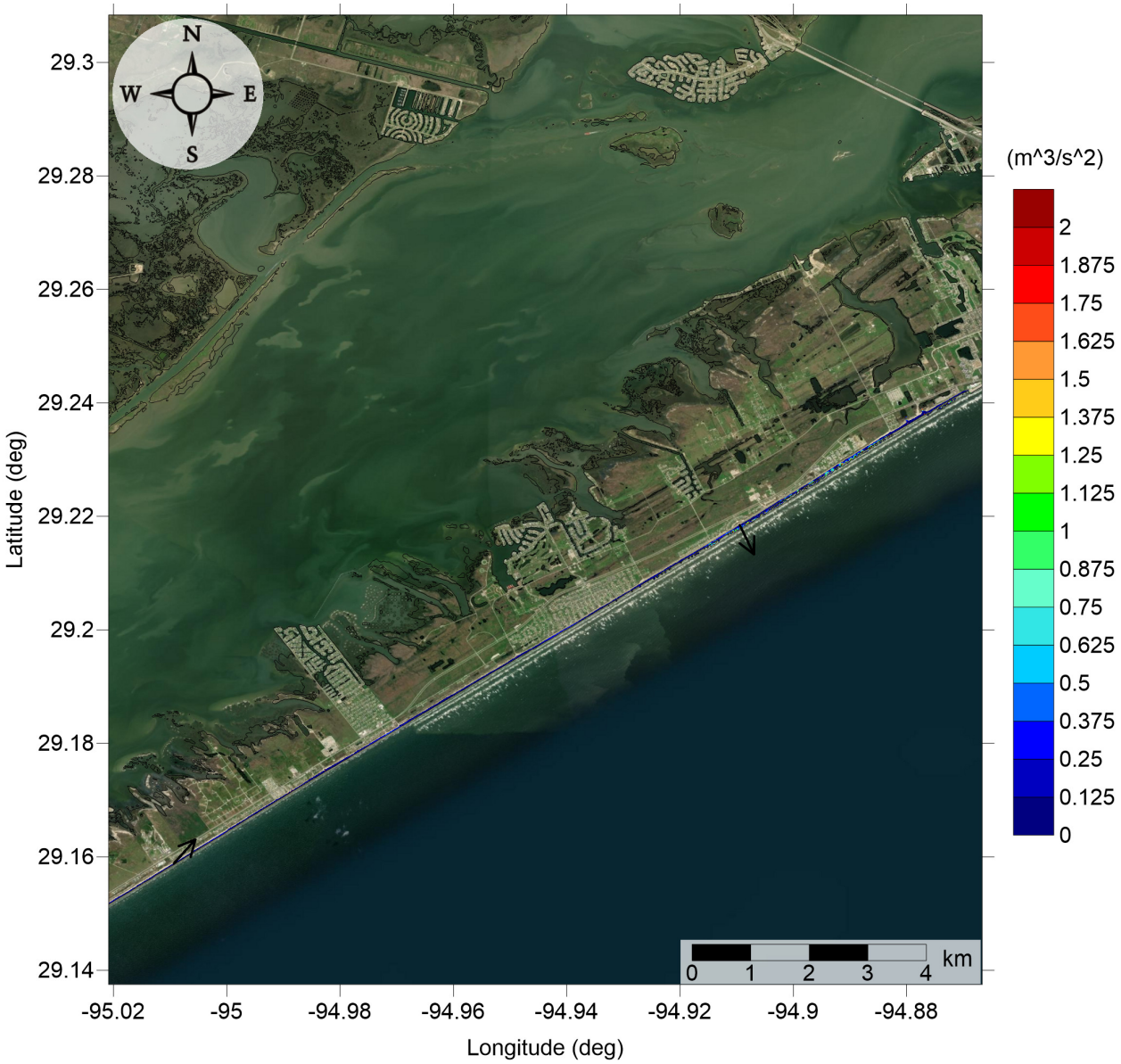

Figure 14: Maximum momentum flux (m^3/s^2) caused by the West Florida submarine landslide in Jamaica Beach, TX. Arrows represent direction of maximum momentum flux. Contour drawn is the zero-meter contour for land elevation.

Jamaica Beach, TX
West Florida submarine landslide
Maximum Inundation Depth

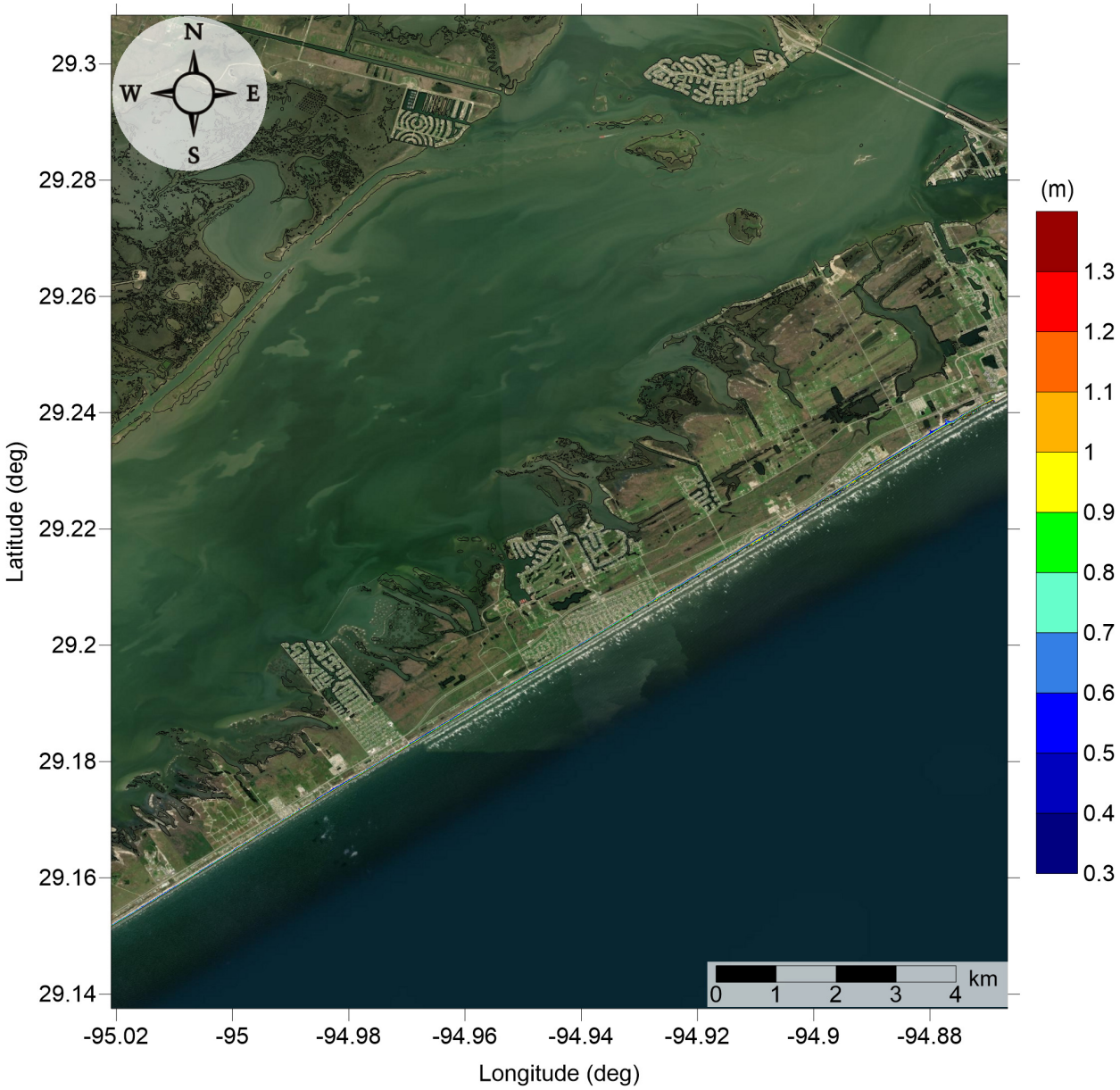

Figure 15: Maximum inundation depth (m) caused by the West Florida submarine landslide in Jamaica Beach, TX. Contour drawn is the zero-meter contour for land elevation.

Jamaica Beach, TX
Yucatán #3 submarine landslide
Maximum Momentum Flux

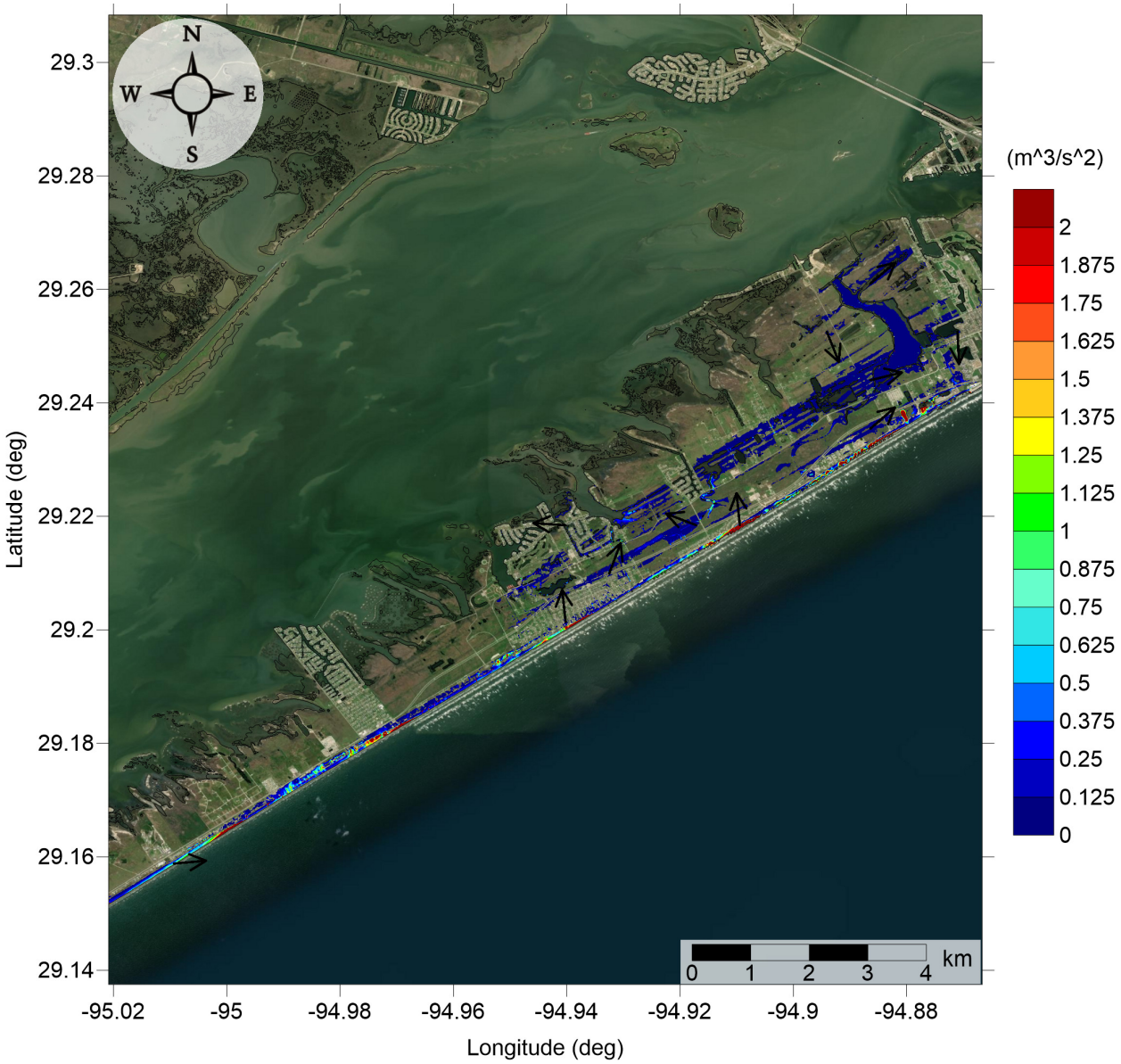

Figure 16: Maximum momentum flux (m^3/s^2) caused by the Yucatán #3 submarine landslide in Jamaica Beach, TX. Arrows represent direction of maximum momentum flux. Contour drawn is the zero-meter contour for land elevation.

Jamaica Beach, TX
Yucatán #3 submarine landslide
Maximum Inundation Depth

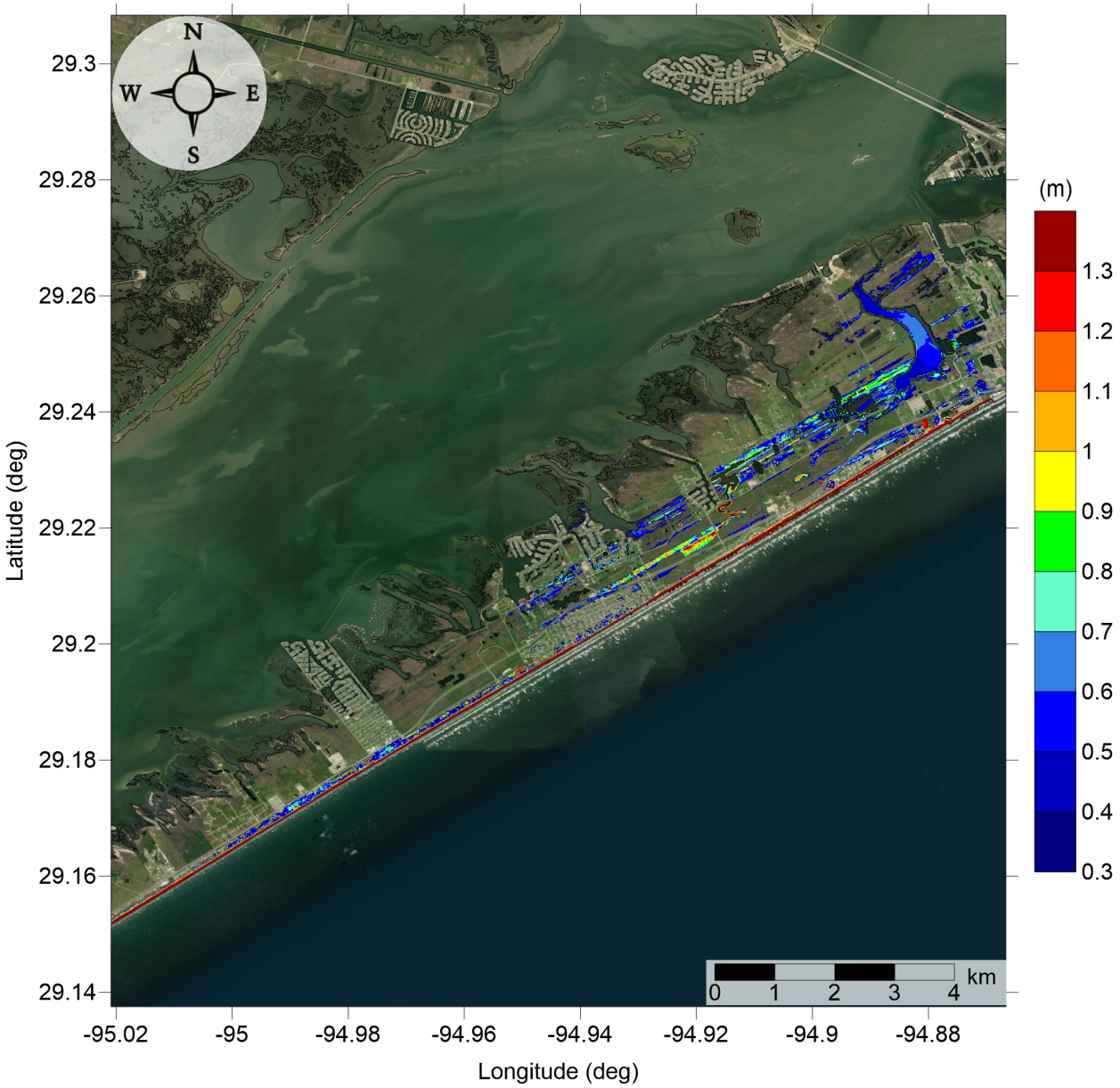

Figure 17: Maximum inundation depth (m) caused by the Yucatán #3 submarine landslide in Jamaica Beach, TX. Contour drawn is the zero-meter contour for land elevation.

Jamaica Beach, TX
Yucatán #5 submarine landslide
Maximum Momentum Flux

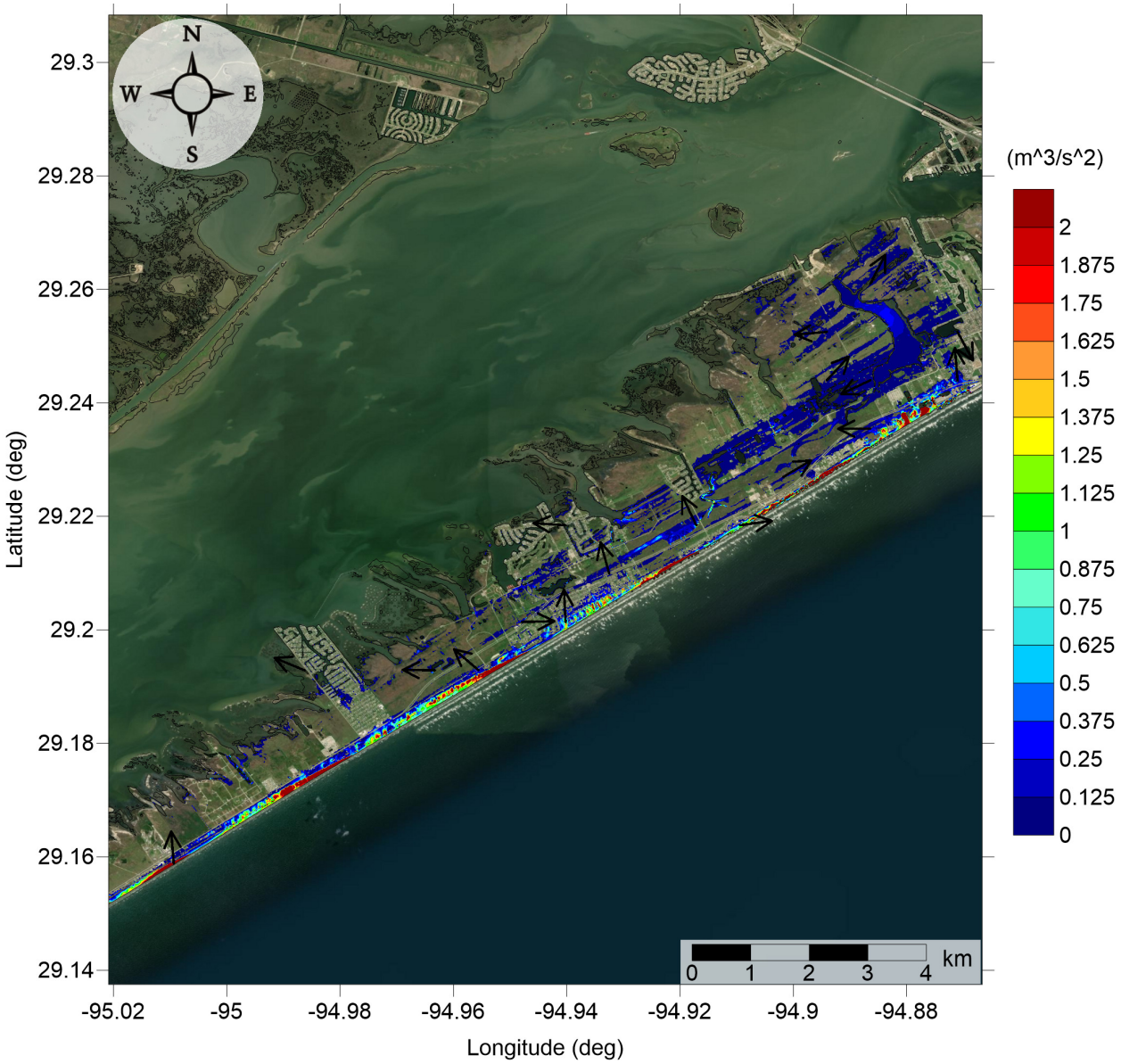

Figure 18: Maximum momentum flux (m^3/s^2) caused by the Yucatán #5 submarine landslide in Jamaica Beach, TX. Arrows represent direction of maximum momentum flux. Contour drawn is the zero-meter contour for land elevation.

Jamaica Beach, TX
Yucatán #5 submarine landslide
Maximum Inundation Depth

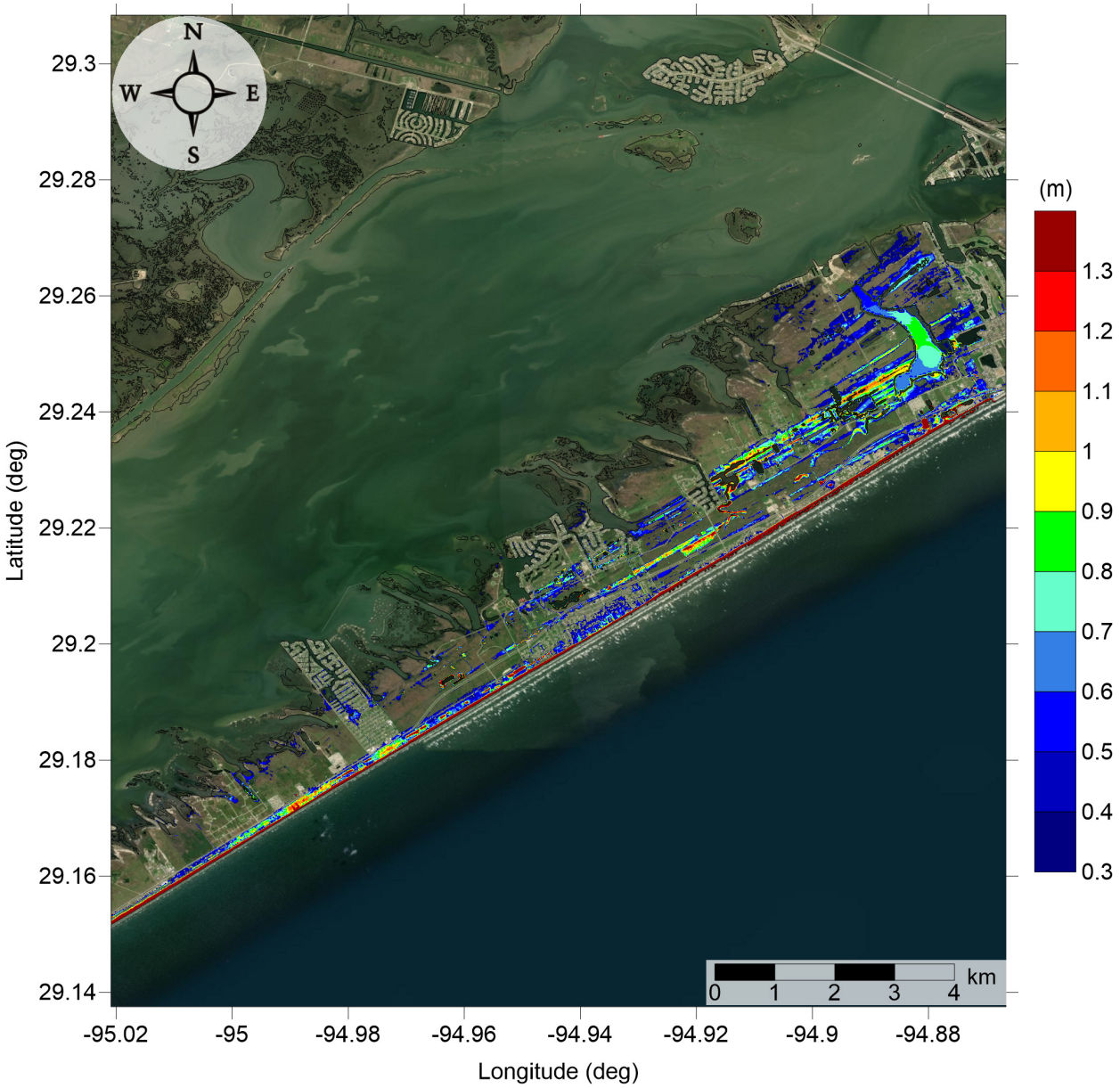

Figure 19: Maximum inundation depth (m) caused by the Yucatán #5 submarine landslide in Jamaica Beach, TX. Contour drawn is the zero-meter contour for land elevation.

Jamaica Beach, TX
All Sources
Maximum of Maximum Inundation Depth

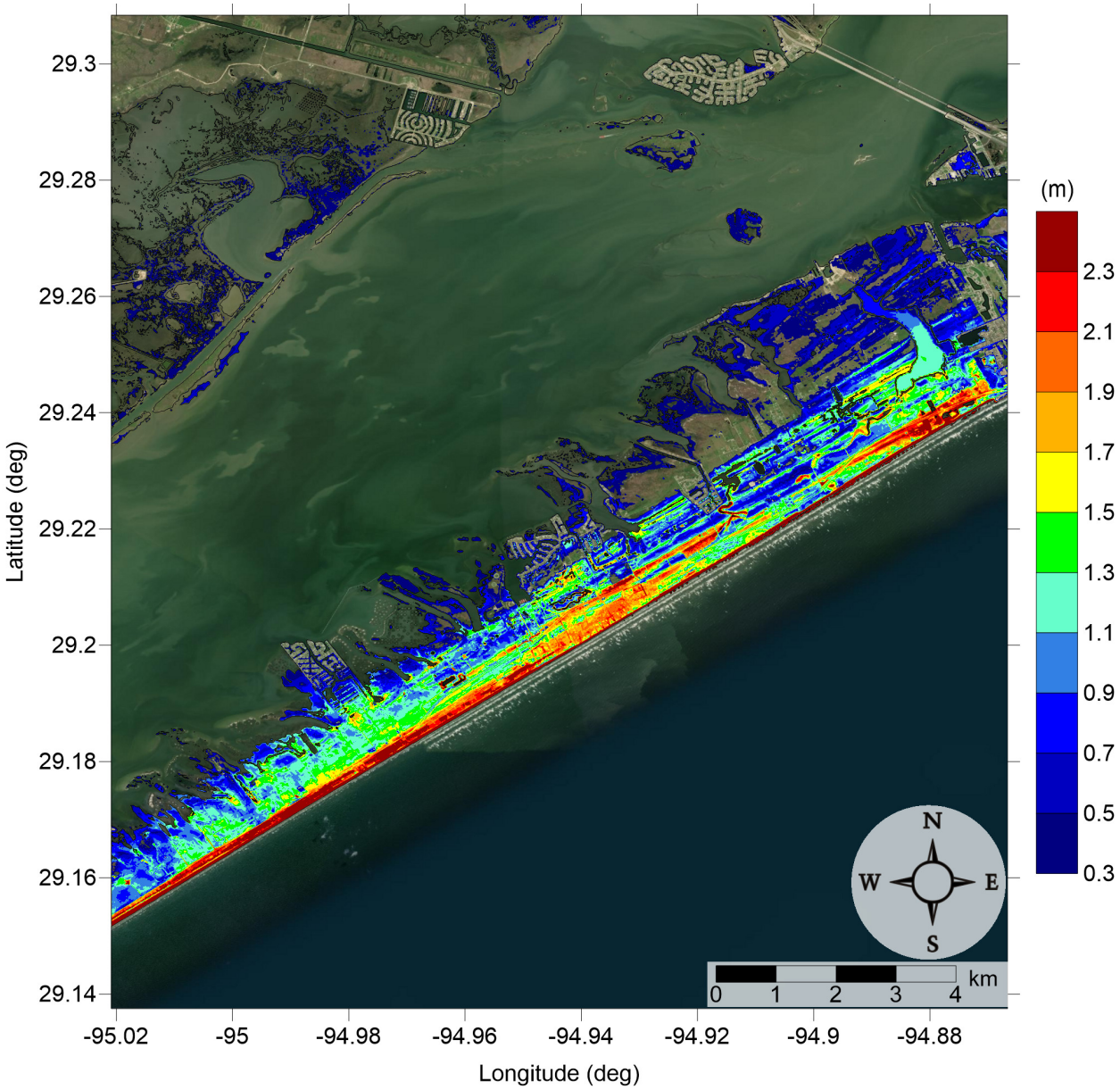

Figure 20: Maximum of maximums inundation depth (m) in Jamaica Beach, TX, calculated as the maximum inundation depth in each grid cell from an ensemble of all tsunami sources considered. Contour drawn is the zero-meter contour for land elevation.

Jamaica Beach, TX
All Sources
Maximum Inundation Depth by Source

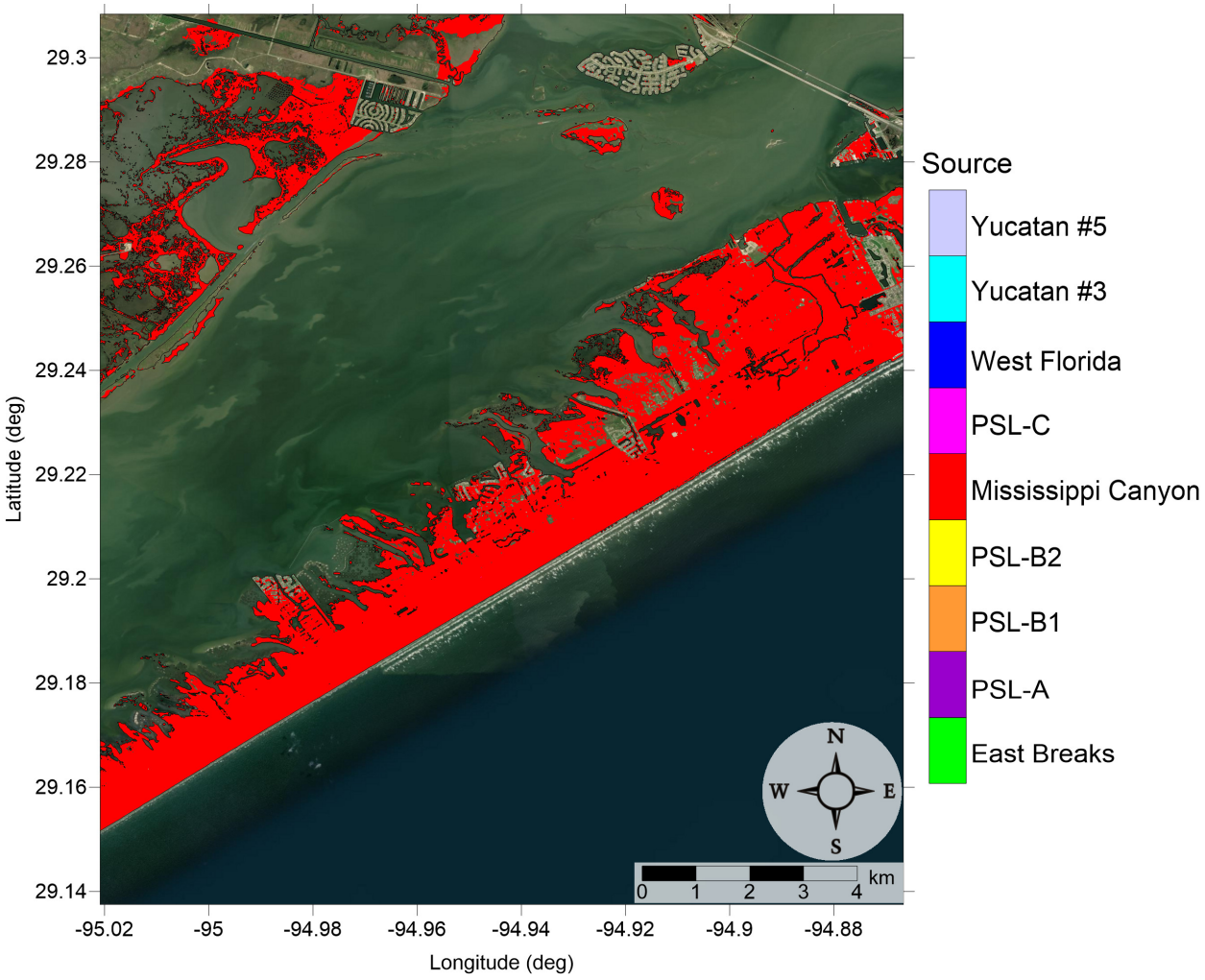

Figure 21: Indication of the tsunami source which causes the maximum of maximums inundation depth (m) in each grid cell from an ensemble of all tsunami sources in Jamaica Beach, TX. Contour drawn is the zero-meter contour for land elevation.

4.2 South Tampa Bay, FL

Table 3: Maximum tsunami wave amplitude and corresponding arrival time after landslide failure at South Tampa Bay, FL numerical wave gauge: 27°35'45"N, 83°3'45"W, approximate water depth 20 m.

Tsunami Source	Maximum Wave Amplitude (m)	Arrival Time After Landslide Failure (hr)
East Breaks	0.46	3.8
PSL-A	0.73	3.4
PSL-B1	1.06	2.7
PSL-B2	2.09	2.9
Mississippi Canyon	4.91	2.3
PSL-C	1.92	2.3
West Florida	1.34	2.1
Yucatán #3	0.57	2.8
Yucatán #5	0.30	2.9

South Tampa Bay, FL
East Breaks submarine landslide
Maximum Momentum Flux

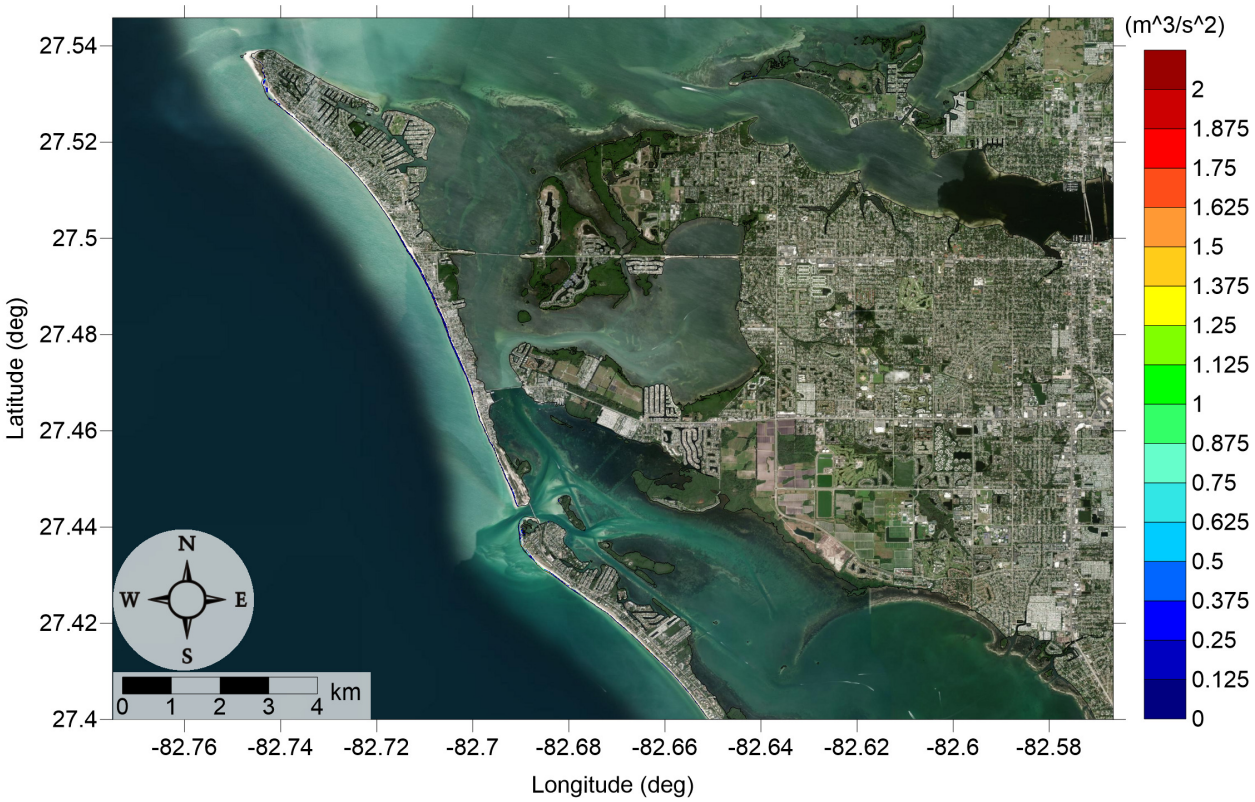

Figure 22: Maximum momentum flux (m^3/s^2) caused by the East Breaks submarine landslide in Anna Maria Island, FL. Arrows represent direction of maximum momentum flux. Contour drawn is the zero-meter contour for land elevation.

South Tampa Bay, FL
East Breaks submarine landslide
Maximum Momentum Flux

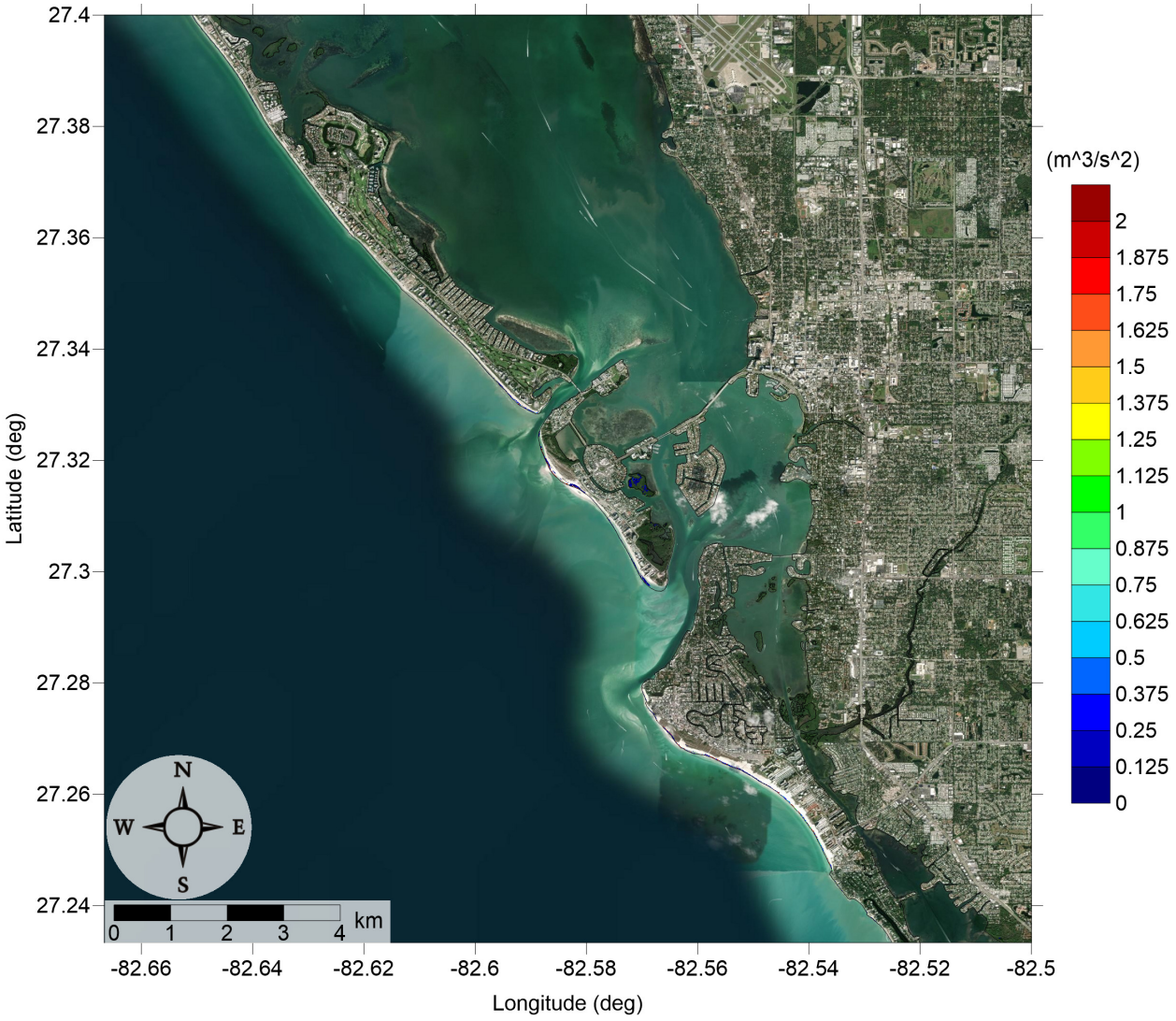

Figure 23: Maximum momentum flux (m^3/s^2) caused by the East Breaks submarine landslide in Siesta Key, FL. Arrows represent direction of maximum momentum flux. Contour drawn is the zero-meter contour for land elevation.

South Tampa Bay, FL
East Breaks submarine landslide
Maximum Inundation Depth

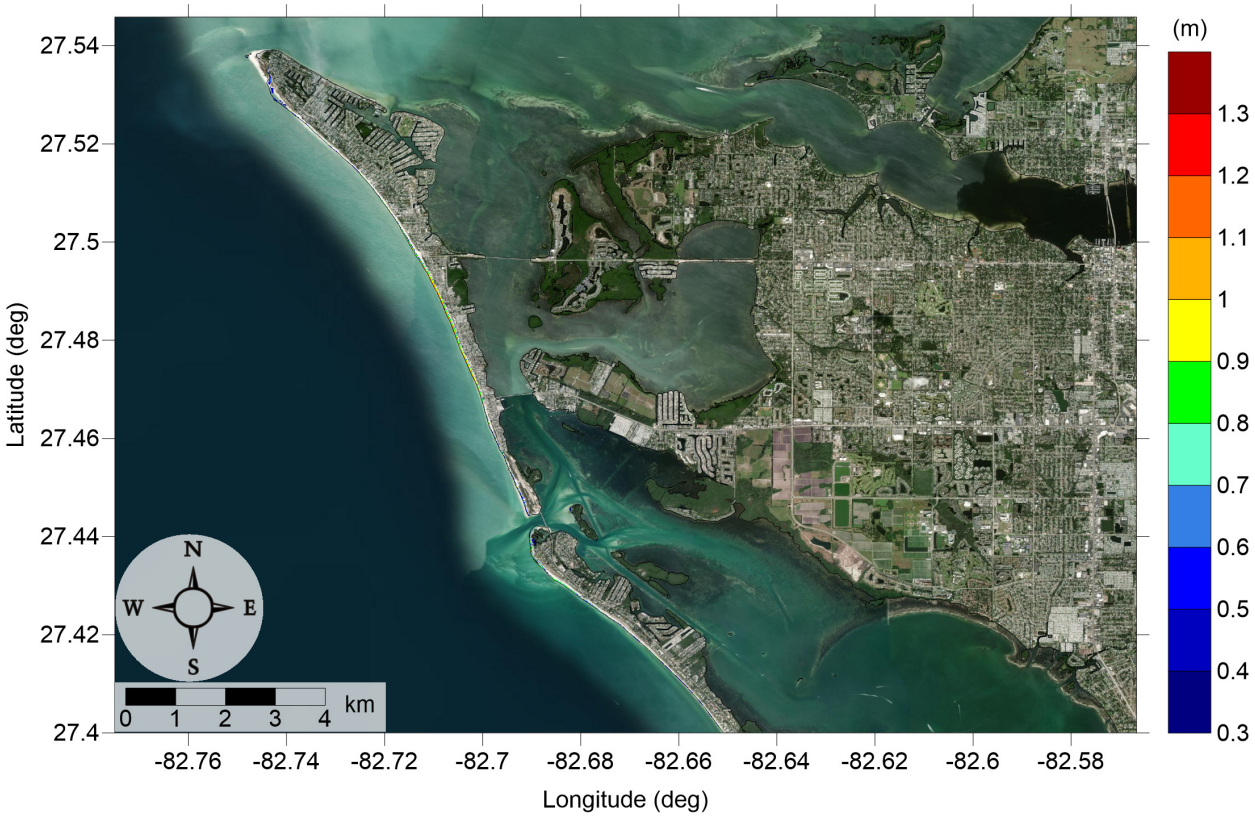

Figure 24: Maximum inundation depth (m) caused by the East Breaks submarine landslide in Anna Maria Island, FL. Contour drawn is the zero-meter contour for land elevation.

South Tampa Bay, FL
East Breaks submarine landslide
Maximum Inundation Depth

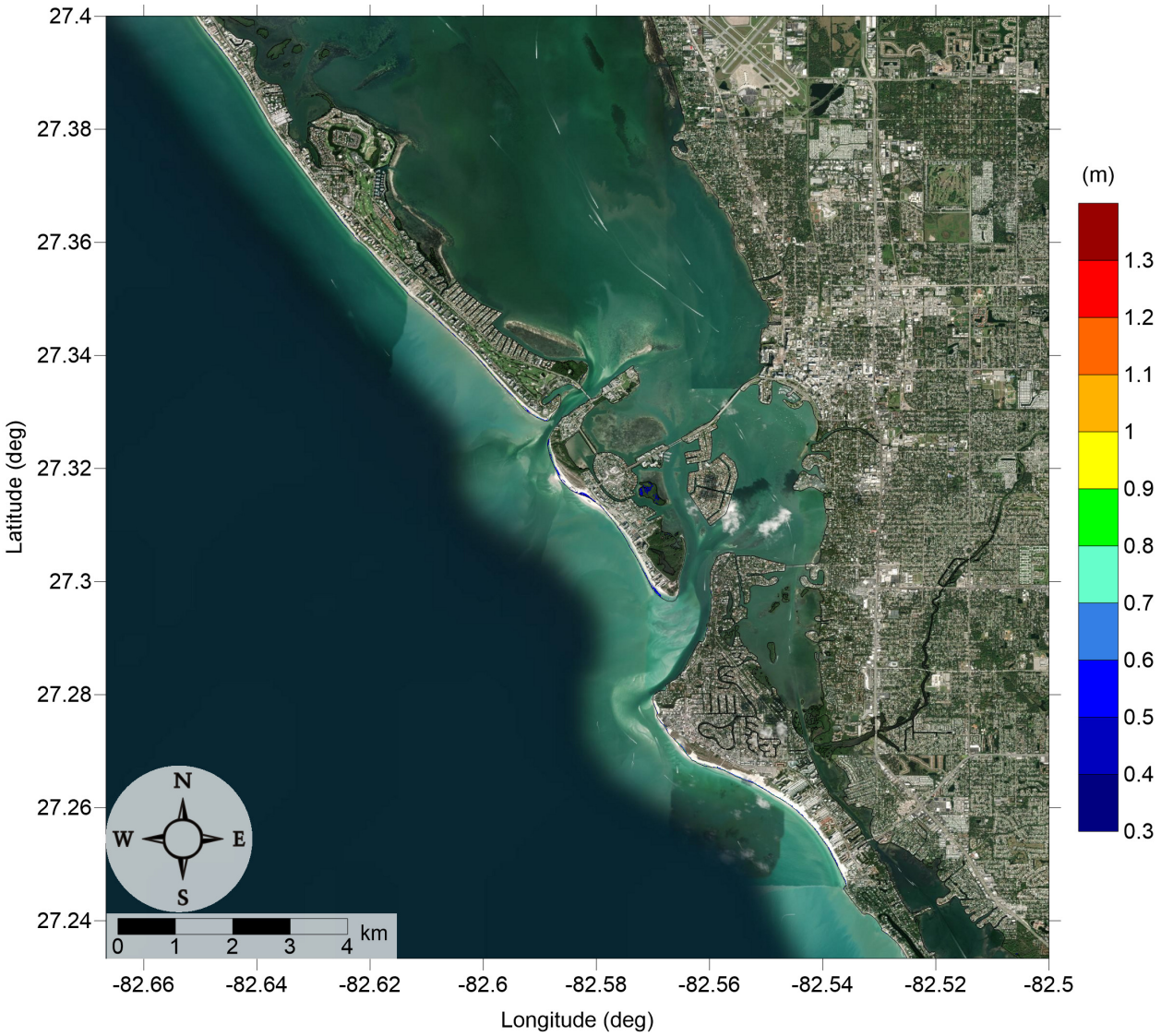

Figure 25: Maximum inundation depth (m) caused by the East Breaks submarine landslide in Siesta Key, FL. Contour drawn is the zero-meter contour for land elevation.

South Tampa Bay, FL
Probabilistic Submarine Landslide A
Maximum Momentum Flux

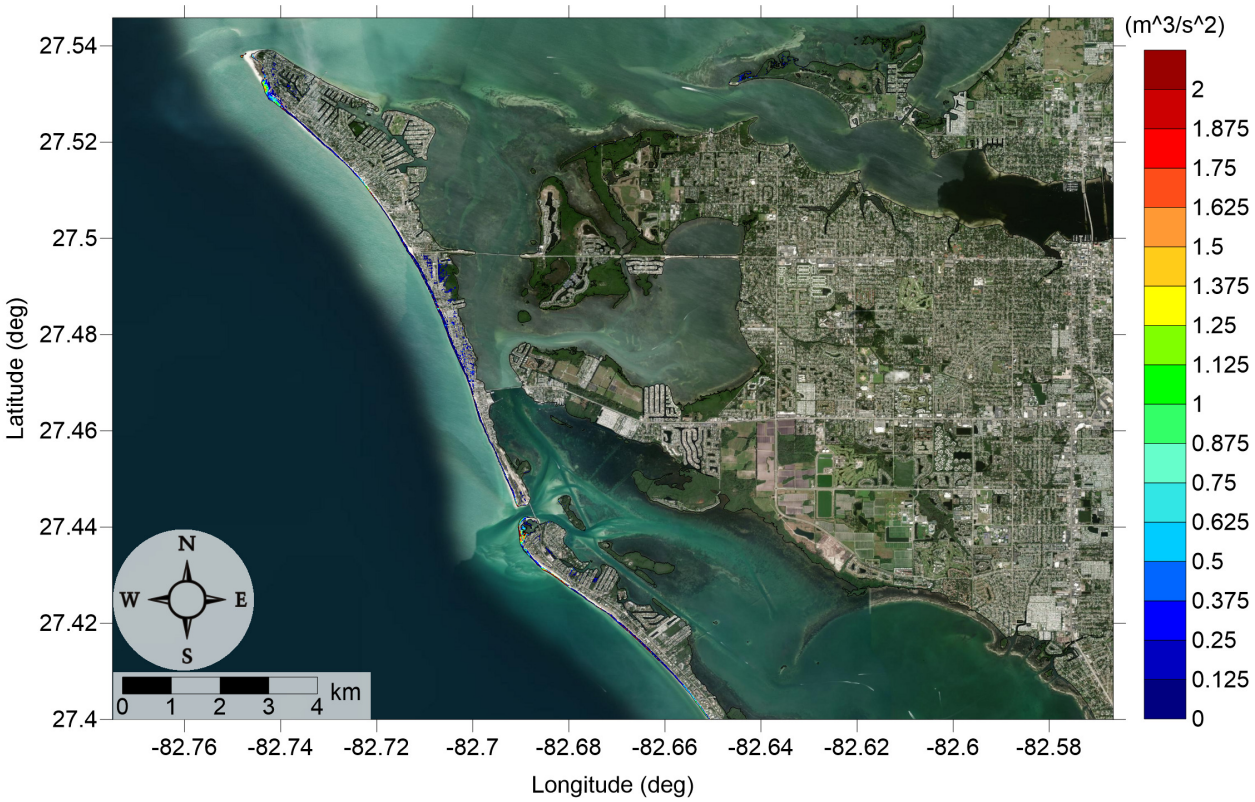

Figure 26: Maximum momentum flux (m^3/s^2) caused by the Probabilistic Submarine Landslide A in Anna Maria Island, FL. Arrows represent direction of maximum momentum flux. Contour drawn is the zero-meter contour for land elevation.

South Tampa Bay, FL
Probabilistic Submarine Landslide A
Maximum Momentum Flux

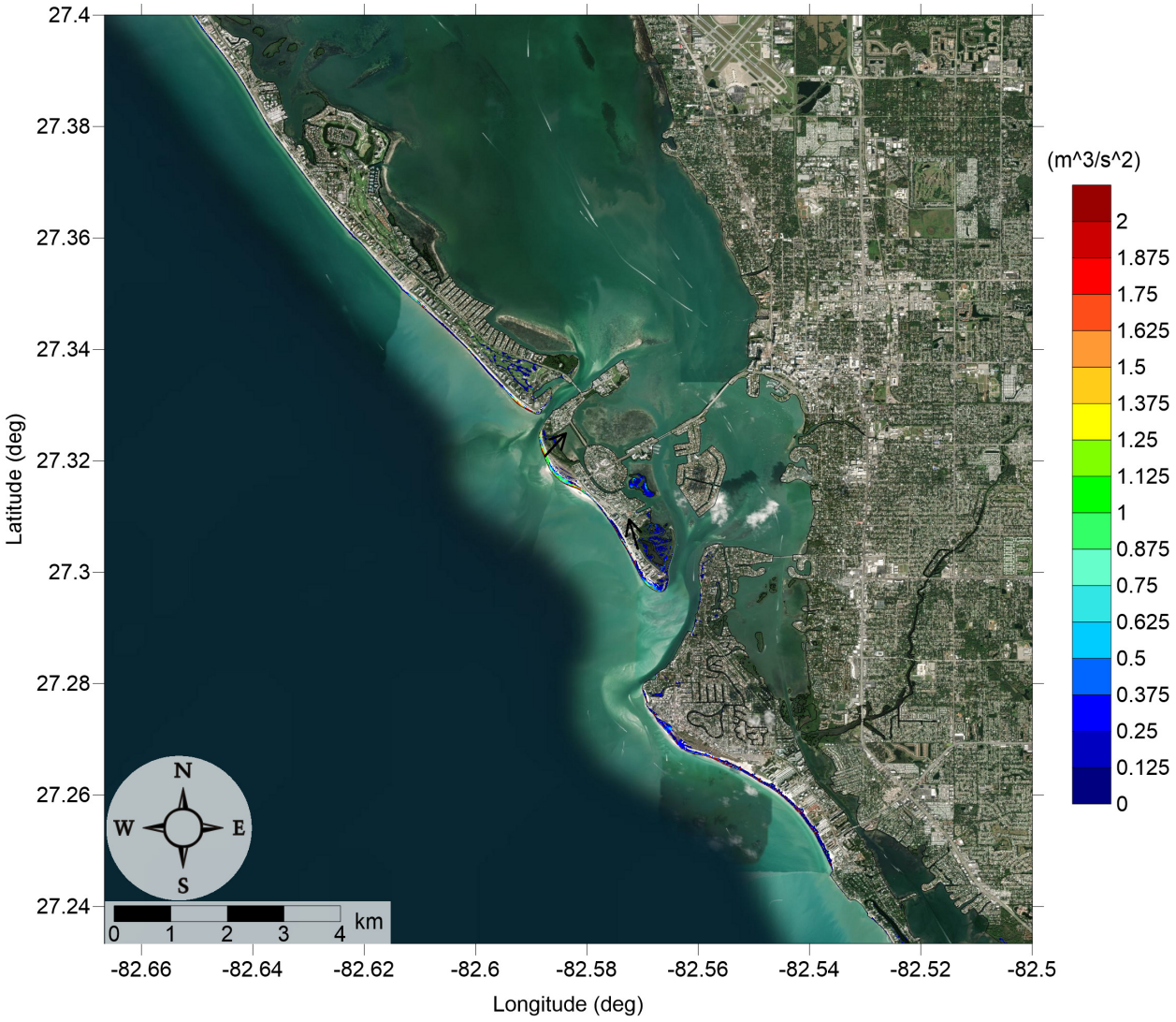

Figure 27: Maximum momentum flux (m^3/s^2) caused by the Probabilistic Submarine Landslide A in Siesta Key, FL. Arrows represent direction of maximum momentum flux. Contour drawn is the zero-meter contour for land elevation.

South Tampa Bay, FL
Probabilistic Submarine Landslide A
Maximum Inundation Depth

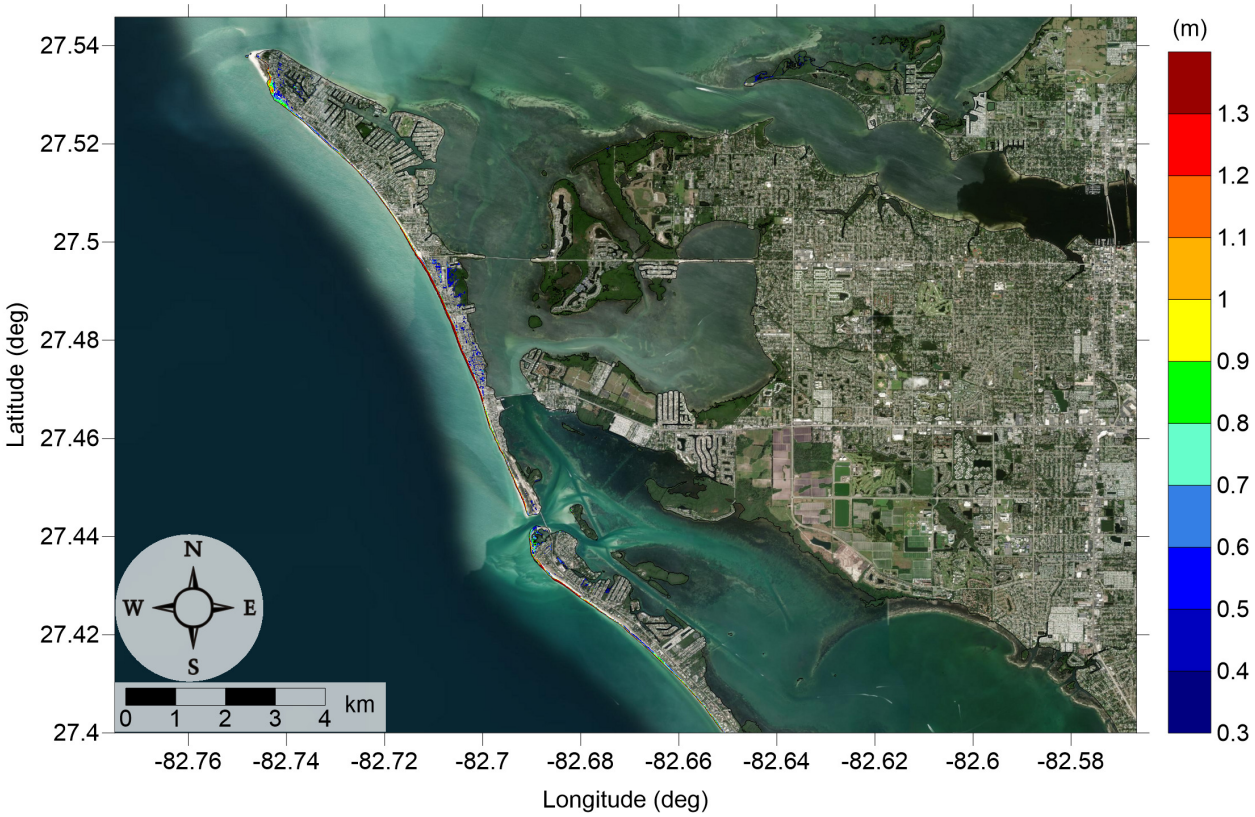

Figure 28: Maximum inundation depth (m) caused by the Probabilistic Submarine Landslide A in Anna Maria Island, FL. Contour drawn is the zero-meter contour for land elevation.

South Tampa Bay, FL
Probabilistic Submarine Landslide A
Maximum Inundation Depth

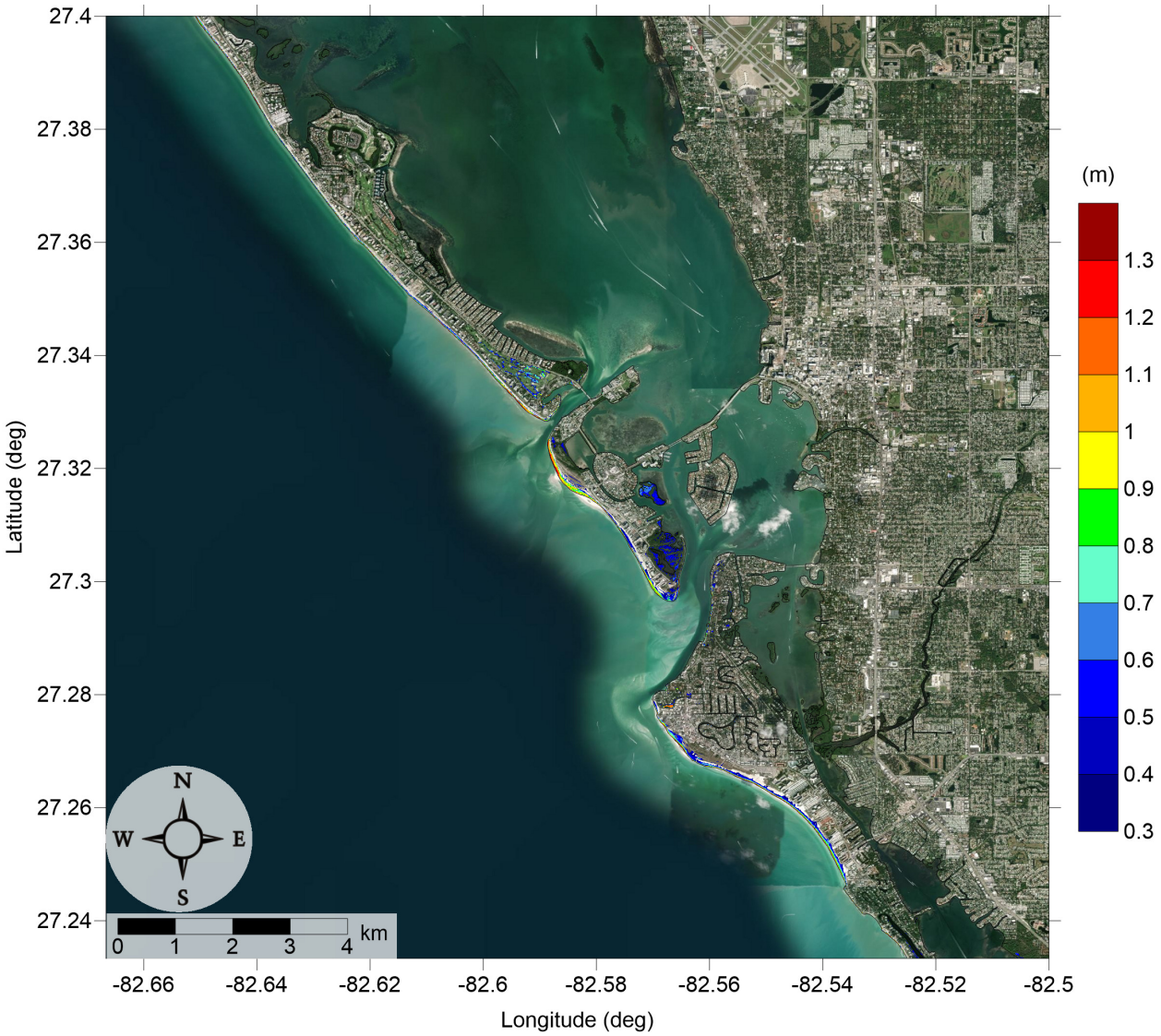

Figure 29: Maximum inundation depth (m) caused by the Probabilistic Submarine Landslide A in Siesta Key, FL. Contour drawn is the zero-meter contour for land elevation.

South Tampa Bay, FL
Probabilistic Submarine Landslide B1
Maximum Momentum Flux

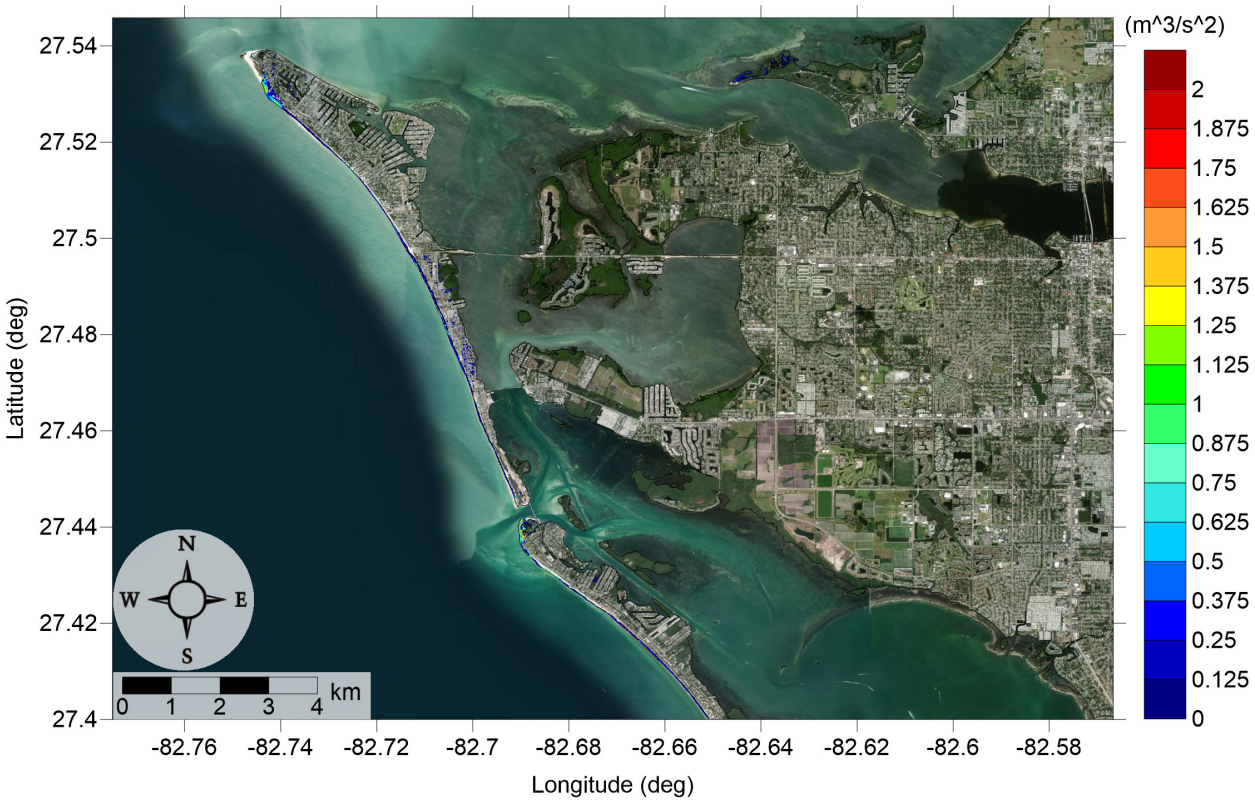

Figure 30: Maximum momentum flux (m^3/s^2) caused by the Probabilistic Submarine Landslide B1 in Anna Maria Island, FL. Arrows represent direction of maximum momentum flux. Contour drawn is the zero-meter contour for land elevation.

South Tampa Bay, FL
Probabilistic Submarine Landslide B1
Maximum Momentum Flux

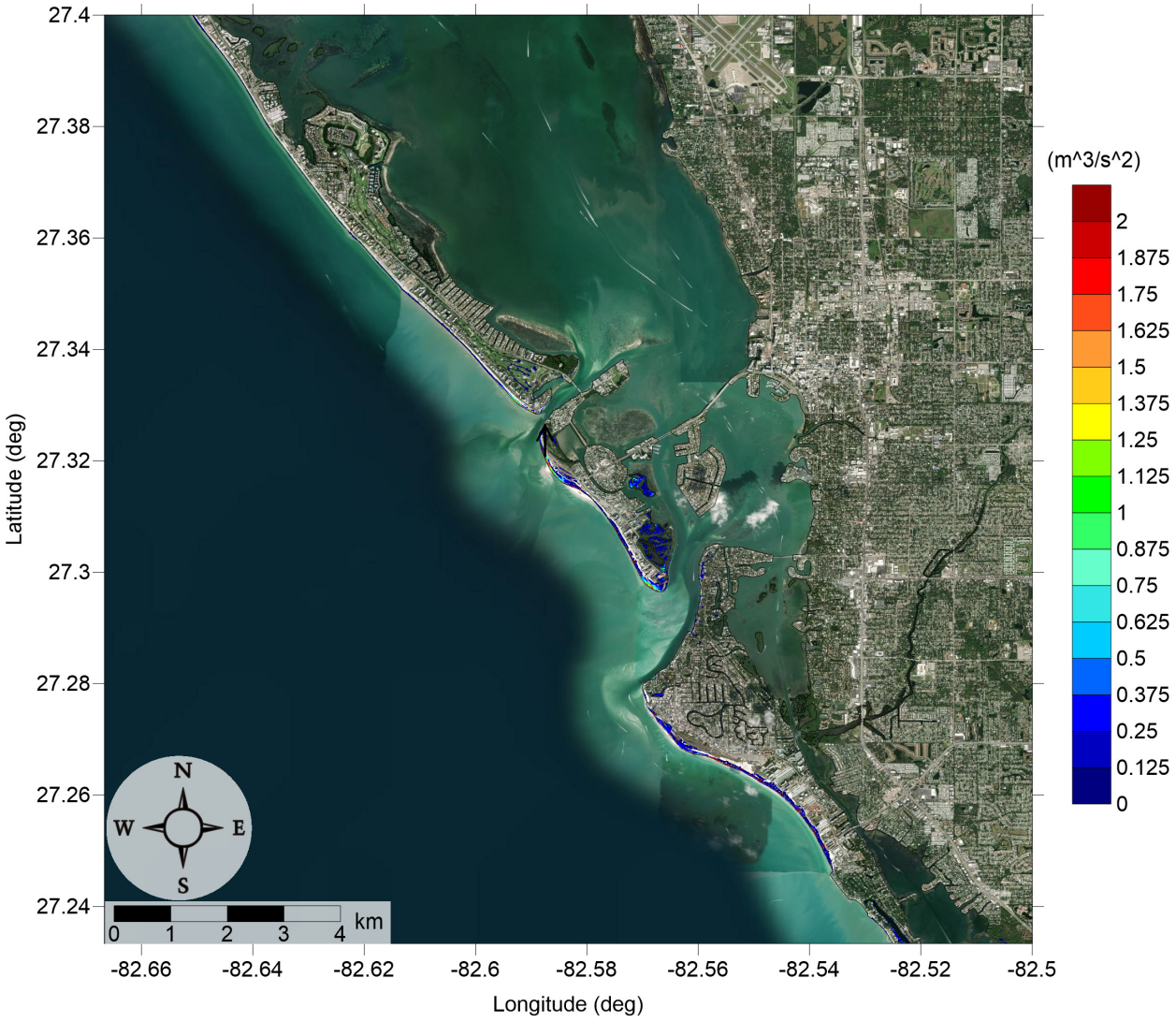

Figure 31: Maximum momentum flux (m^3/s^2) caused by the Probabilistic Submarine Landslide B1 in Siesta Key, FL. Arrows represent direction of maximum momentum flux. Contour drawn is the zero-meter contour for land elevation.

South Tampa Bay, FL
Probabilistic Submarine Landslide B1
Maximum Inundation Depth

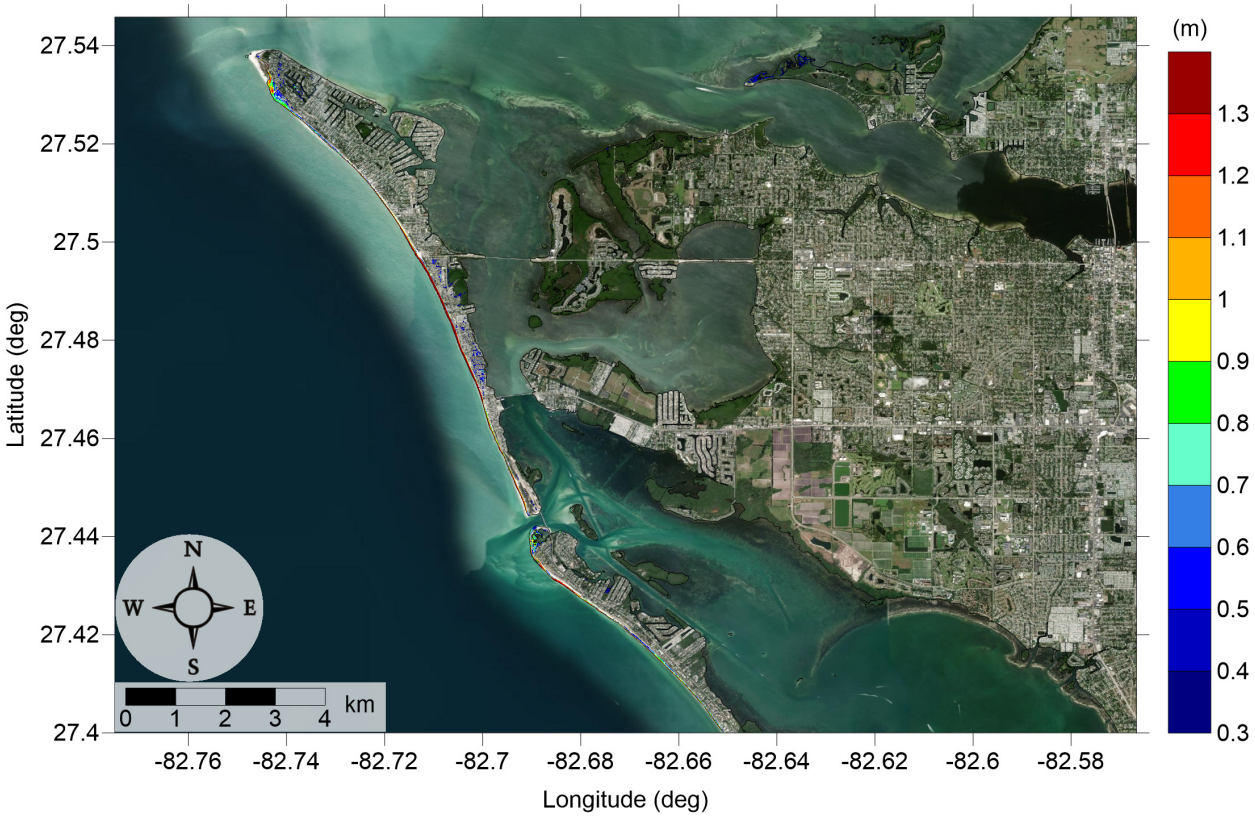

Figure 32: Maximum inundation depth (m) caused by the Probabilistic Submarine Landslide B1 in Anna Maria Island, FL. Contour drawn is the zero-meter contour for land elevation.

South Tampa Bay, FL
Probabilistic Submarine Landslide B1
Maximum Inundation Depth

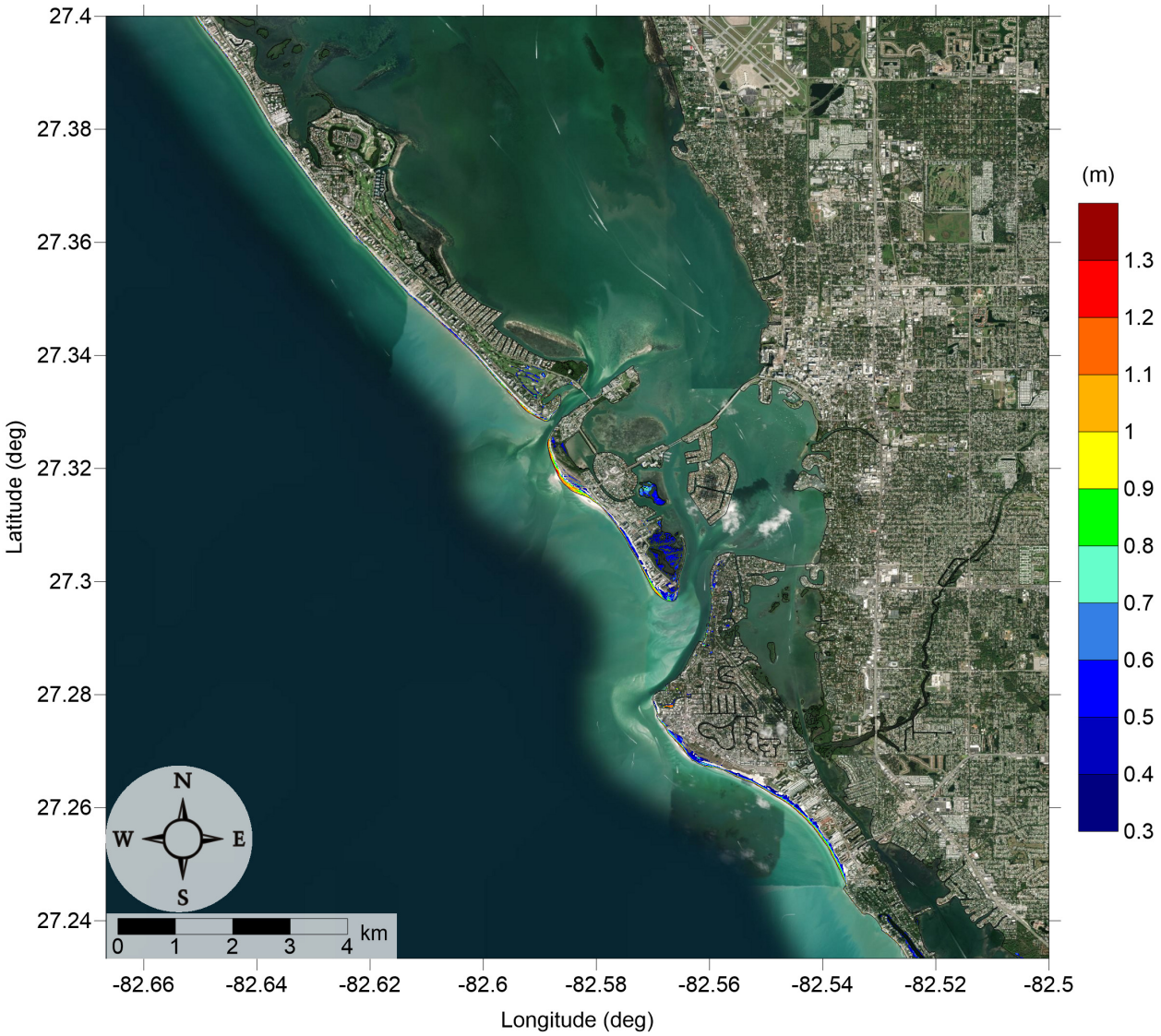

Figure 33: Maximum inundation depth (m) caused by the Probabilistic Submarine Landslide B1 in Siesta Key, FL. Contour drawn is the zero-meter contour for land elevation.

South Tampa Bay, FL
Probabilistic Submarine Landslide B2
Maximum Momentum Flux

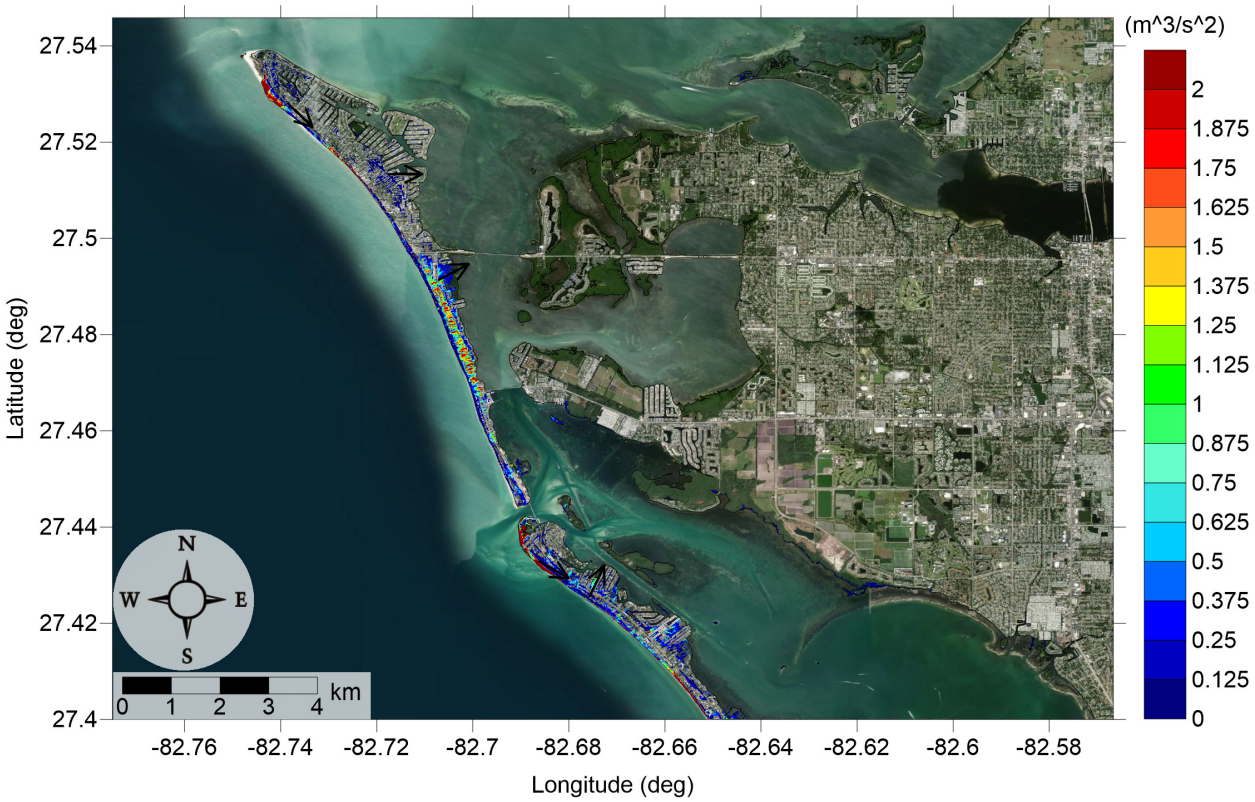

Figure 34: Maximum momentum flux (m^3/s^2) caused by the Probabilistic Submarine Landslide B2 in Anna Maria Island, FL. Arrows represent direction of maximum momentum flux. Contour drawn is the zero-meter contour for land elevation.

South Tampa Bay, FL
Probabilistic Submarine Landslide B2
Maximum Momentum Flux

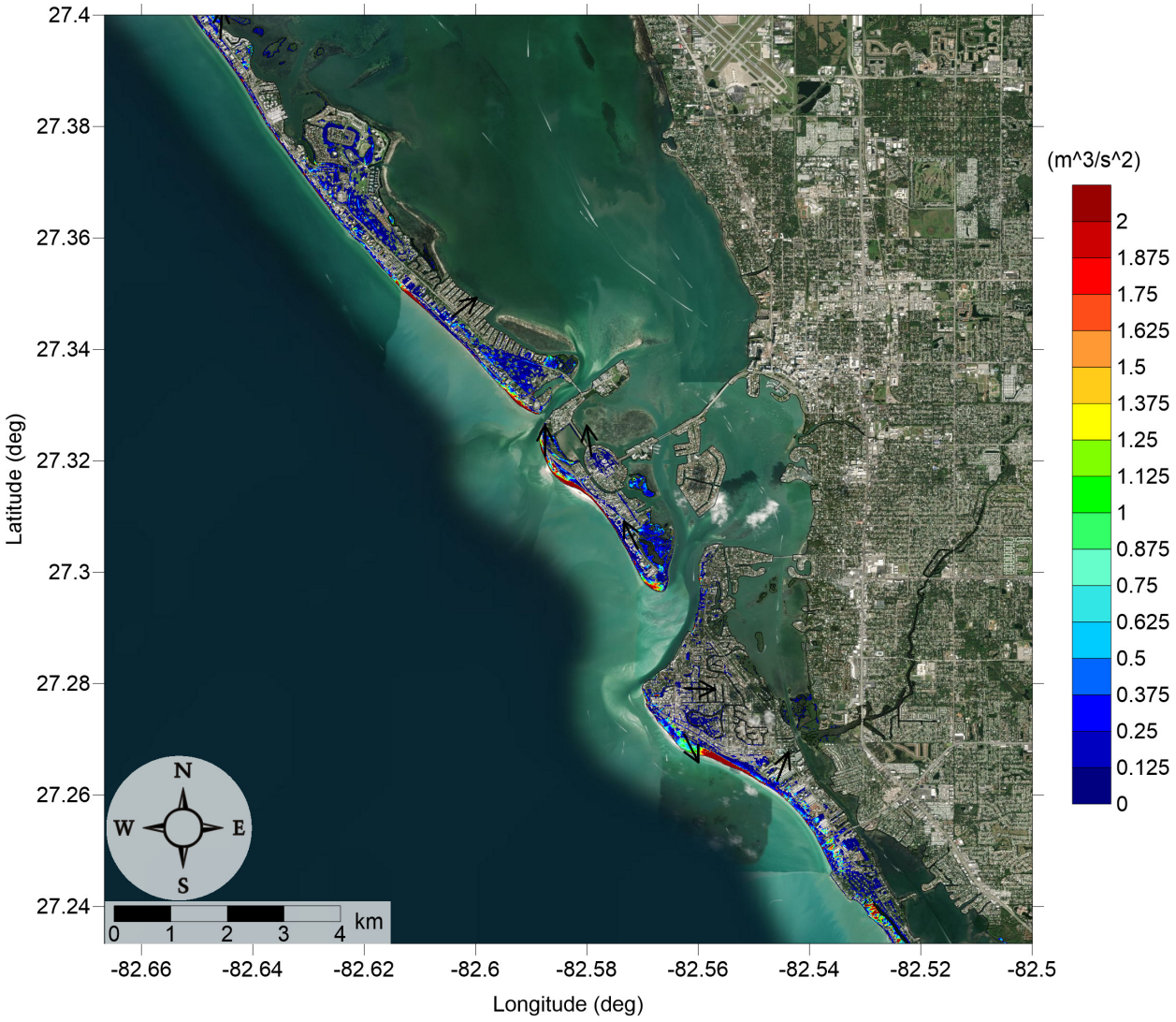

Figure 35: Maximum momentum flux (m^3/s^2) caused by the Probabilistic Submarine Landslide B2 in Siesta Key, FL. Arrows represent direction of maximum momentum flux. Contour drawn is the zero-meter contour for land elevation.

South Tampa Bay, FL
Probabilistic Submarine Landslide B2
Maximum Inundation Depth

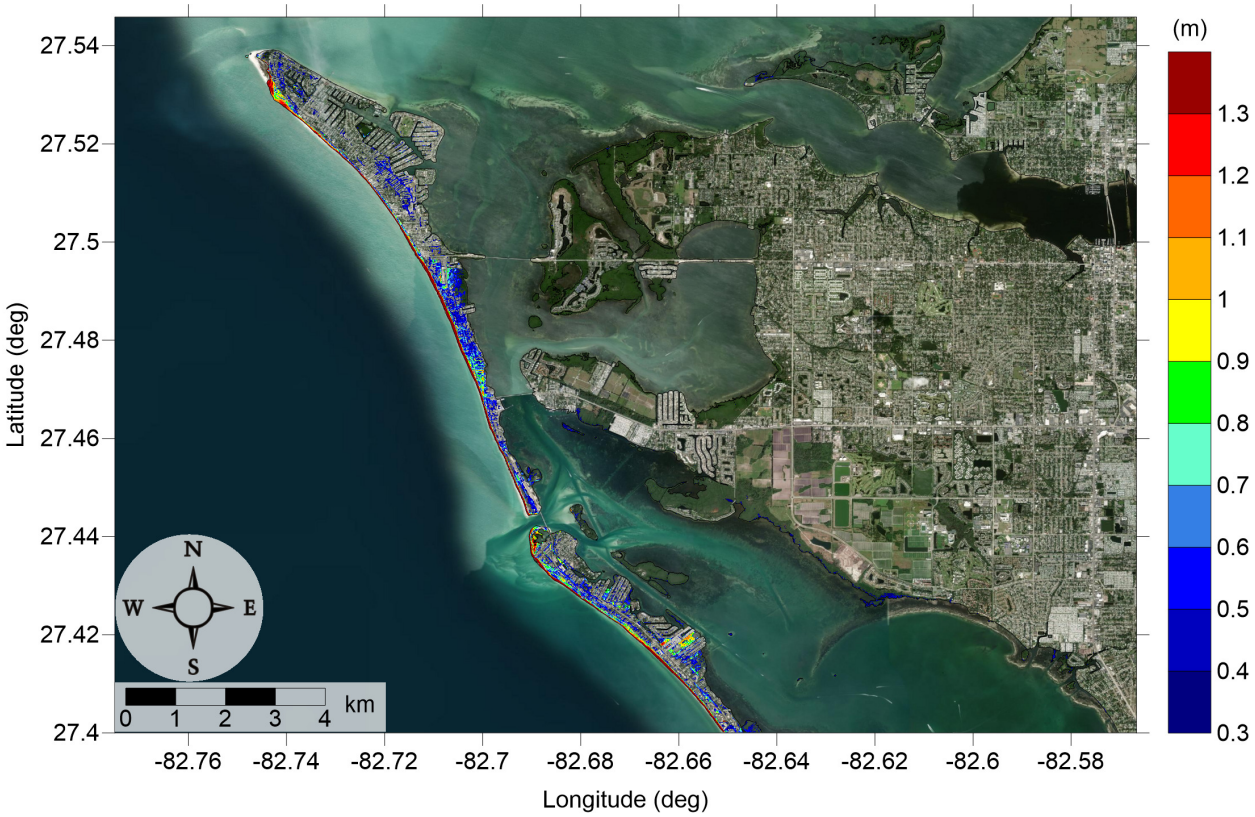

Figure 36: Maximum inundation depth (m) caused by the Probabilistic Submarine Landslide B2 in Anna Maria Island, FL. Contour drawn is the zero-meter contour for land elevation.

South Tampa Bay, FL
Probabilistic Submarine Landslide B2
Maximum Inundation Depth

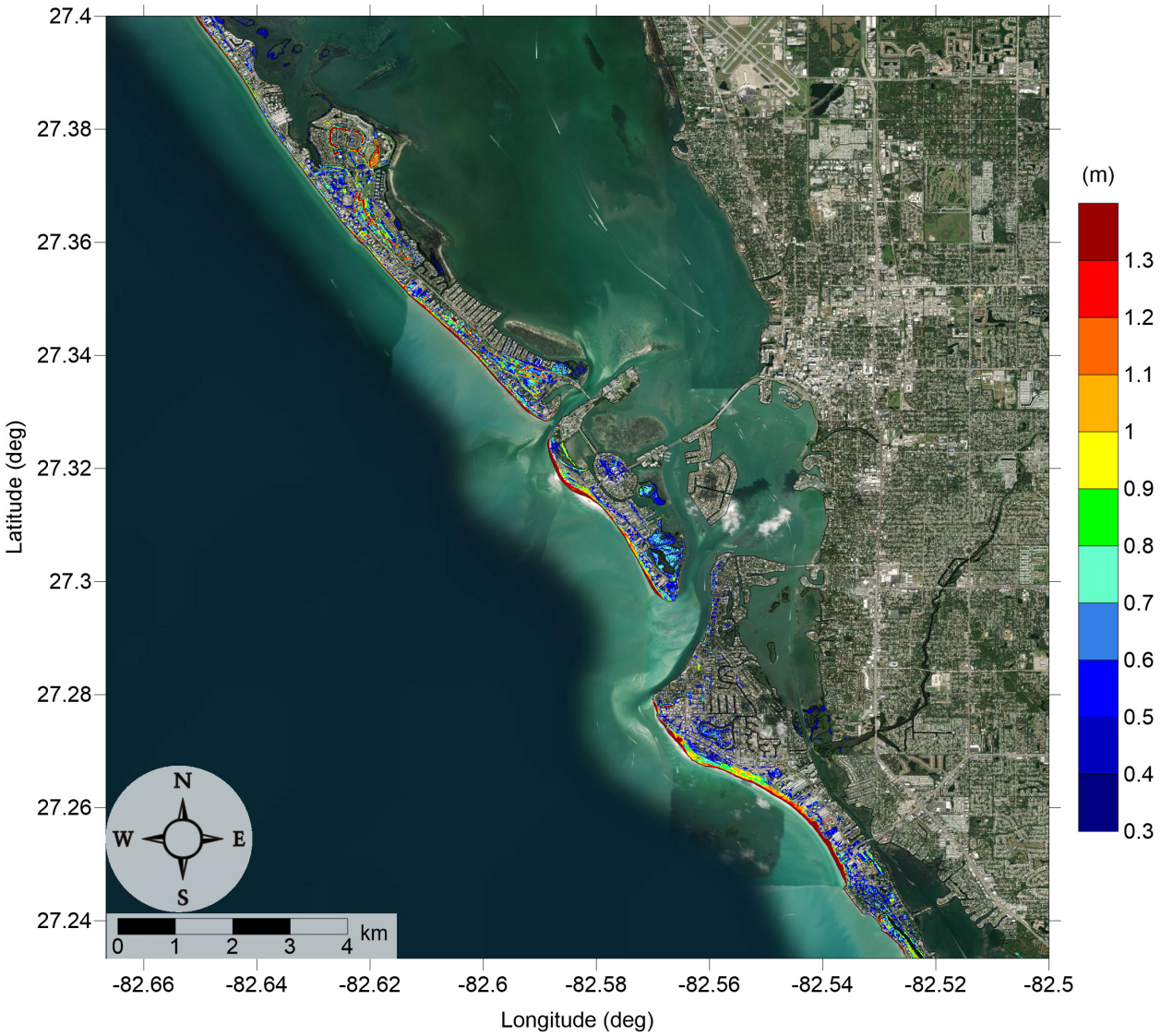

Figure 37: Maximum inundation depth (m) caused by the Probabilistic Submarine Landslide B2 in Siesta Key, FL. Contour drawn is the zero-meter contour for land elevation.

South Tampa Bay, FL
Mississippi Canyon submarine landslide
Maximum Momentum Flux

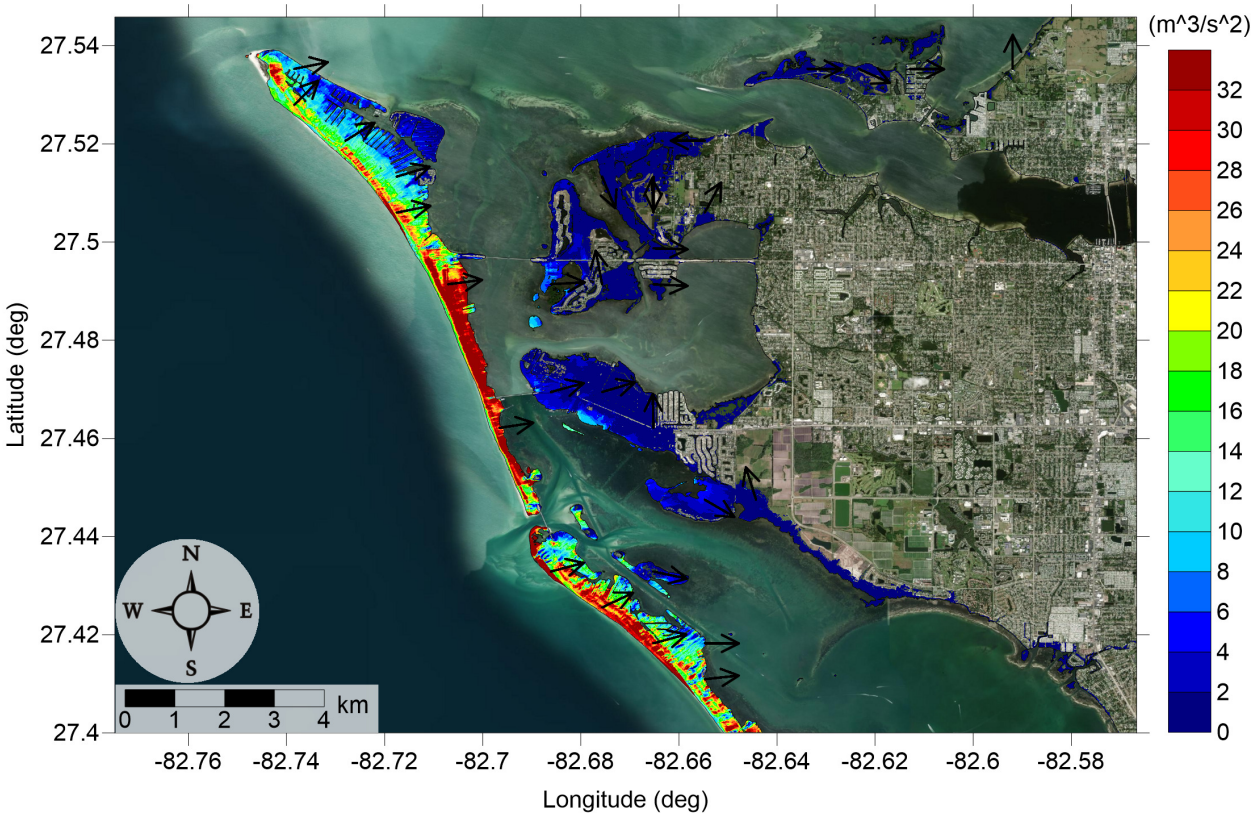

Figure 38: Maximum momentum flux (m^3/s^2) caused by the Mississippi Canyon submarine landslide in Anna Maria Island, FL. Arrows represent direction of maximum momentum flux. Contour drawn is the zero-meter contour for land elevation.

South Tampa Bay, FL
Mississippi Canyon submarine landslide
Maximum Momentum Flux

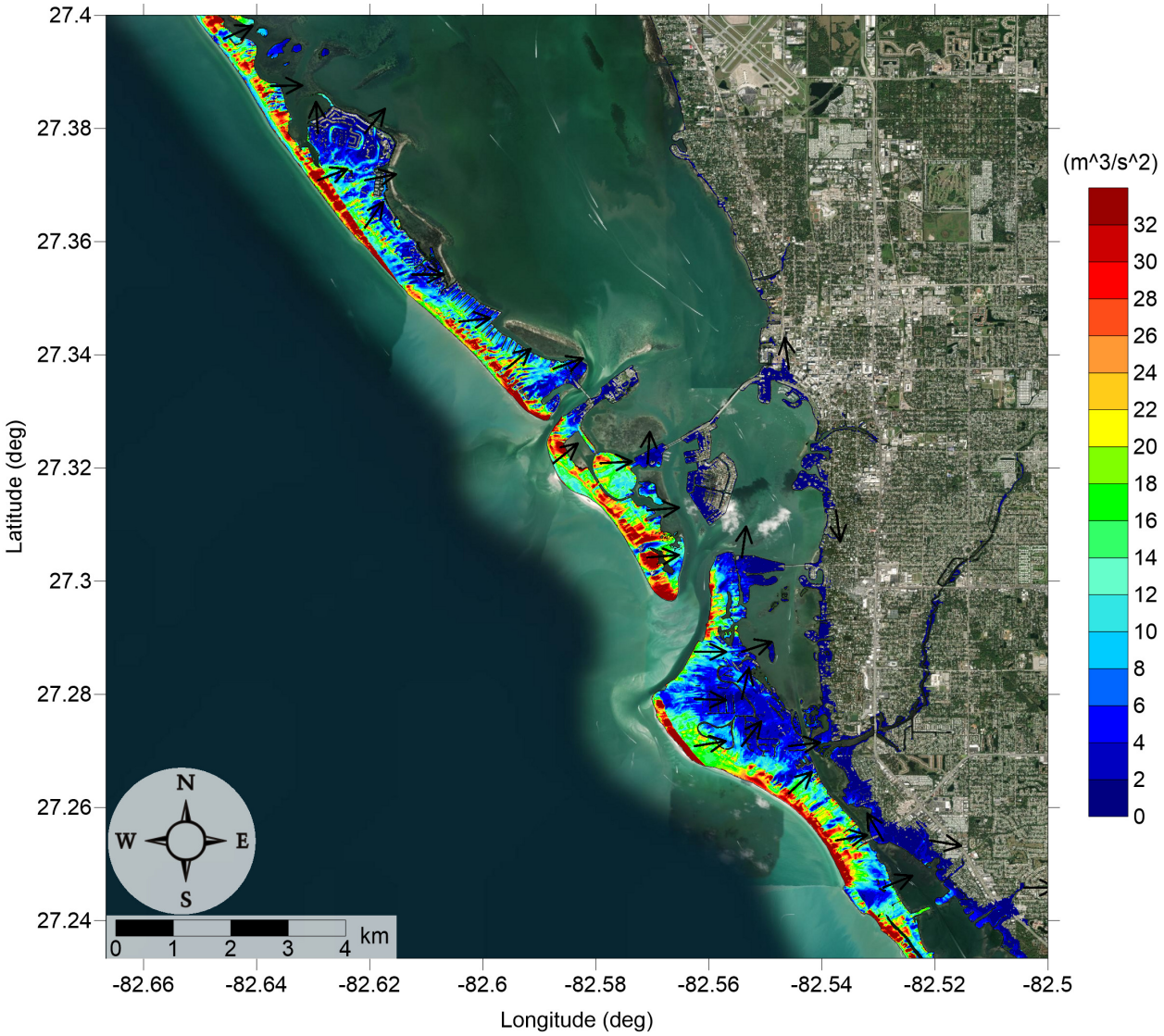

Figure 39: Maximum momentum flux (m^3/s^2) caused by the Mississippi Canyon submarine landslide in Siesta Key, FL. Arrows represent direction of maximum momentum flux. Contour drawn is the zero-meter contour for land elevation.

South Tampa Bay, FL
Mississippi Canyon submarine landslide
Maximum Inundation Depth

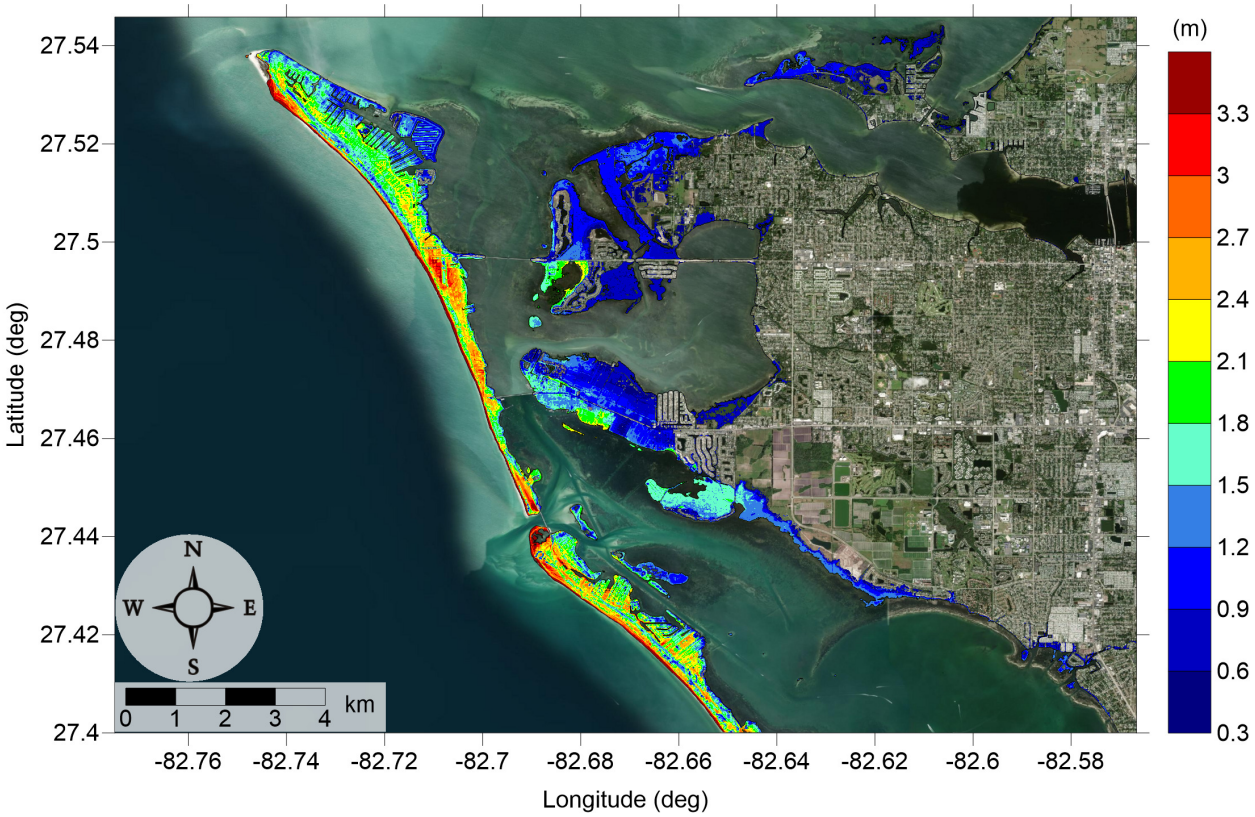

Figure 40: Maximum inundation depth (m) caused by the Mississippi Canyon submarine landslide in Anna Maria Island, FL. Contour drawn is the zero-meter contour for land elevation.

South Tampa Bay, FL
Mississippi Canyon submarine landslide
Maximum Inundation Depth

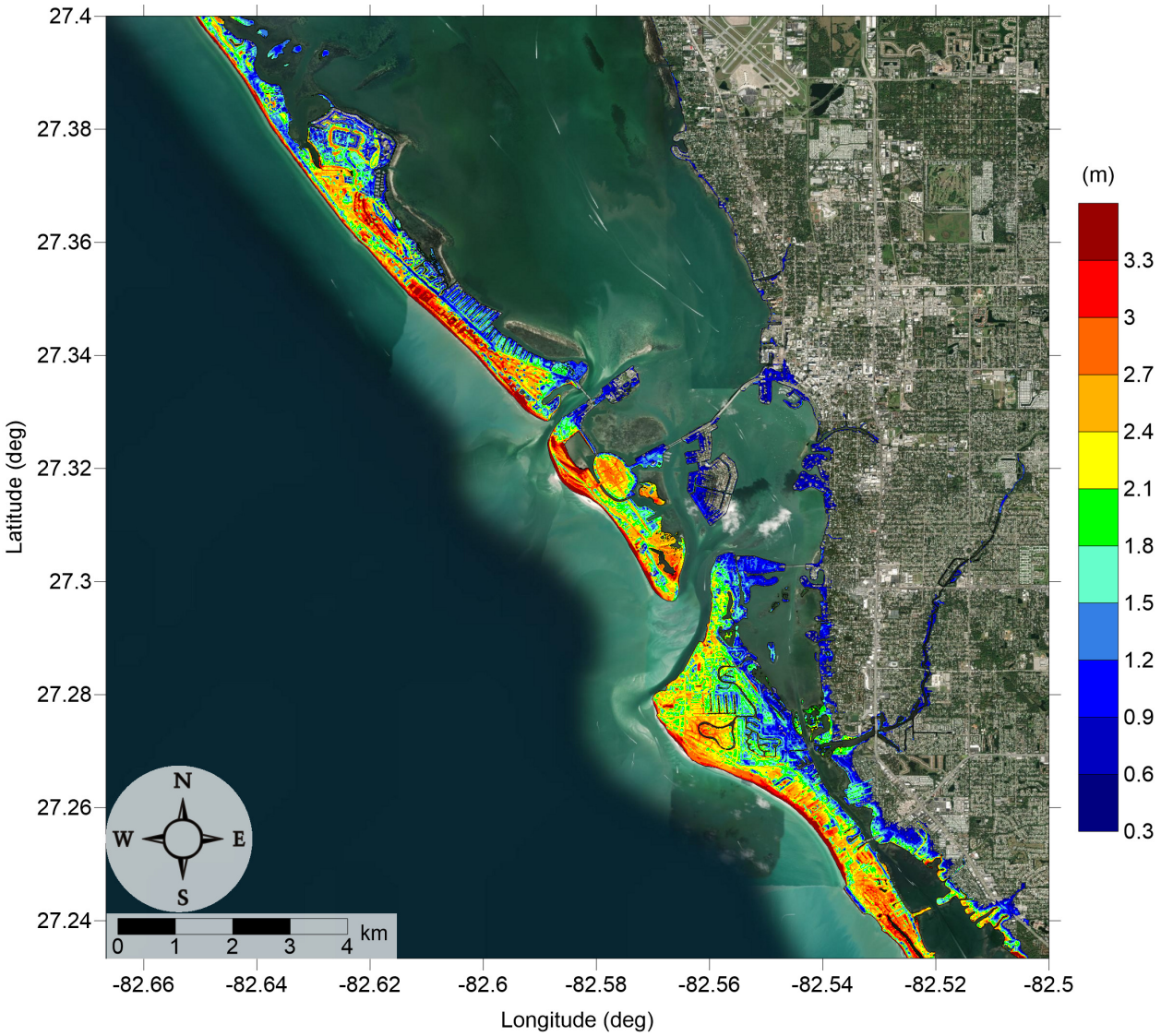

Figure 41: Maximum inundation depth (m) caused by the Mississippi Canyon submarine landslide in Siesta Key, FL. Contour drawn is the zero-meter contour for land elevation.

South Tampa Bay, FL
Probabilistic Submarine Landslide C
Maximum Momentum Flux

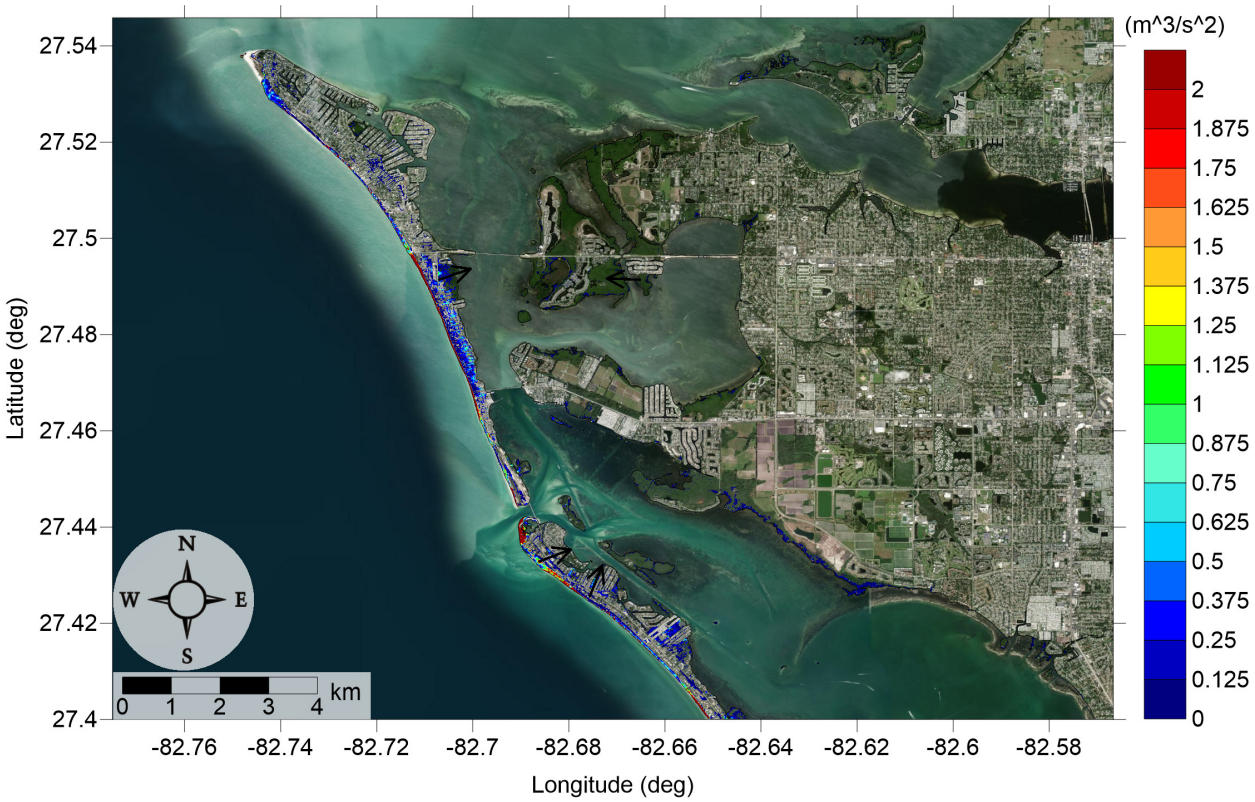

Figure 42: Maximum momentum flux (m^3/s^2) caused by the Probabilistic Submarine Landslide C in Anna Maria Island, FL. Arrows represent direction of maximum momentum flux. Contour drawn is the zero-meter contour for land elevation.

South Tampa Bay, FL
Probabilistic Submarine Landslide C
Maximum Momentum Flux

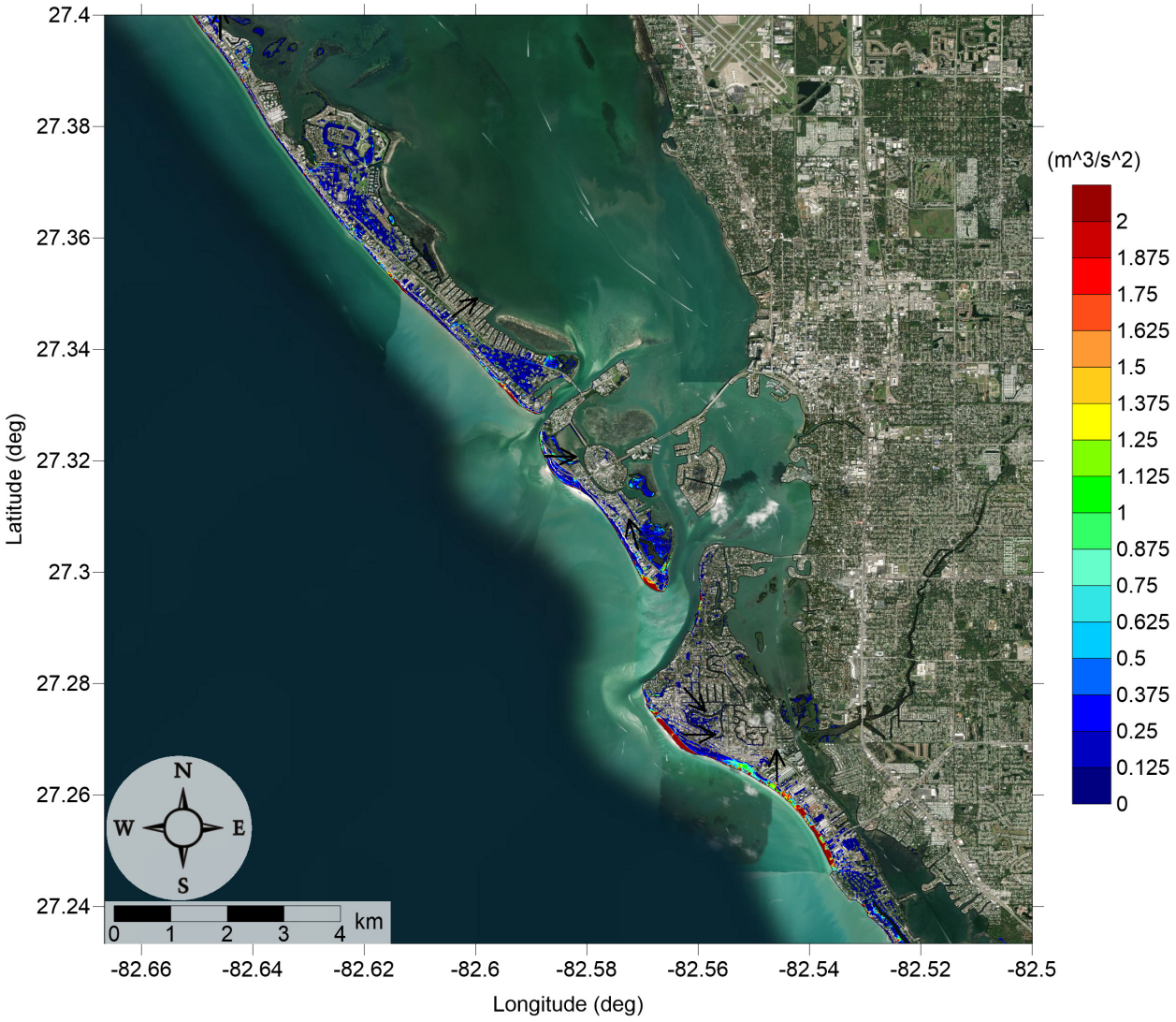

Figure 43: Maximum momentum flux (m^3/s^2) caused by the Probabilistic Submarine Landslide C in Siesta Key, FL. Arrows represent direction of maximum momentum flux. Contour drawn is the zero-meter contour for land elevation.

South Tampa Bay, FL
Probabilistic Submarine Landslide C
Maximum Inundation Depth

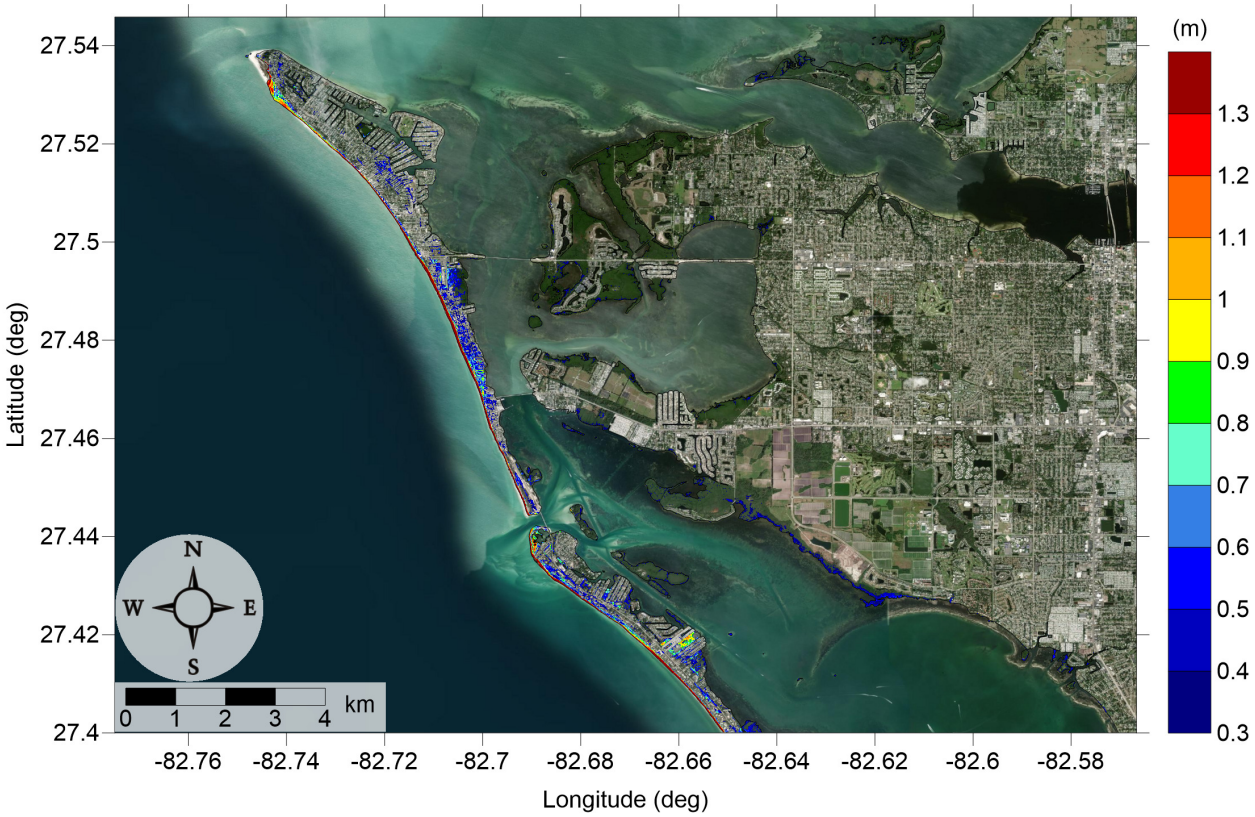

Figure 44: Maximum inundation depth (m) caused by the Probabilistic Submarine Landslide C in Anna Maria Island, FL. Contour drawn is the zero-meter contour for land elevation.

South Tampa Bay, FL
Probabilistic Submarine Landslide C
Maximum Inundation Depth

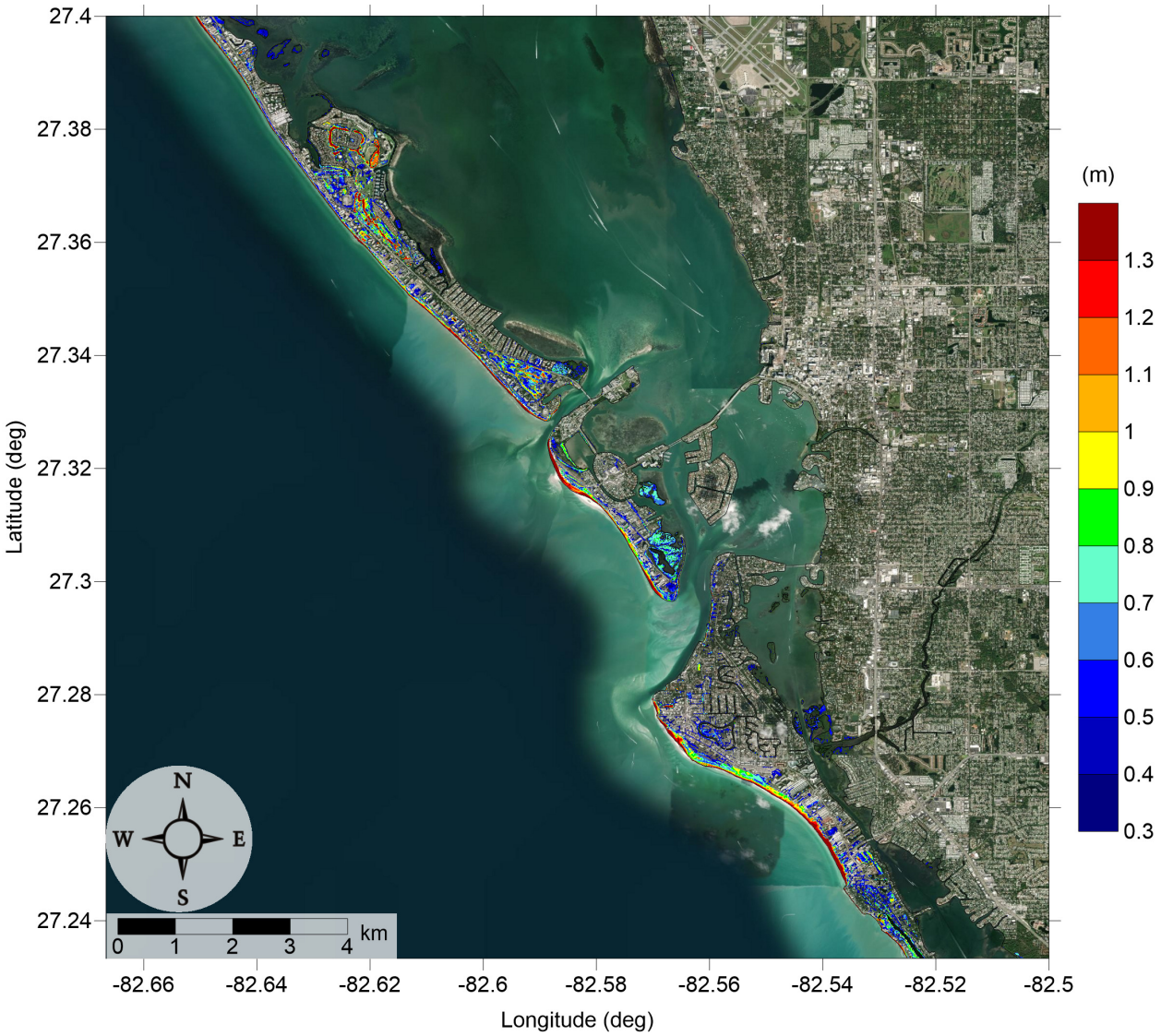

Figure 45: Maximum inundation depth (m) caused by the Probabilistic Submarine Landslide C in Siesta Key, FL. Contour drawn is the zero-meter contour for land elevation.

South Tampa Bay, FL
West Florida submarine landslide
Maximum Momentum Flux

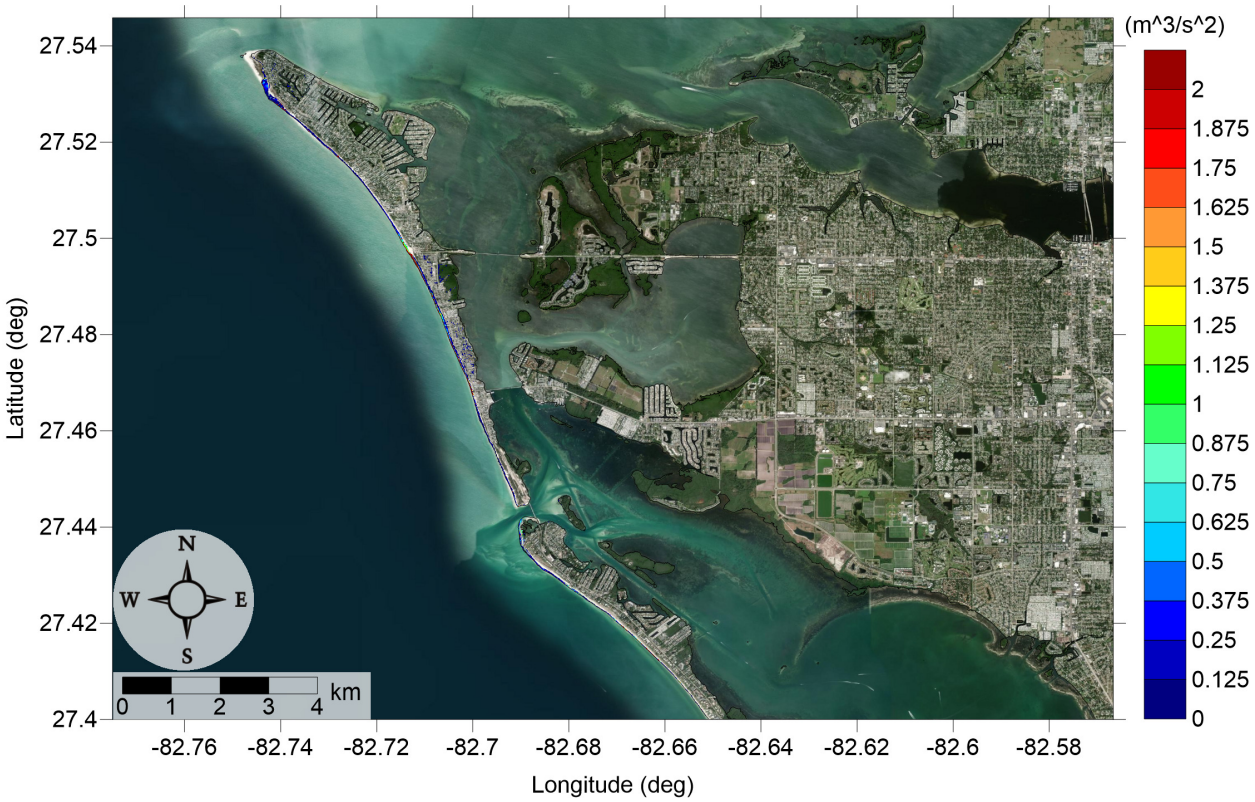

Figure 46: Maximum momentum flux (m^3/s^2) caused by the West Florida submarine landslide in Anna Maria Island, FL. Arrows represent direction of maximum momentum flux. Contour drawn is the zero-meter contour for land elevation.

South Tampa Bay, FL
West Florida submarine landslide
Maximum Momentum Flux

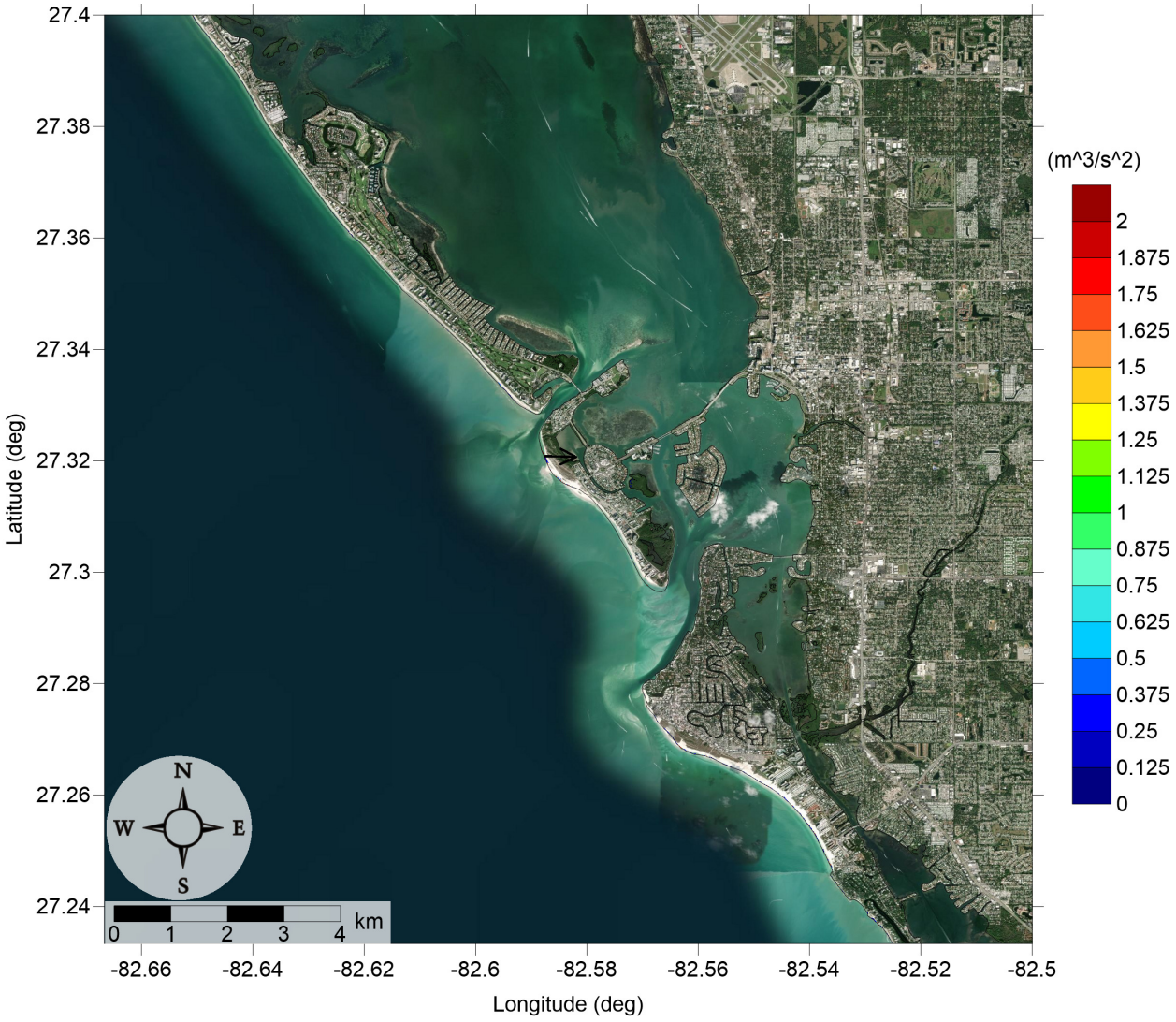

Figure 47: Maximum momentum flux (m^3/s^2) caused by the West Florida submarine landslide in Siesta Key, FL. Arrows represent direction of maximum momentum flux. Contour drawn is the zero-meter contour for land elevation.

South Tampa Bay, FL
West Florida submarine landslide
Maximum Inundation Depth

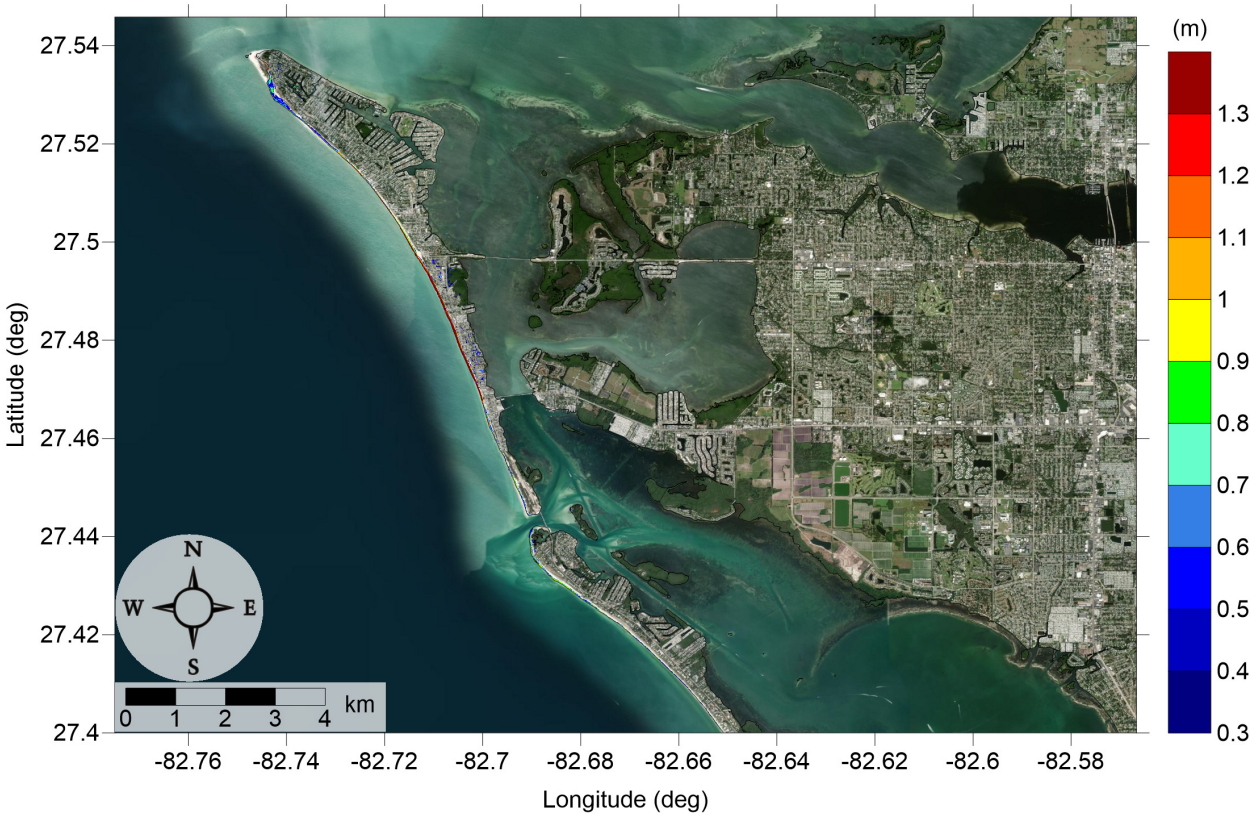

Figure 48: Maximum inundation depth (m) caused by the West Florida submarine landslide in Anna Maria Island, FL. Contour drawn is the zero-meter contour for land elevation.

South Tampa Bay, FL
West Florida submarine landslide
Maximum Inundation Depth

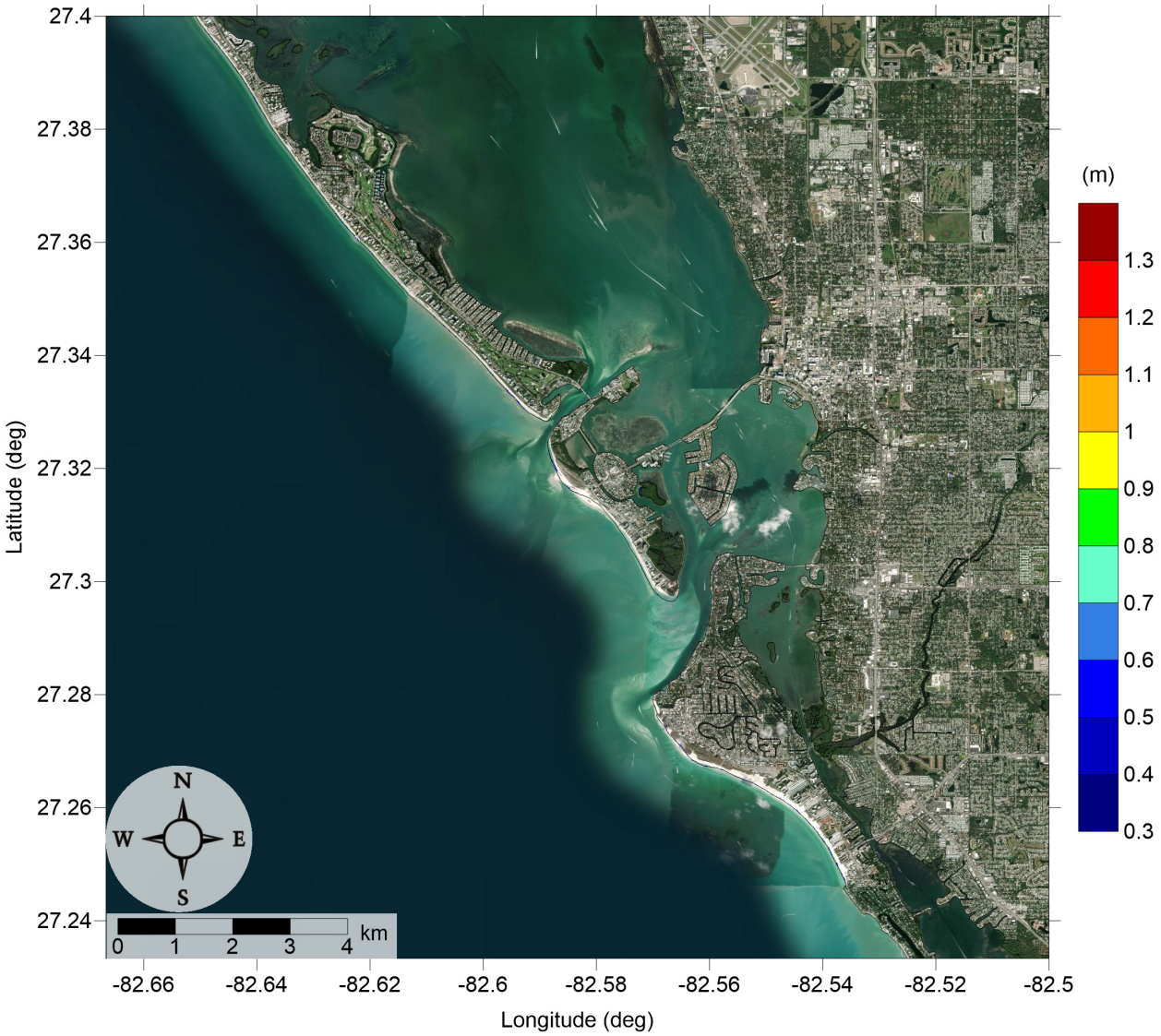

Figure 49: Maximum inundation depth (m) caused by the West Florida submarine landslide in Siesta Key, FL. Contour drawn is the zero-meter contour for land elevation.

South Tampa Bay, FL
Yucatán #3 submarine landslide
Maximum Momentum Flux

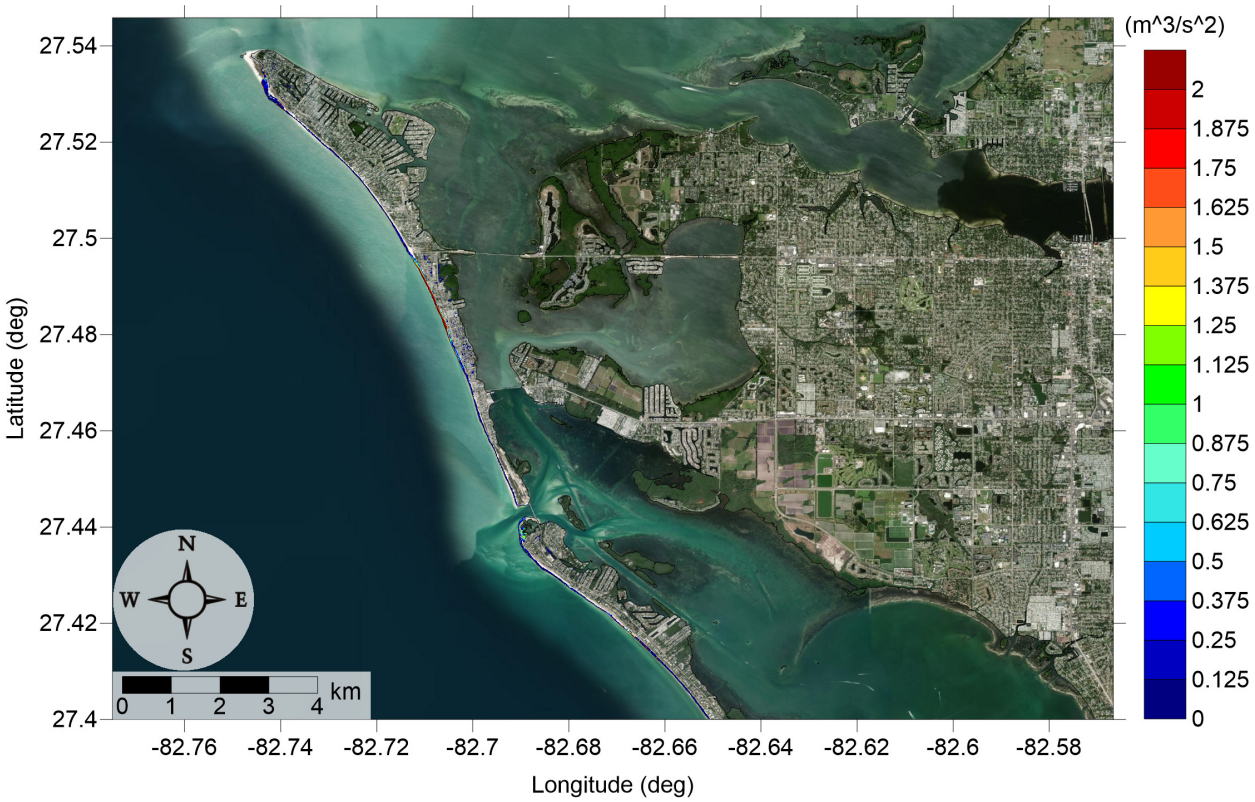

Figure 50: Maximum momentum flux (m^3/s^2) caused by the Yucatán #3 submarine landslide in Anna Maria Island, FL. Arrows represent direction of maximum momentum flux. Contour drawn is the zero-meter contour for land elevation.

South Tampa Bay, FL
Yucatán #3 submarine landslide
Maximum Momentum Flux

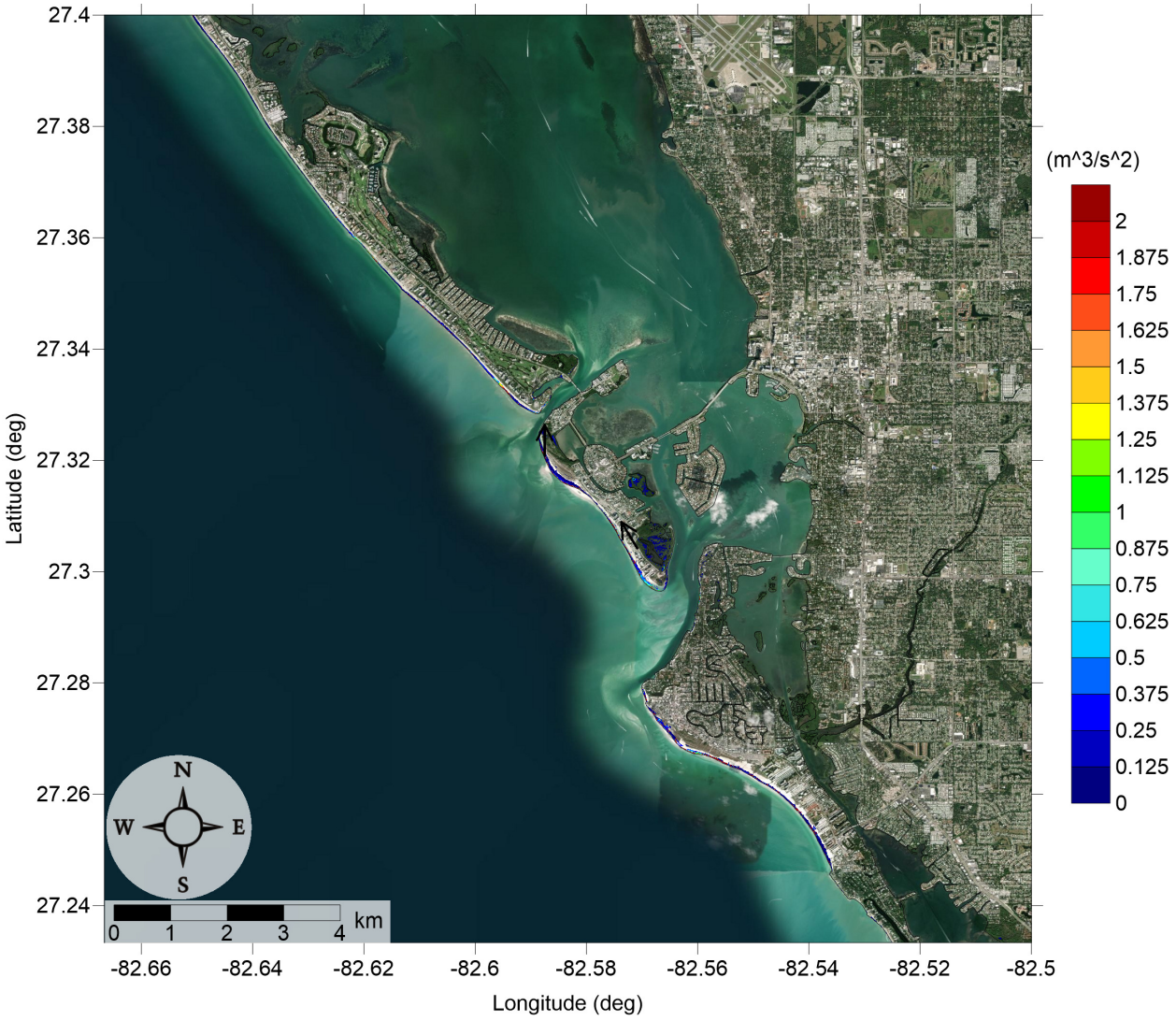

Figure 51: Maximum momentum flux (m^3/s^2) caused by the Yucatán #3 submarine landslide in Siesta Key, FL. Arrows represent direction of maximum momentum flux. Contour drawn is the zero-meter contour for land elevation.

South Tampa Bay, FL
Yucatán #3 submarine landslide
Maximum Inundation Depth

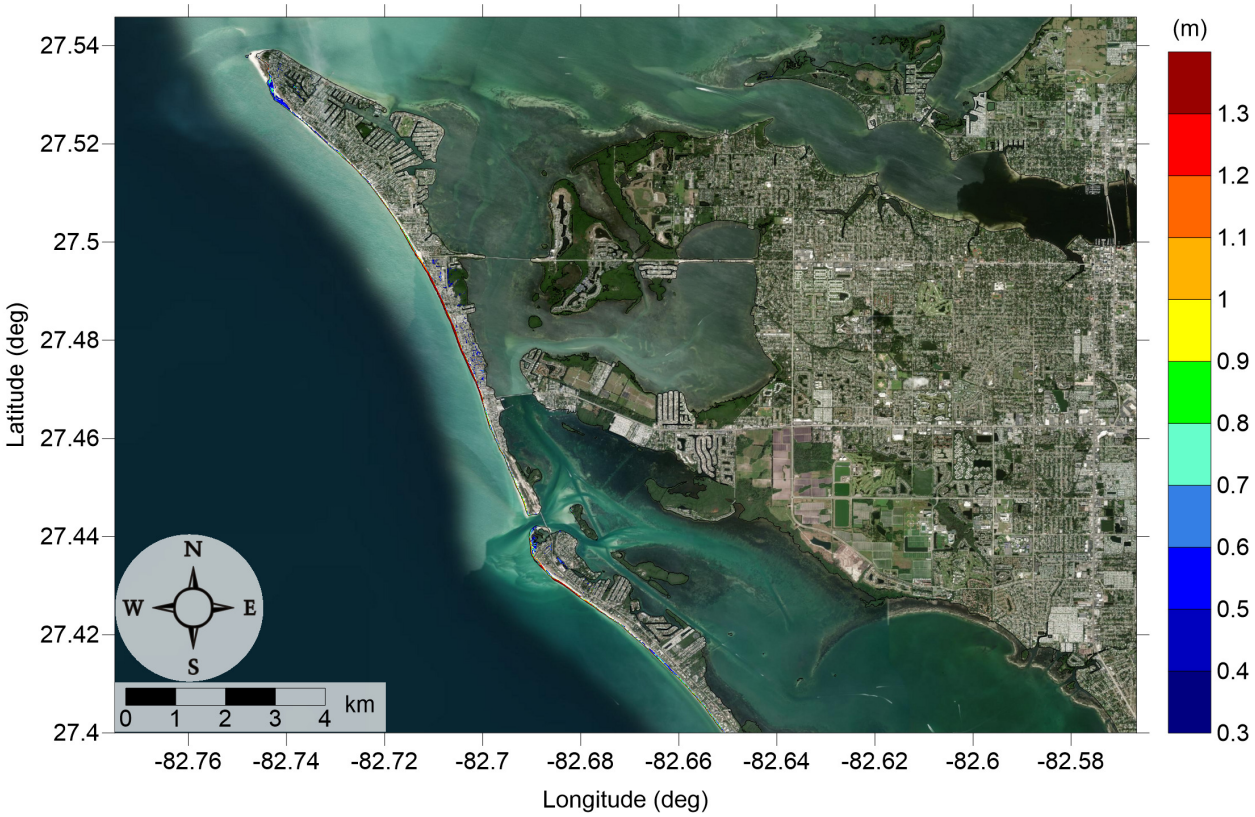

Figure 52: Maximum inundation depth (m) caused by the Yucatán #3 submarine landslide in Anna Maria Island, FL. Contour drawn is the zero-meter contour for land elevation.

South Tampa Bay, FL
Yucatán #3 submarine landslide
Maximum Inundation Depth

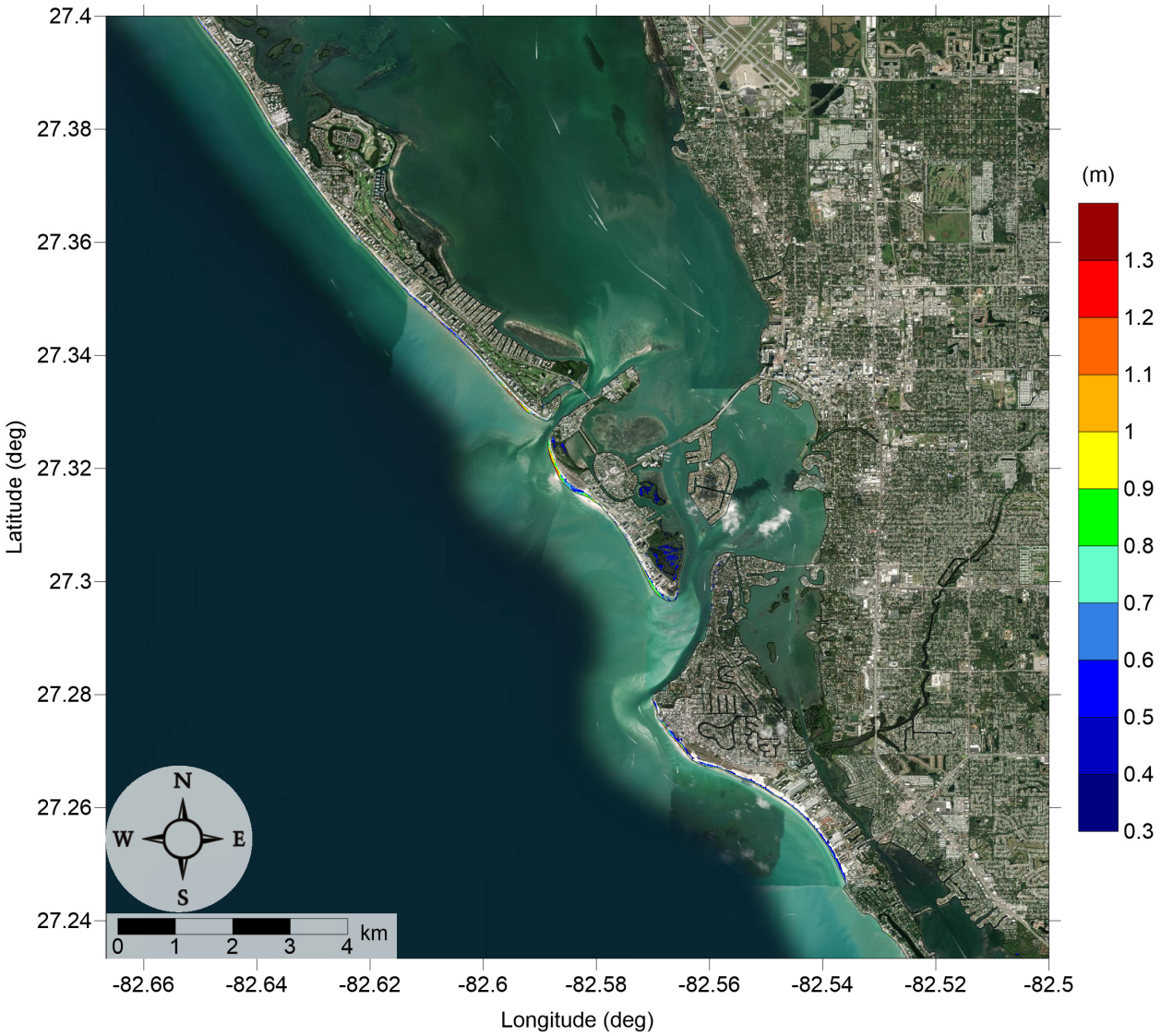

Figure 53: Maximum inundation depth (m) caused by the Yucatán #3 submarine landslide in Siesta Key, FL. Contour drawn is the zero-meter contour for land elevation.

South Tampa Bay, FL
Yucatán #5 submarine landslide
Maximum Momentum Flux

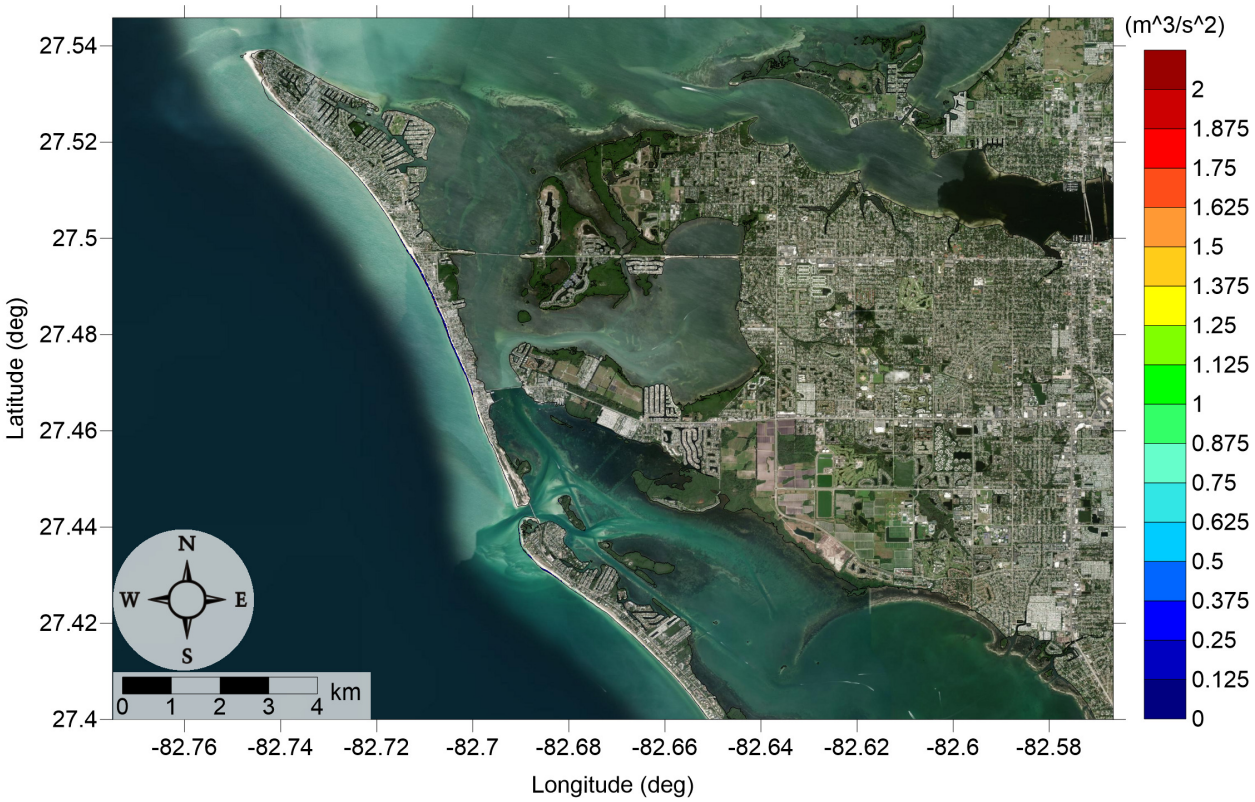

Figure 54: Maximum momentum flux (m^3/s^2) caused by the Yucatán #5 submarine landslide in Anna Maria Island, FL. Arrows represent direction of maximum momentum flux. Contour drawn is the zero-meter contour for land elevation.

South Tampa Bay, FL
Yucatán #5 submarine landslide
Maximum Momentum Flux

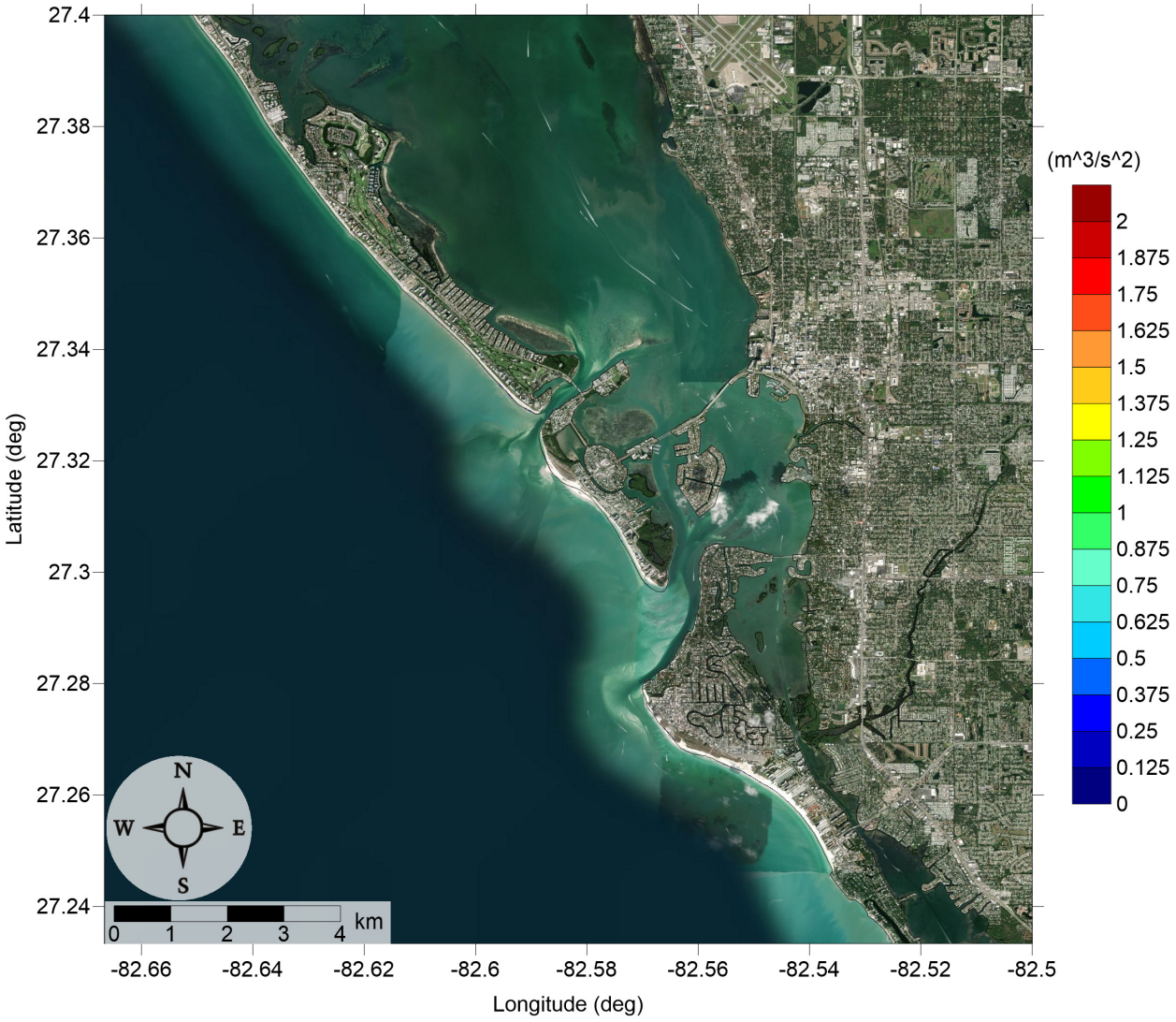

Figure 55: Maximum momentum flux (m^3/s^2) caused by the Yucatán #5 submarine landslide in Siesta Key, FL. Arrows represent direction of maximum momentum flux. Contour drawn is the zero-meter contour for land elevation.

South Tampa Bay, FL
Yucatán #5 submarine landslide
Maximum Inundation Depth

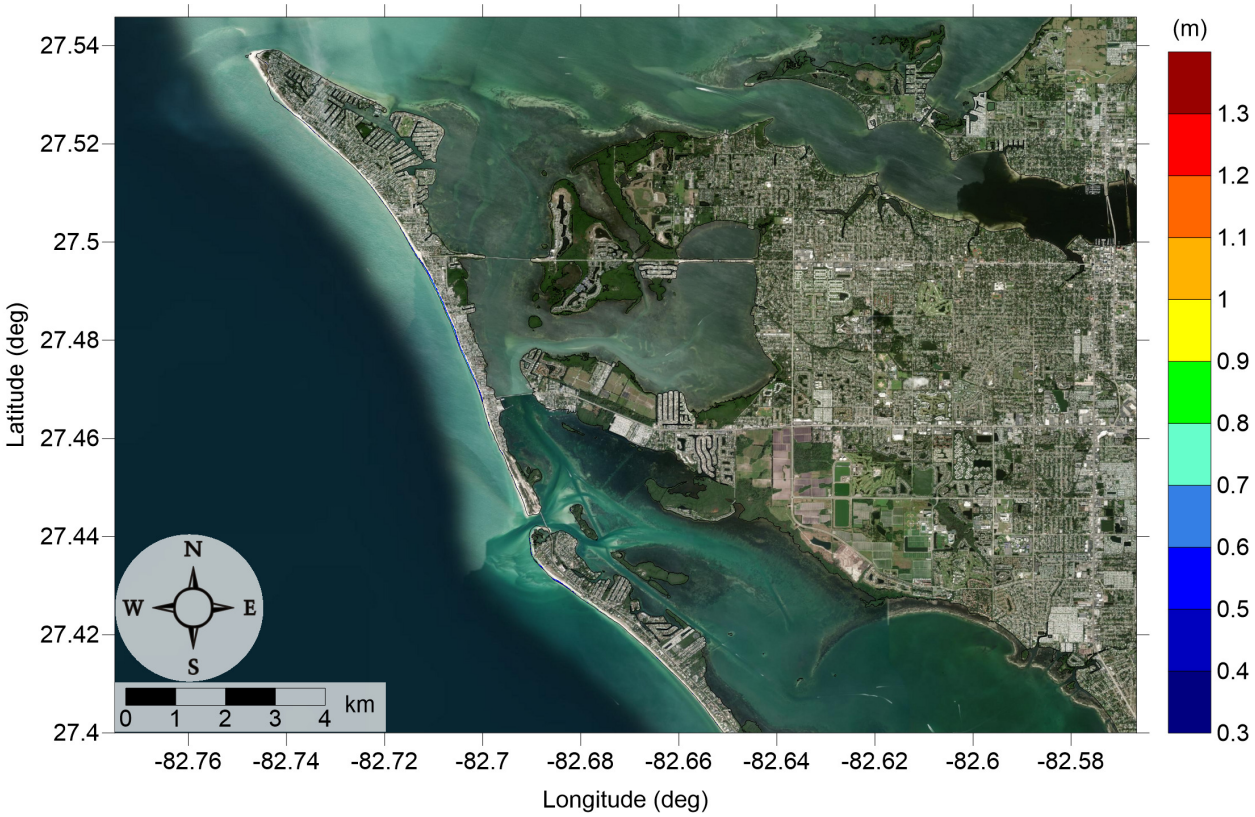

Figure 56: Maximum inundation depth (m) caused by the Yucatán #5 submarine landslide in Anna Maria Island, FL. Contour drawn is the zero-meter contour for land elevation.

South Tampa Bay, FL
Yucatán #5 submarine landslide
Maximum Inundation Depth

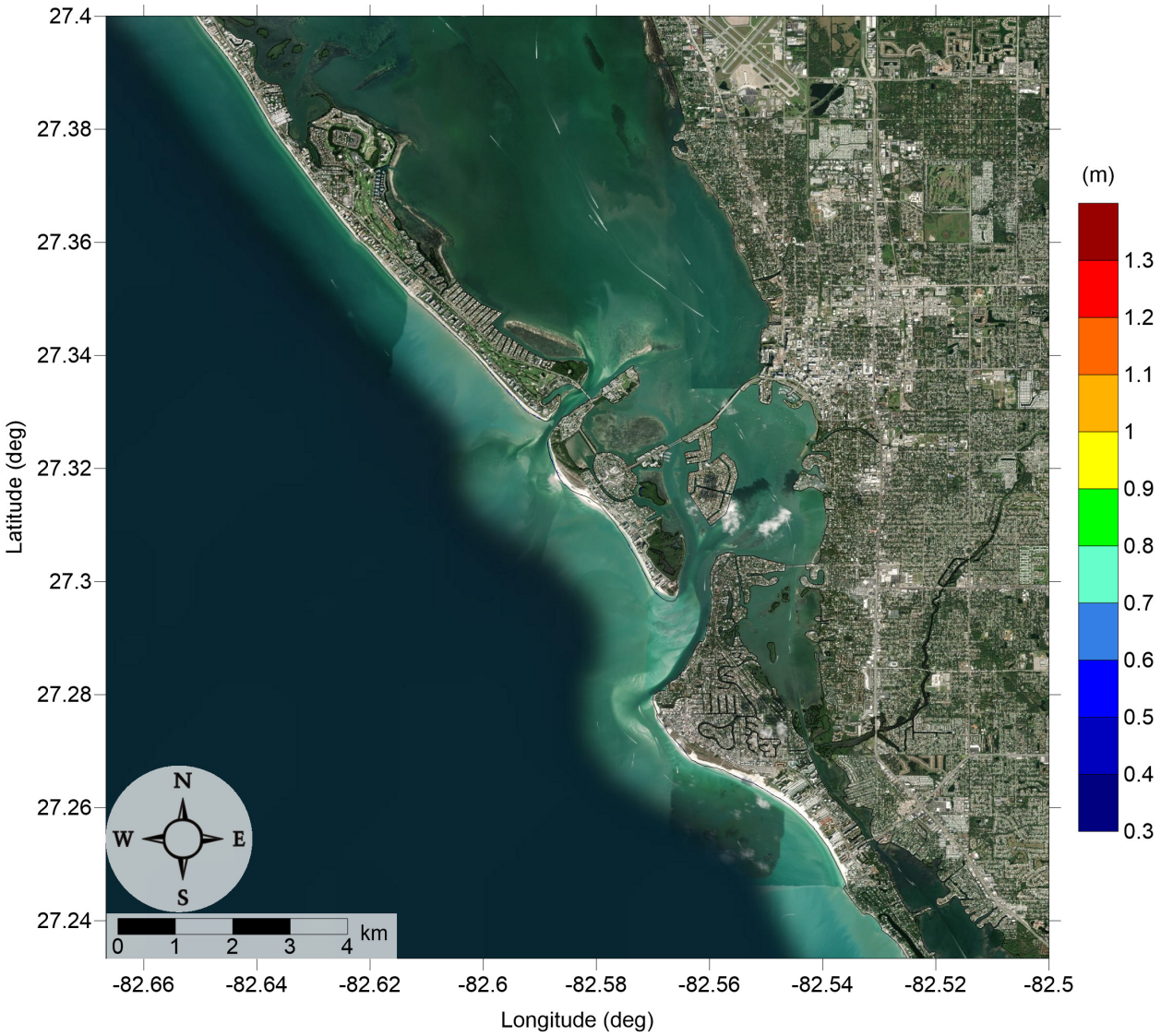

Figure 57: Maximum inundation depth (m) caused by the Yucatán #5 submarine landslide in Siesta Key, FL. Contour drawn is the zero-meter contour for land elevation.

South Tampa Bay, FL
All Sources
Maximum of Maximum Inundation Depth

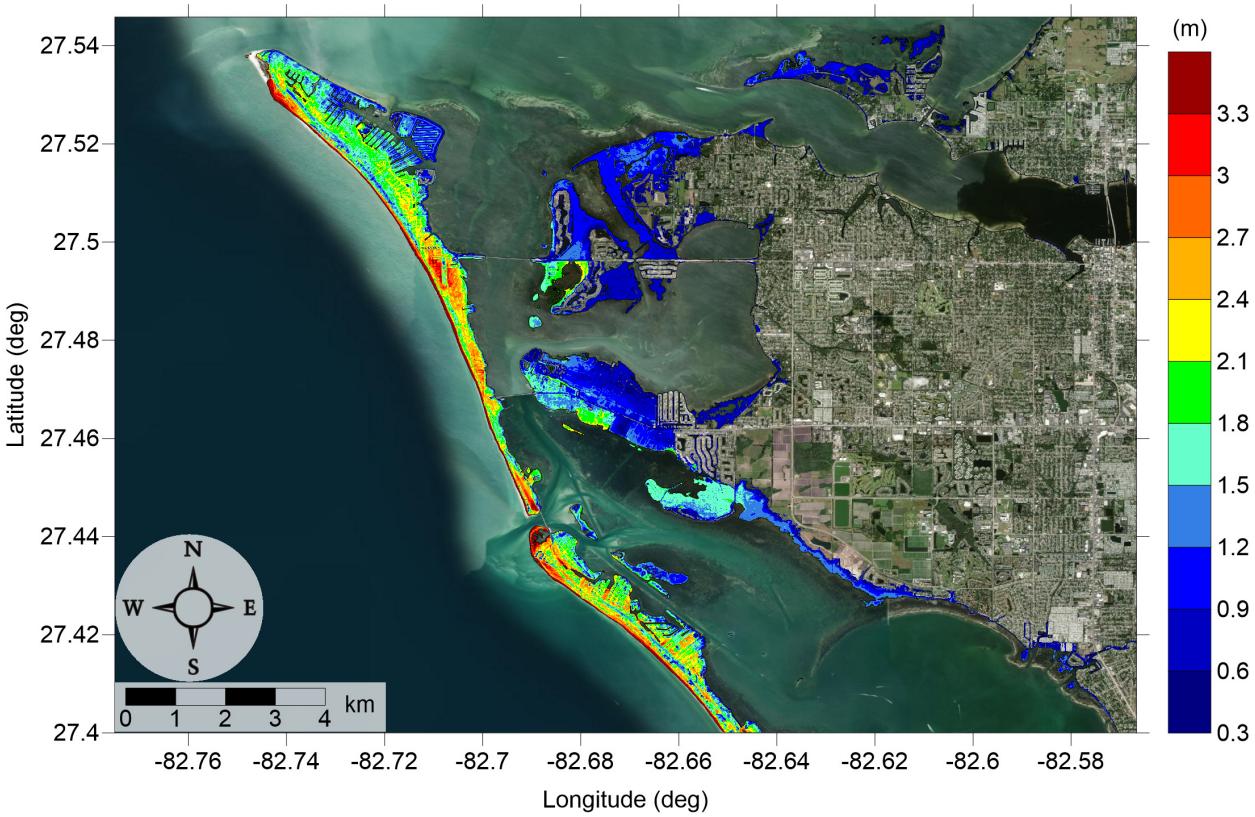

Figure 58: Maximum of maximums inundation depth (m) in Anna Maria Island, FL, calculated as the maximum inundation depth in each grid cell from an ensemble of all tsunami sources considered. Contour drawn is the zero-meter contour for land elevation.

South Tampa Bay, FL
All Sources
Maximum of Maximum Inundation Depth

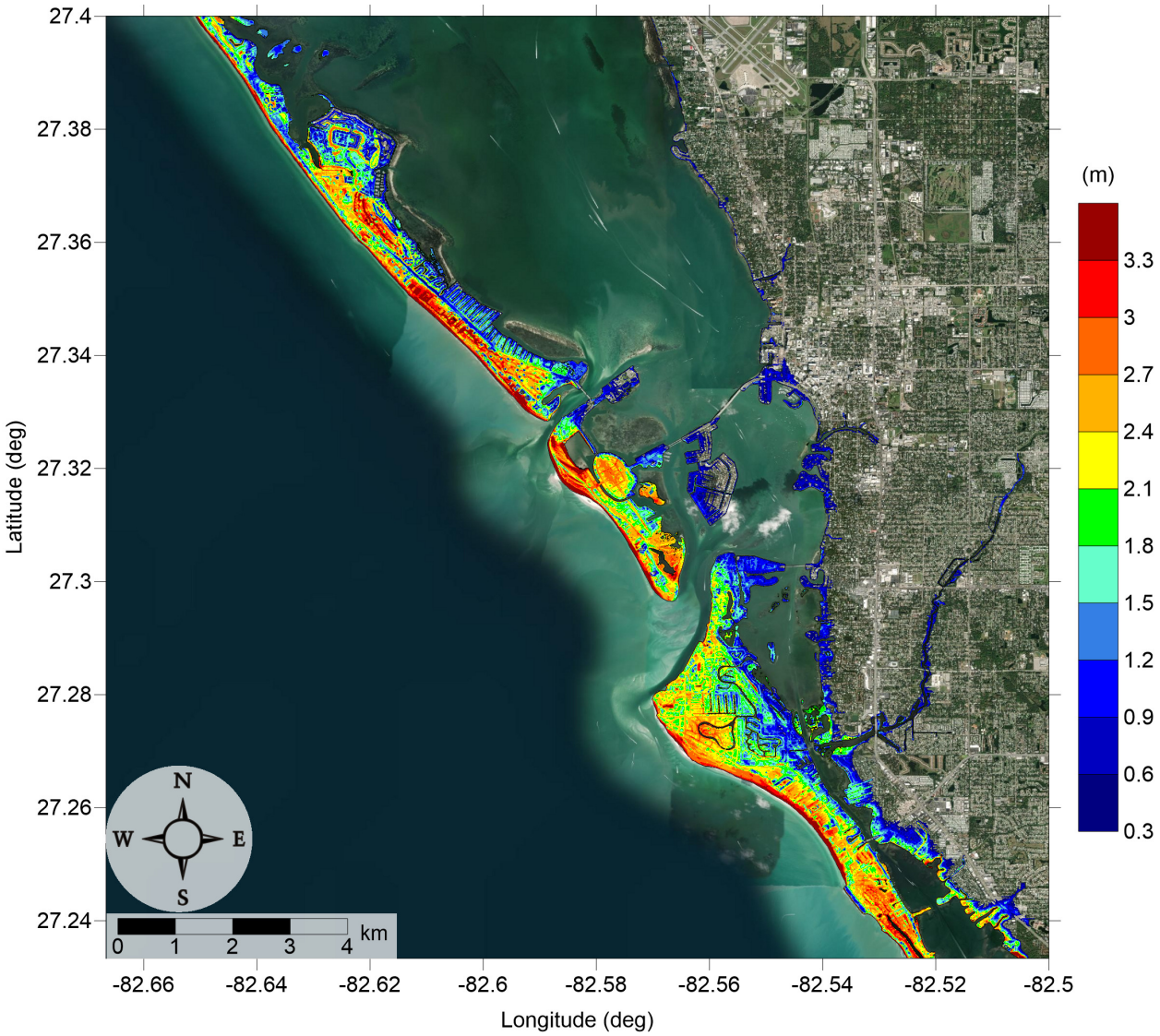

Figure 59: Maximum of maximums inundation depth (m) in Siesta Key, FL, calculated as the maximum inundation depth in each grid cell from an ensemble of all tsunami sources considered. Contour drawn is the zero-meter contour for land elevation.

South Tampa Bay, FL
All Sources
Maximum Inundation Depth by Source

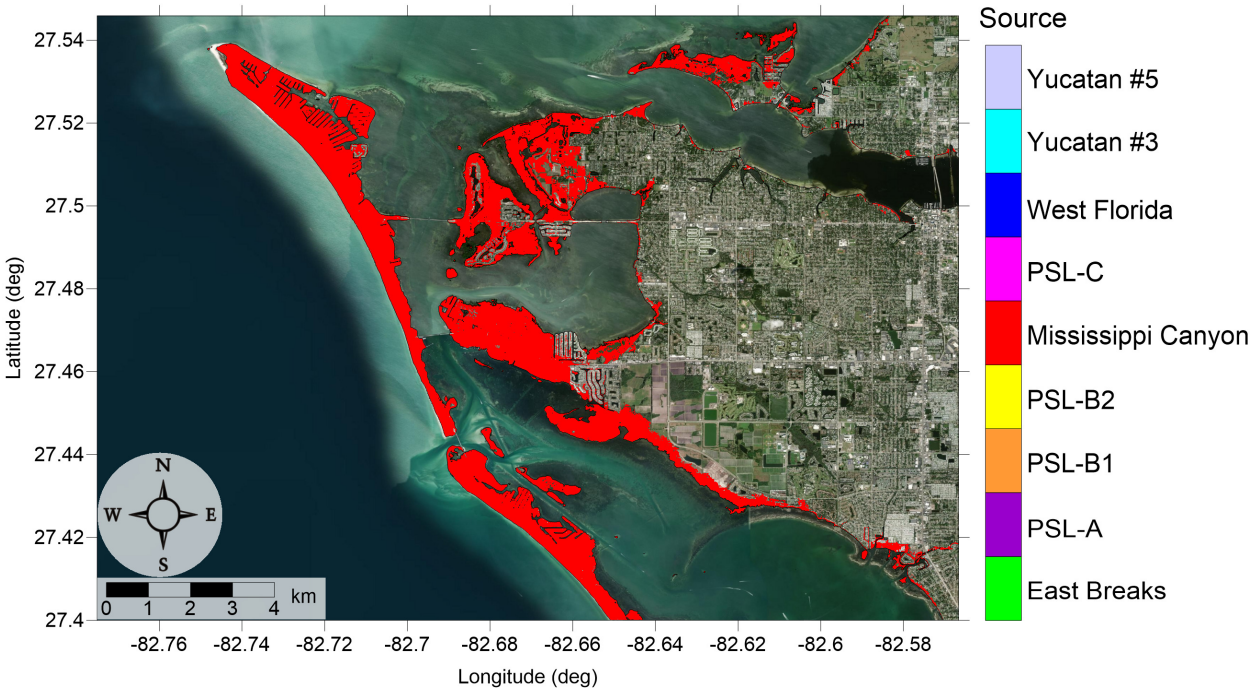

Figure 60: Indication of the tsunami source which causes the maximum of maximums inundation depth (m) in each grid cell from an ensemble of all tsunami sources in Anna Maria Island, FL. Contour drawn is the zero-meter contour for land elevation.

South Tampa Bay, FL
All Sources
Maximum Inundation Depth by Source

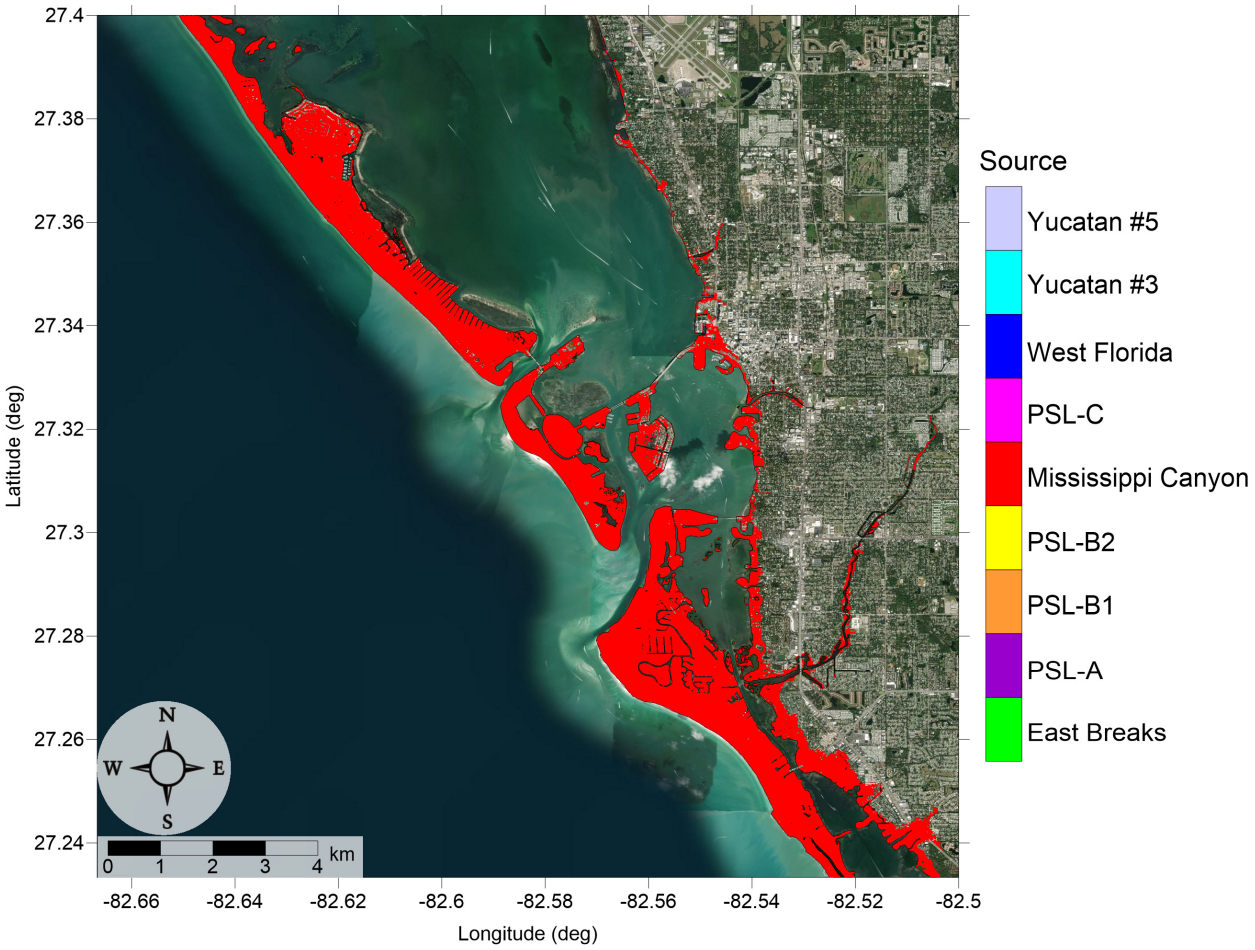

Figure 61: Indication of the tsunami source which causes the maximum of maximums inundation depth (m) in each grid cell from an ensemble of all tsunami sources in Siesta Key, FL. Contour drawn is the zero-meter contour for land elevation.

5 Tsunami and Hurricane Storm Surge Inundation

Due to the limitations on availability of high-resolution (1/3 arcsecond) DEMs, detailed inundation maps for all communities along the Gulf Coast are not yet possible. In an effort to develop a first-order estimate of potential tsunami inundation for those locations where detailed inundation maps have not yet been developed, we compare tsunami inundation modeled for the communities mentioned above to hurricane storm surge modeled data. The motivation for and implications of this approach are twofold. It provides a way to assess tsunami inundation in unmapped communities based on existing storm surge flood data and also relates the level of tsunami hazard to that of another hazard that is better defined in this region. Tsunamis are not well-understood as a threat along the Gulf Coast, making tsunami hazard mitigation efforts somewhat difficult. However, hurricane is a relatively well-understood threat in this region, and hurricane preparedness approaches are well-developed. As a result, comparisons of tsunami and hurricane storm surge inundation levels provide a more understandable and accessible idea of the level of hazard presented by potential tsunami events and can serve as a basis for tsunami preparedness efforts.

The hurricane storm surge data used here is available from the Sea, Lake, and Overland Surges from Hurricanes (SLOSH) model (http://www.nhc.noaa.gov/surge/slosh.php). The SLOSH model was developed by the National Weather Service (NWS) to provide estimates of storm surge heights caused by historical, predicted, or hypothetical hurricanes based on different values for atmospheric pressure, hurricane size, forward speed, and track. It uses a polar, elliptical, or hyperbolic grid for computations, leading to higher resolutions near coastal areas of interest. Some limitations of the SLOSH model should be acknowledged. Resolution of the model varies from tens of meters to a kilometer or more. Near the coastal communities of interest here, resolution is on the order of 1 km. Sub-grid scale water and topographic features such as channels, rivers, levees, and roads, are parameterized instead of being explicitly modeled. Despite these limitations, the hurricane storm surge data from the SLOSH model is currently the best data publicly available for our purposes, and efforts have been made to ensure the validity of the SLOSH data in performing comparisons with tsunami inundation.

The SLOSH MOM results provide the worst-case storm surge for a given hurricane category and initial tide level based on a set of model runs with various combinations of parameters such as forward speed, trajectory, and landfall location. To perform the storm surge and tsunami comparisons, SLOSH storm surge elevation data was first converted to meters and adjusted from the NAVD88 to the MHW vertical datum using NOAA's VDatum tool (http://vdatum.noaa.gov/). Due to the relatively low resolution of the SLOSH data as compared to the DEMs used for tsunami modeling, the SLOSH data was interpolated to 1/3 arcsecond (10 m) resolution using a kriging method. Inundation was then determined by subtracting land elevation from the storm surge elevation.

Here, an initial high tide level is used for the SLOSH MOM results in order to compare the worst-case tsunami inundation with a worst-case storm surge scenario. The high tide SLOSH MOM data includes effects of the highest predicted tide level at each location. In comparison, water elevations in the tsunami modeling are based on the MHW datum, which averages the high water levels over the National Tidal Datum Epoch (NTDE). Within the

GOM, tidal ranges are relatively small, with diurnal ranges on the order of 1.5 ft (0.5 m) for most of the communities studied here, and slightly higher at around 2.5 ft (0.8 m) for the west coast of Florida. Thus, differences between highest tide levels and the mean of the highest tide levels are expected to be relatively small, though local bathymetric effects combined with tidal effects can still be significant.

It should be noted that the updated Saffir-Simpson Hurricane Wind Scale which delineates hurricane categories 1-5 does not include storm surge as a component of the measure of hurricane intensity and that other methods may capture the physics of hurricane severity and damage in a more appropriate manner (e.g. Kantha [2006], Basco and Klentzman [2006], Irish and Resio [2010]). However, the SLOSH MOM results take into account thousands of scenarios for a given hurricane category, resulting in a composite worst-case storm surge scenario for each Saffir-Simpson hurricane category. Thus, since hurricane preparedness, storm surge evacuation zones, and hazard mitigation efforts are based on hurricane category assignment, we aim to determine the hurricane category which produces MOM storm surge inundation ζ_h that is a best match to the tsunami MOM inundation ζ_t. That is, we determine the hurricane category which satisfies

$$min_c(|\zeta_{h_c} - \zeta_t|), \qquad c = \text{Cat1,..,Cat5} \tag{1}$$

for each grid cell. The inundation level for the best-match category is denoted $\zeta_{h_{min}}$. The actual difference between hurricane and tsunami inundation levels $\Delta\zeta = \zeta_{h_{min}} - \zeta_t$ then indicates how close of a match the best-match category actually is. Thus, positive values of $\Delta\zeta$ indicate where hurricane storm surge inundation is higher than tsunami inundation, and negative values indicate where tsunami inundation is higher. A common local practice in tsunami modeling is to only consider inundation above a threshold of 0.3 m (1 ft) [Horrillo et al., 2011, 2015]. This is due to the extensive flat and low-lying elevation found along the Gulf Coast. All depths are calculated for tsunami inundation modeling, but inundation less than 0.3 m (1 ft) is considered negligible here for inundation mapping purposes. Thus, comparisons are only made where either the tsunami or hurricane MOM inundation is at least 0.3 m (1 ft). Results for the two selected Gulf Coast communities are given in the following subsections. It is possible that tsunami inundation zone has no hurricane flooding, therefore matching with hurricane category cannot be made.

5.1 Jamaica Beach, TX

Fig. 20 shows the MOM tsunami inundation affecting Jamaica Beach, TX. Tsunami inundates most of the island facing the GOM. Overall water depth exhibits decreasing trend from oceanfront toward the bay, with maximum over 2 m. North half of City of Jamaica Beach and the communities around Lake Como and Eckert Bayou which are north of Steward Rd do not suffer from any inundation, though major evacuation route, San Luis Pass Rd is severely flooded. Since this area is far from both San Luis Pass and Galveston Bay entrance, tsunami energy has been significantly dissipated when waves reach the bay side of the island (lee side), therefore the West Bay, all three Deer Islands, Tiki Island and Flamingo Isles are well protected. Mississippi Canyon landslide is responsible for the MOM inundation (see Fig. 21).

The hurricane category which best matches the tsunami inundation in Jamaica Beach, TX is shown in Fig. 62, and Fig. 63 shows $\Delta\zeta$ for the best-matching hurricane category satisfying Eq. 1. The hurricane category that best matches tsunami inundation closely follows the MOM tsunami inundation trend, where Category 3 appears near the beach, Category 2 runs parallel and takes up the middle section of the island, and the rest is occupied by Category 1. The difference between hurricane flooding and tsunami inundation is mostly within ± 1 m.

Jamaica Beach, TX
All Sources
SLOSH Storm Surge and MOM Tsunami Inundation Comparison

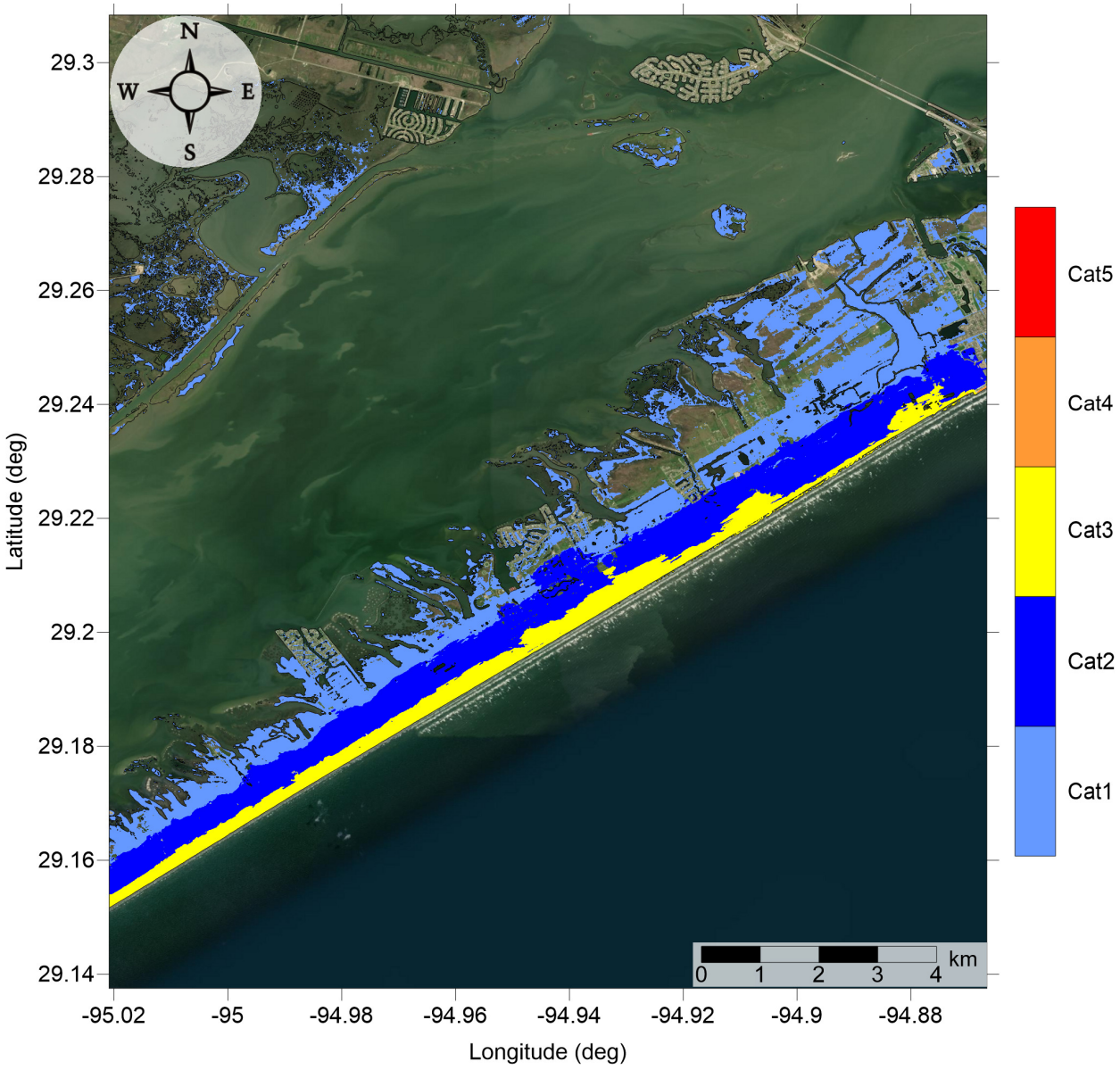

Figure 62: Hurricane category which produces inundation at high tide that best matches the MOM tsunami inundation shown in Figure 20 for Jamaica Beach, TX. The contours drawn and labeled are at -5 m, -10 m, and -15 m levels.

Jamaica Beach, TX
All Sources
SLOSH Storm Surge and MOM Tsunami Inundation Comparison

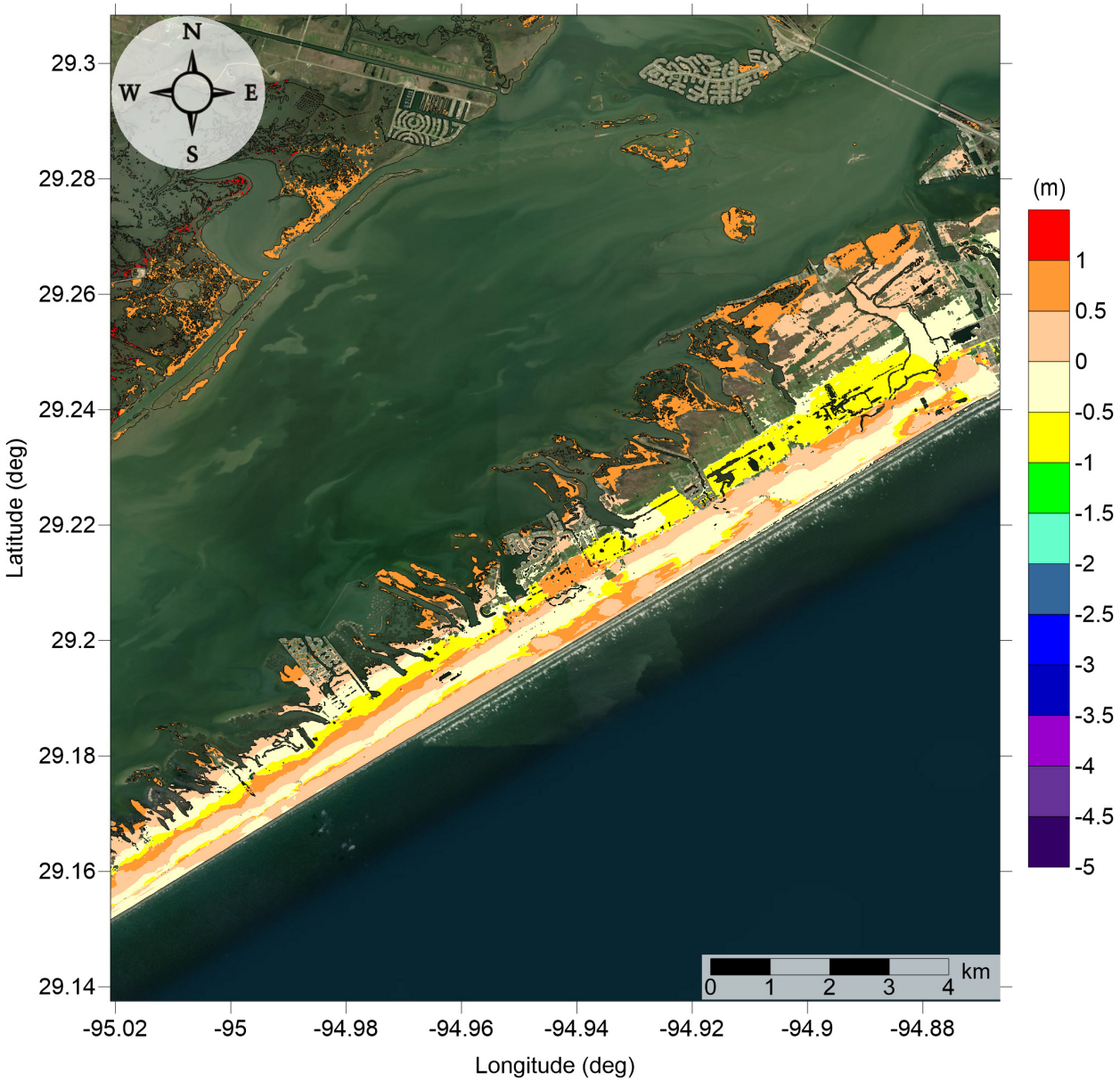

Figure 63: Actual difference $\Delta\zeta$ (in meters) between SLOSH MOM storm surge inundation and MOM tsunami inundation for the best-match hurricane category shown in Figure 62 for Jamaica Beach, TX. Note that negative values indicate where tsunami inundation is higher than hurricane inundation, and pale colors indicate relatively good agreement between tsunami and storm surge inundation, i.e. $|\Delta\zeta| \leq 0.5$ m. The contours drawn and labeled are at -5 m, -10 m, and -15 m levels.

5.2 South Tampa Bay, FL

Fig. 58 and Fig. 59 show the MOM tsunami inundation affecting South Tampa Bay mapping area (Anna Maria Island, Longboat Key, Lido Key and Siesta Key). On a regional scale, the wide Florida GOM continental shelf provides significant damping of tsunami waves so that the majority of Florida west coast shows less tsunami inundation, based on previous findings [e.g. Horrillo et al., 2015, 2018]. Overall the barrier islands provide ample protection for the mainland against tsunami inundation. While inundation depth at the barrier island ranges from 1 to over 3 m from the lee side to the GOM, the mainland is mostly less than 2 m. Cortez, FL is relatively more flooded than other mainland cities due to its proximity to Longboat Pass, where the communities around Cortez Rd west of 119 St W see inundation as high as 2 m. Another high risk mainland area are the communities south of the Phillippi Creek, where inundation depth is mainly below 2 m but can reach to as high as 3 m. The Mississippi Canyon landslide is responsible for the MOM inundation (see Fig. 60).

The hurricane category which best matches the tsunami inundation in this area is shown in Fig. 64. $\Delta\zeta$ for the best-match hurricane category satisfying equation 1 is shown in Fig. 66, and Fig. 65 and Fig. 67. The matching hurricane category distribution closely reflects that of tsunami inundation. Category 3 is only seen on a thin strip near the barrier island beach, and the majority of the barrier islands are split between Category 2 and 1. Mainland coastal communities that are inundated have water depth mostly equivalent to Category 1, except for south of Phillippi Creek where Category 2 appears. The difference between hurricane flooding and tsunami inundation $\Delta\zeta$ is generally within $\pm$ 0.5 m for the barrier islands, however, at the mainland the difference reaches larger than 1 m, which means storm surge inundation depth is higher since tsunami waves generally cannot reach as far into the bays.

South Tampa Bay, FL
All Sources
SLOSH Storm Surge and MOM Tsunami Inundation Comparison

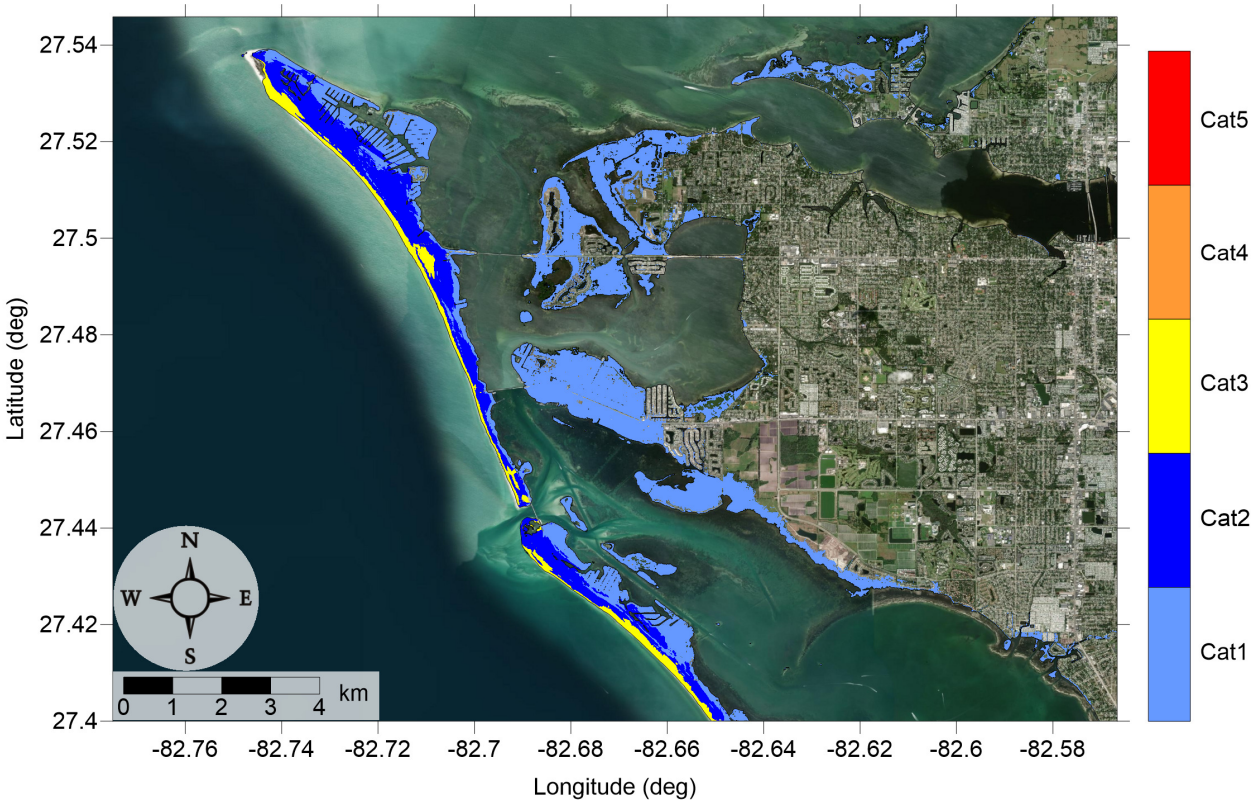

Figure 64: Hurricane category which produces inundation at high tide that best matches the MOM tsunami inundation shown in Figure 58 for Anna Maria Island, FL. The contours drawn and labeled are at -5 m, -10 m, and -15 m levels.

South Tampa Bay, FL
All Sources
SLOSH Storm Surge and MOM Tsunami Inundation Comparison

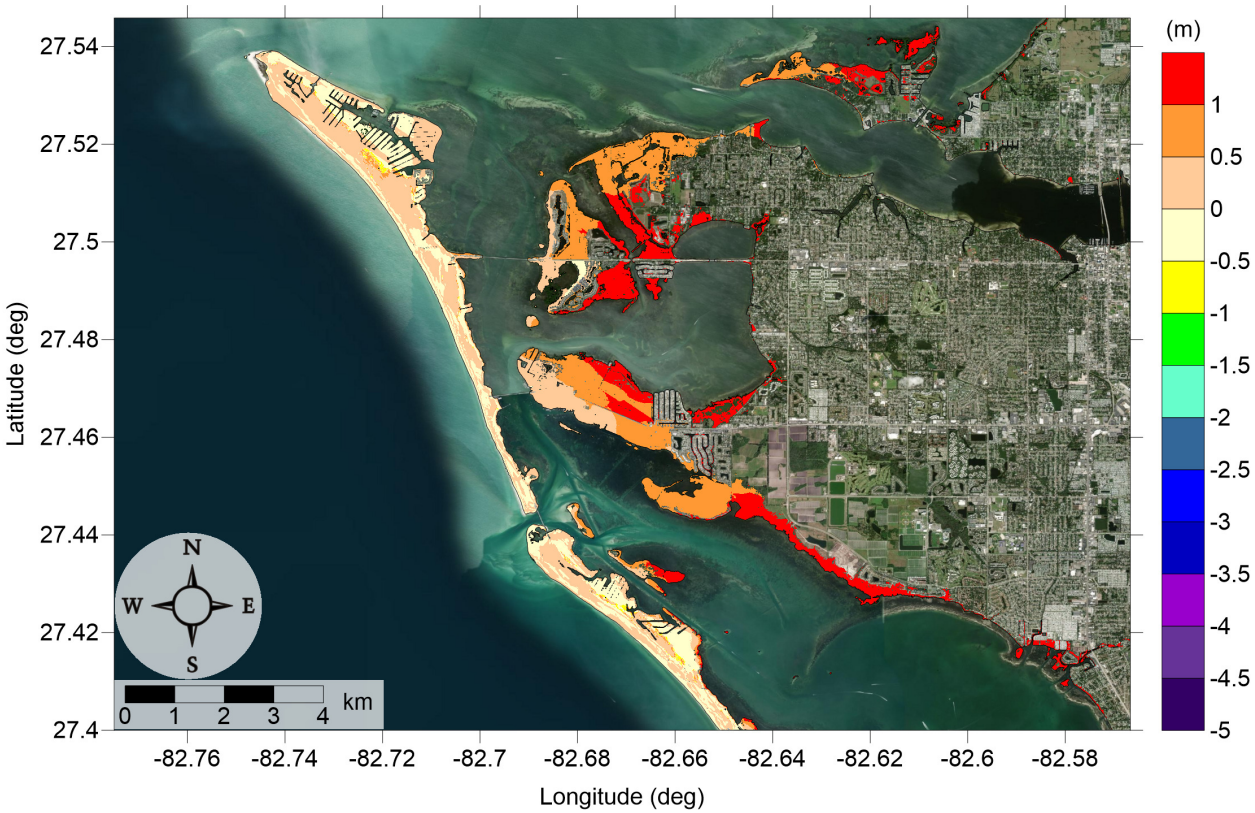

Figure 65: Actual difference $\Delta\zeta$ (in meters) between SLOSH MOM storm surge inundation and MOM tsunami inundation for the best-match hurricane category shown in Figure 64 for Anna Maria Island, FL. Note that negative values indicate where tsunami inundation is higher than hurricane inundation, and pale colors indicate relatively good agreement between tsunami and storm surge inundation, i.e. $|\Delta\zeta| \leq 0.5$ m. The contours drawn and labeled are at -5 m, -10 m, and -15 m levels.

Siesta Key, FL
All Sources
SLOSH Storm Surge and MOM Tsunami Inundation Comparison

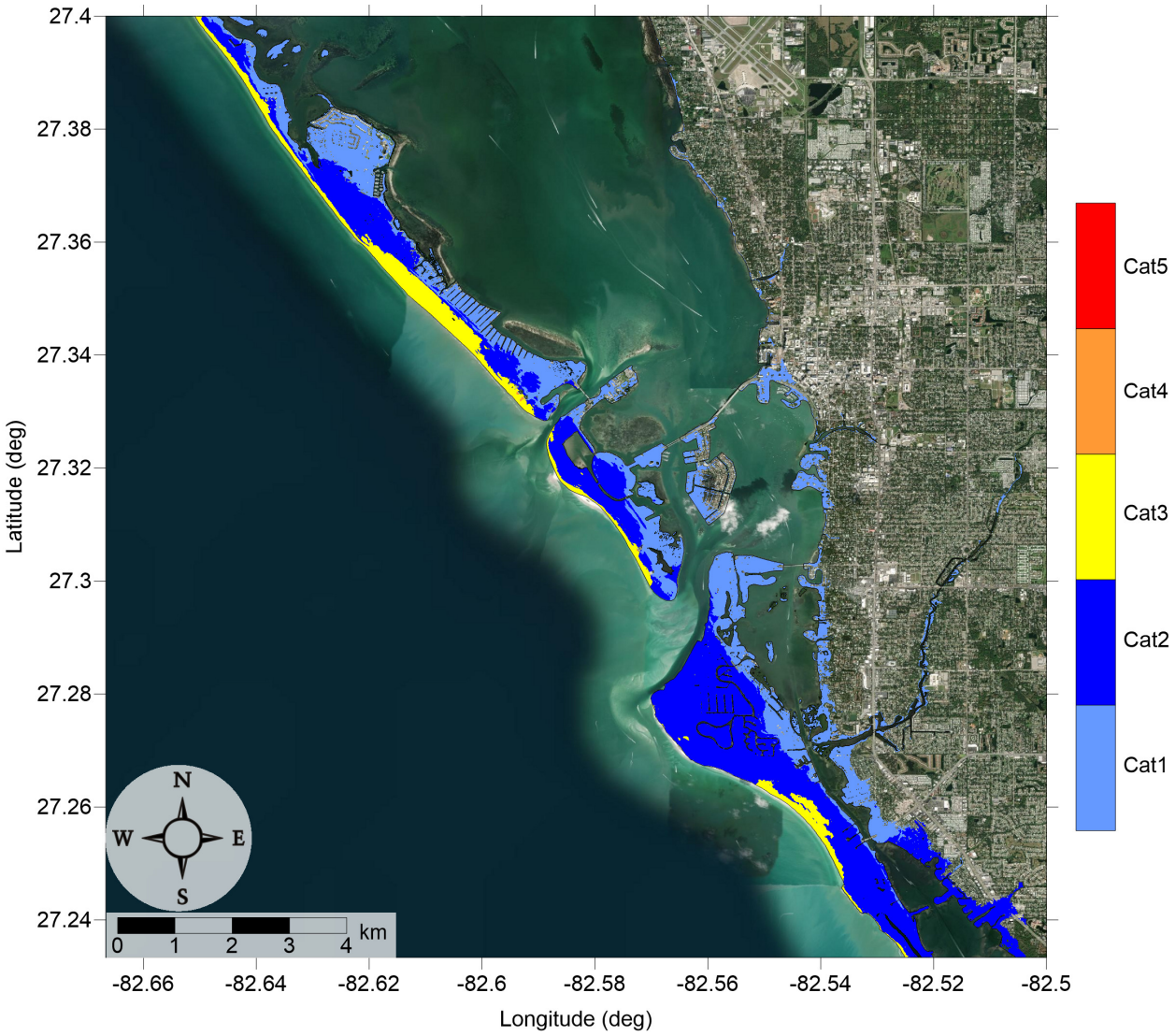

Figure 66: Hurricane category which produces inundation at high tide that best matches the MOM tsunami inundation shown in Figure 59 for Siesta Key, FL. The contours drawn and labeled are at -5 m, -10 m, and -15 m levels.

Siesta Key, FL
All Sources
SLOSH Storm Surge and MOM Tsunami Inundation Comparison

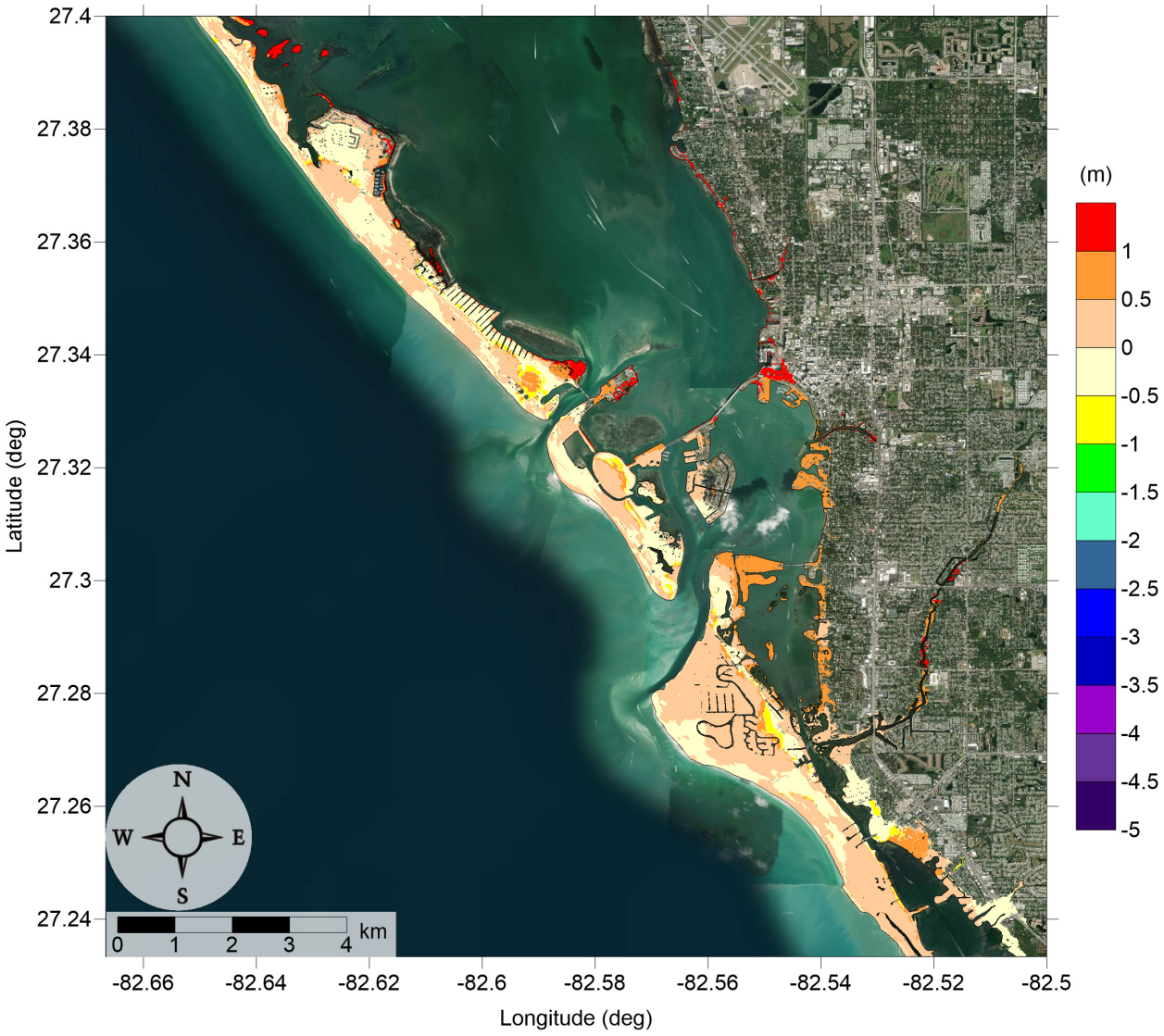

Figure 67: Actual difference $\Delta\zeta$ (in meters) between SLOSH MOM storm surge inundation and MOM tsunami inundation for the best-match hurricane category shown in Figure 66 for Siesta Key, FL. Note that negative values indicate where tsunami inundation is higher than hurricane inundation, and pale colors indicate relatively good agreement between tsunami and storm surge inundation, i.e. $|\Delta\zeta| \leq 0.5$ m. The contours drawn and labeled are at -5 m, -10 m, and -15 m levels.

6 Tsunami Maritime Products

Accurate estimates of tsunami wave amplitude do not necessarily equate to the prediction of localized damaging currents in a basin or harbor [Lynett et al., 2012]. Furthermore, damage potential in ports is strongly related to the current speed. Therefore, tsunami hazard mitigation products need to be advanced to predict damage potential in basins or harbors. Recent tsunamis have shown that the maritime community requires additional information and guidance about tsunami hazards and post-tsunami recovery [Wilson et al., 2012, 2013]. To accomplish mapping and modeling activities to meet NTHMP's planning/response purposes for the maritime community and port emergency management and other customer requirements, it is necessary to continue the process to include maritime products in our current inundation map development. These maritime products will help identify impact specifically on ship channels, bay inlets, harbors, marinas, and oil infrastructures (e.g., designated lightering and oil tanker waiting zones).

In this study, Jamaica Beach, TX and South Tampa Bay, FL are added to the maritime portfolio, where tsunami hazard maritime products such as tsunami current magnitude, vorticity, safe/hazard zones are included.

Lynett et al. [2014] complied a general relationship between tsunami current speed and harbor damage based on observational data, in which the current speed is divided into four ranges of damaging potential, 0 - 3 knots means unharmful currents, 3 - 6 knots corresponds to minor-to-moderate damage, 6 - 9 knots moderate-to-major damage, and over 9 knots extreme damage. Since the extent of damage is very location-dependent, to make the text concise, we associate 0 - 3 knots to unharmful currents, 3 - 6 knots to minor damage, 6 - 9 knots to moderate damage, and finally over 9 knots to major damage. The four levels are denoted with white, blue, yellow and red colors, respectively, for all the velocity contour plots within our velocity maritime products.

Using this damage-to-speed relationship, we have plotted the maximum of maximum depth-averaged velocity for each computational subdomain of the two new communities. Fig. 68 shows the minimum offshore safe depth (approximately 200 m or 100 fathoms), and the maximum of maximum velocity magnitude contour plot across the entire Gulf of Mexico (15 arcsecond resolution) for all landslide scenarios (Eastbreaks, PSL-A, PSL-B1, PSL-B2, Mississippi Canyon, PSL-C, West Florida, Yucatán #3 and Yucatán #5). Potential damaging currents ($>$ 3 knots, blue, yellow and red areas) tend to be present in most of the area shallower than the minimum offshore safe depth. However, damaging currents could reach areas deeper than 200 m close to most of the landslide generation regions. Major damaging currents ($>$ 9 knots, red) can be expected in most of the landslide generation regions, in the continental shelf adjacent to Mississippi Canyon, offshore northwest Florida, and Yucatán shelf. Moderate ($>$ 6 knots and $<$ 9 knots, yellow) damaging current areas are scattered over the continental shelf, but mostly close to areas with major damage currents.

All locations
All Sources
Maximum of Maximum Velocity Magnitude

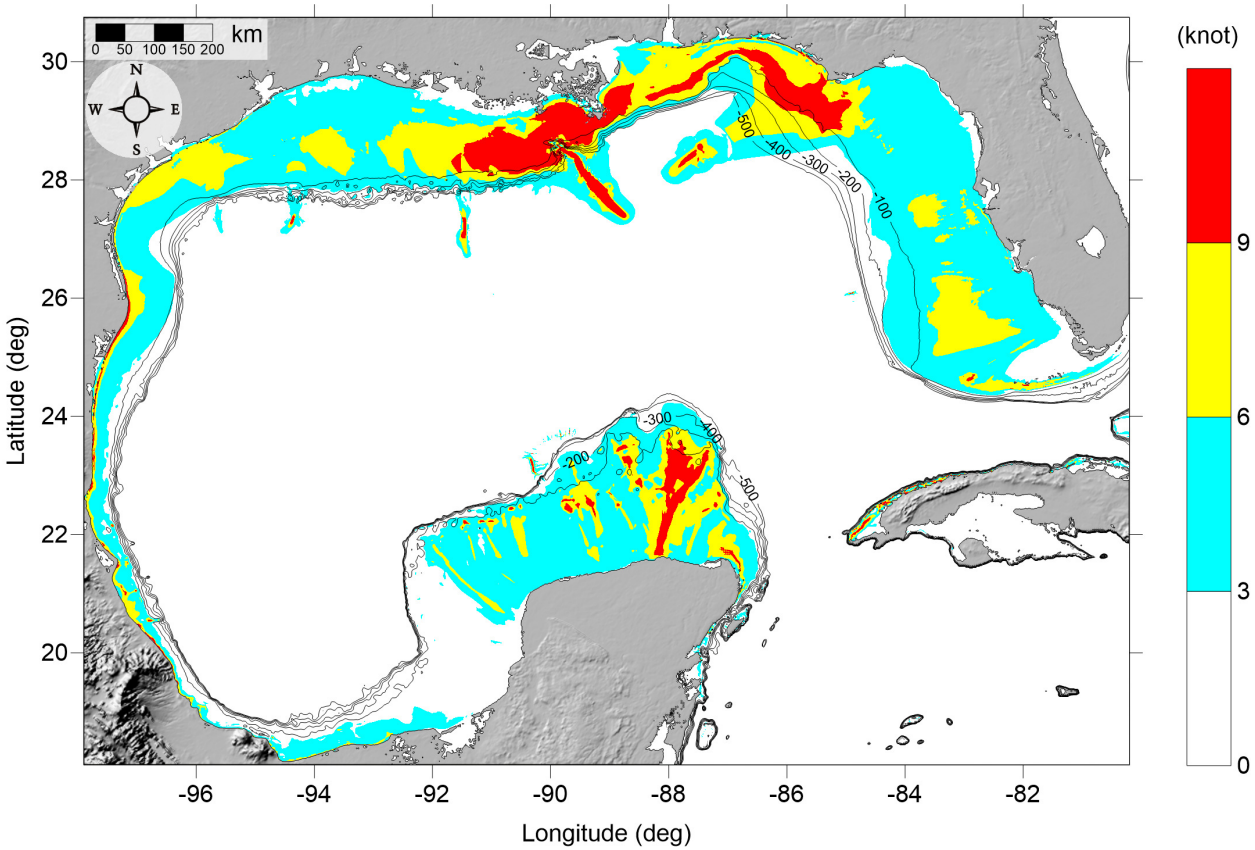

Figure 68: Maximum of maximum velocity magnitude contour in GOM for all landslide scenarios and all locations.

The MOM velocity magnitude (damaging potential) contour maps and the MOM vorticity magnitude contour maps for the finer computational subdomains of Jamaica Beach, TX and South Tampa Bay, FL are presented from Fig. 69 to Fig. 80.

General trends can be observed from the different grid levels of the MOM velocity for Jamaica Beach, TX. Most of offshore region is expected to have minor damaging currents, with moderate damaging currents occurring along the coastline and jetties. Fig. 70 shows the MOM velocity magnitude contour plot result for the Jamaica Beach area, and Galveston Bay Entrance (Grid 3 - 1 arcsecond resolution). Moderate damaging currents (> 6 knots) can be expected adjacent to the Galveston island GOM coastline. There is no damaging currents inside the Galveston Bay, however, there are some minor damaging current locations in the bay entrance and the Galveston Ship Channel.

In South Tampa Bay, FL, the situation is different from Jamaica Beach, TX. Moderate damaging currents (> 6 knots) can be seen more than 100 km offshore. Major damaging current (> 9 knots) area appears as a thin strip near the barrier islands and at bay entrances, e.g., Tampa Bay and Longboat Pass. In the interior bays and channels, the tsunami currents are less severe which can be used as shelter to minimize tsunami impact.

Vorticity distribution, on the other hand, displays similar patterns between the two locations, where high vorticity appears around the barrier island, and are more intense near the bay entrances.

6.1 Jamaica Beach, TX

Jamaica Beach, TX
All Sources
Maximum of Maximum Velocity Magnitude

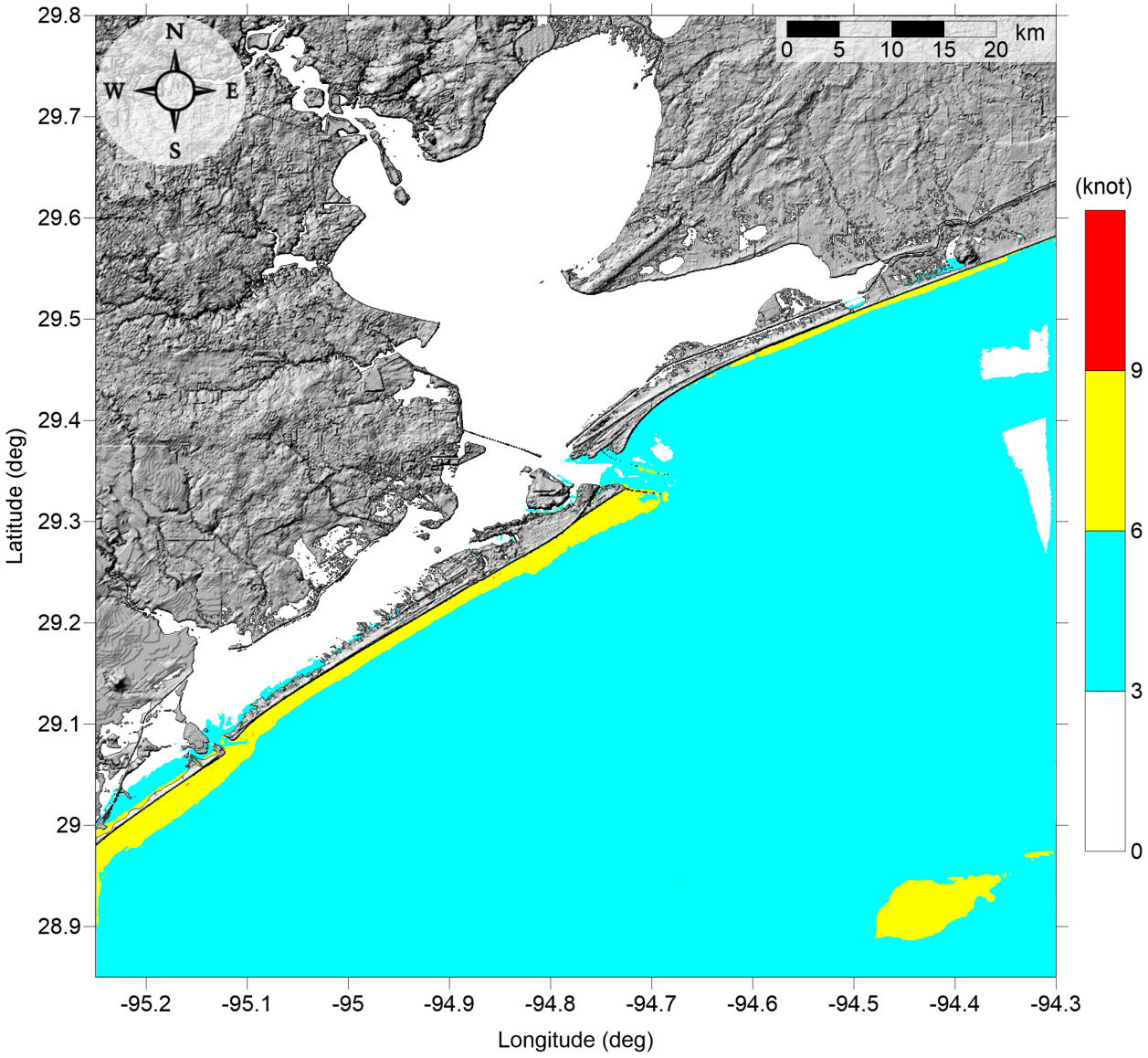

Figure 69: Maximum of maximum velocity magnitude contour in Jamaica Beach, TX (Grid 2 - 3 arcsecond) for all landslide scenarios.

Jamaica Beach, TX
All Sources
Maximum of Maximum Velocity Magnitude

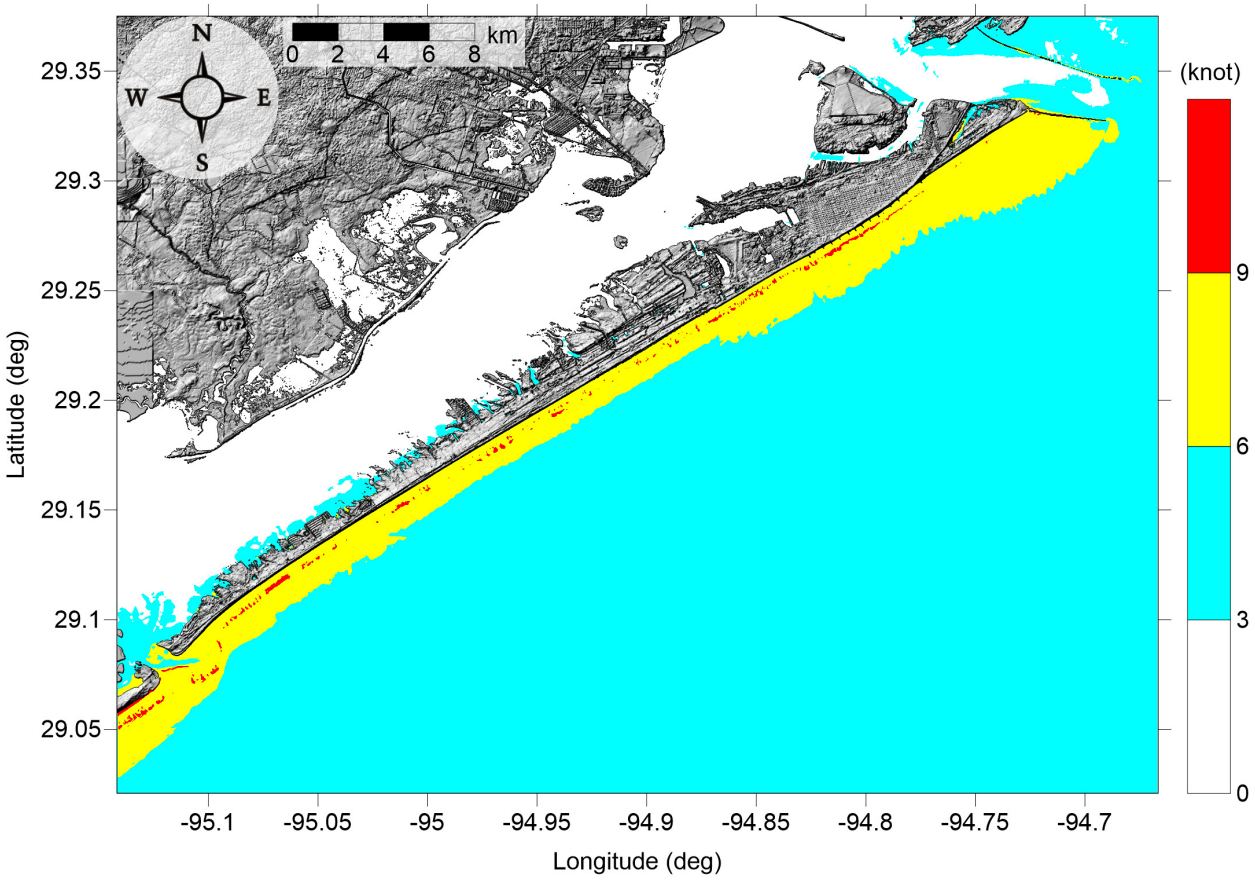

Figure 70: Maximum of maximum velocity magnitude contour in Jamaica Beach, TX (Grid 3 - 1 arcsecond) for all landslide scenarios.

Jamaica Beach, TX
All Sources
Maximum of Maximum Velocity Magnitude

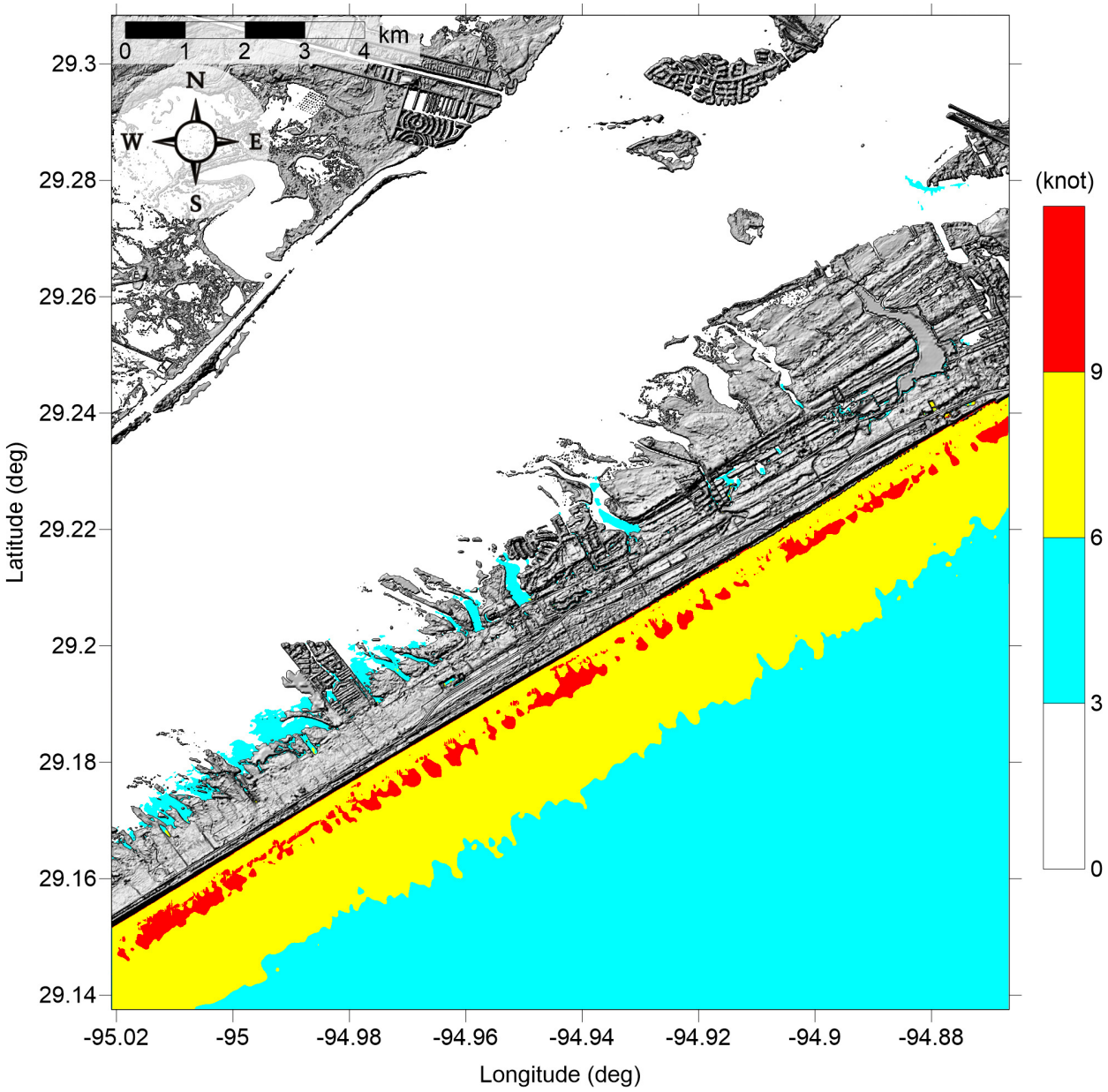

Figure 71: Maximum of maximum velocity magnitude contour in Jamaica Beach, TX (Grid 4 - 1/3 arcsecond) for all landslide scenarios.

Jamaica Beach, TX
All Sources
Maximum of Maximum Vorticity Magnitude

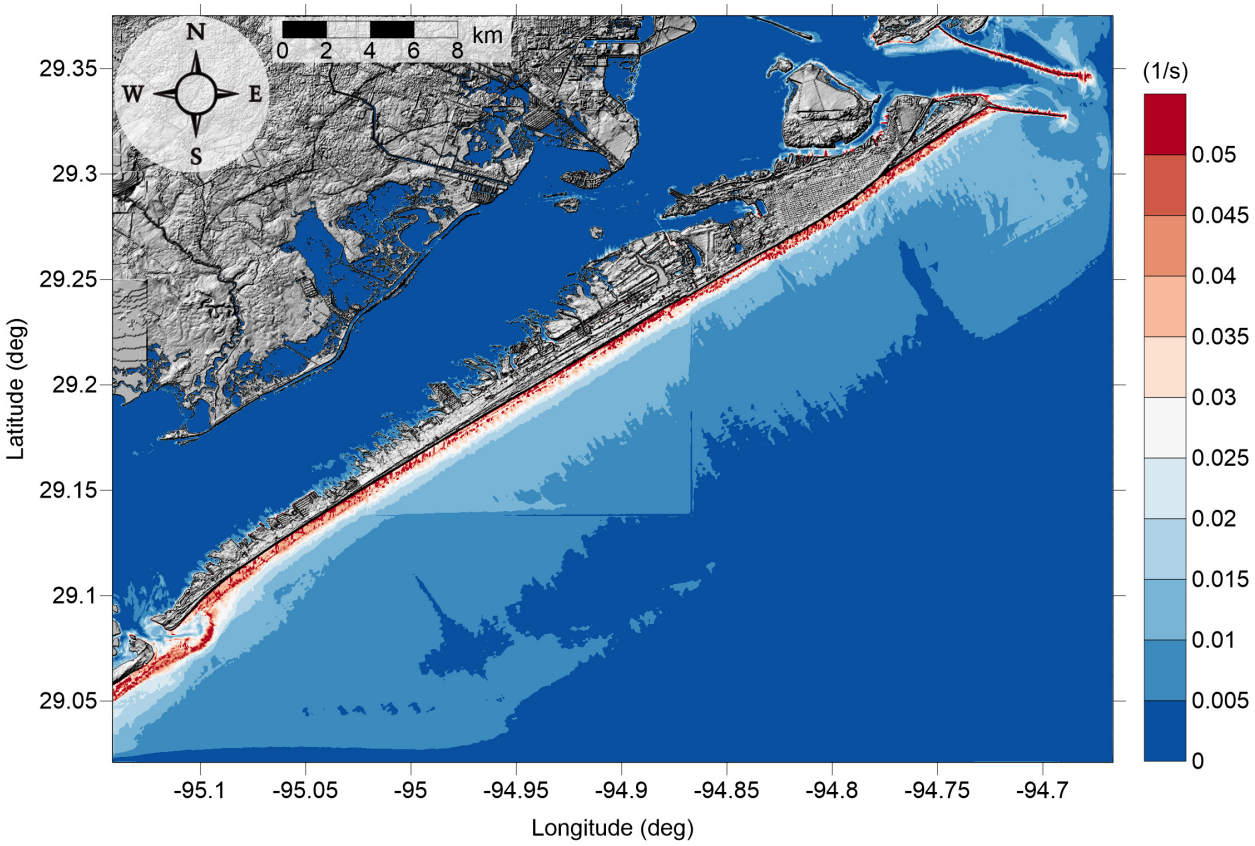

Figure 72: Maximum of maximum vorticity magnitude contour in Jamaica Beach, TX Grid 3 (1 arcsecond) for all landslide scenarios.

Jamaica Beach, TX
All Sources
Maximum of Maximum Vorticity Magnitude

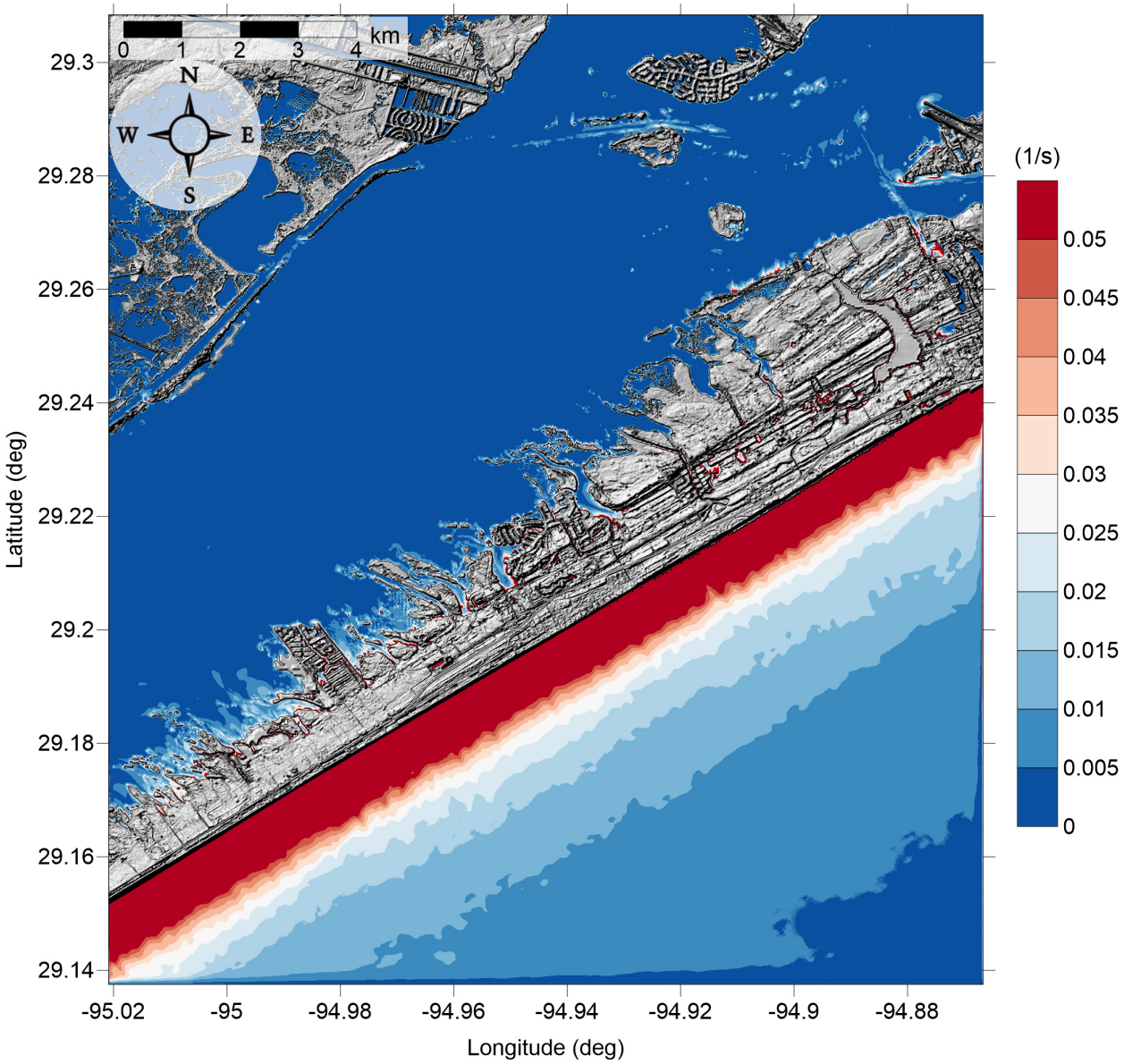

Figure 73: Maximum of maximum vorticity magnitude contour in Jamaica Beach, TX Grid 4 (1/3 arcsecond) for all landslide scenarios.

6.2 South Tampa Bay, FL

South Tampa Bay, FL
All Sources
Maximum of Maximum Velocity Magnitude

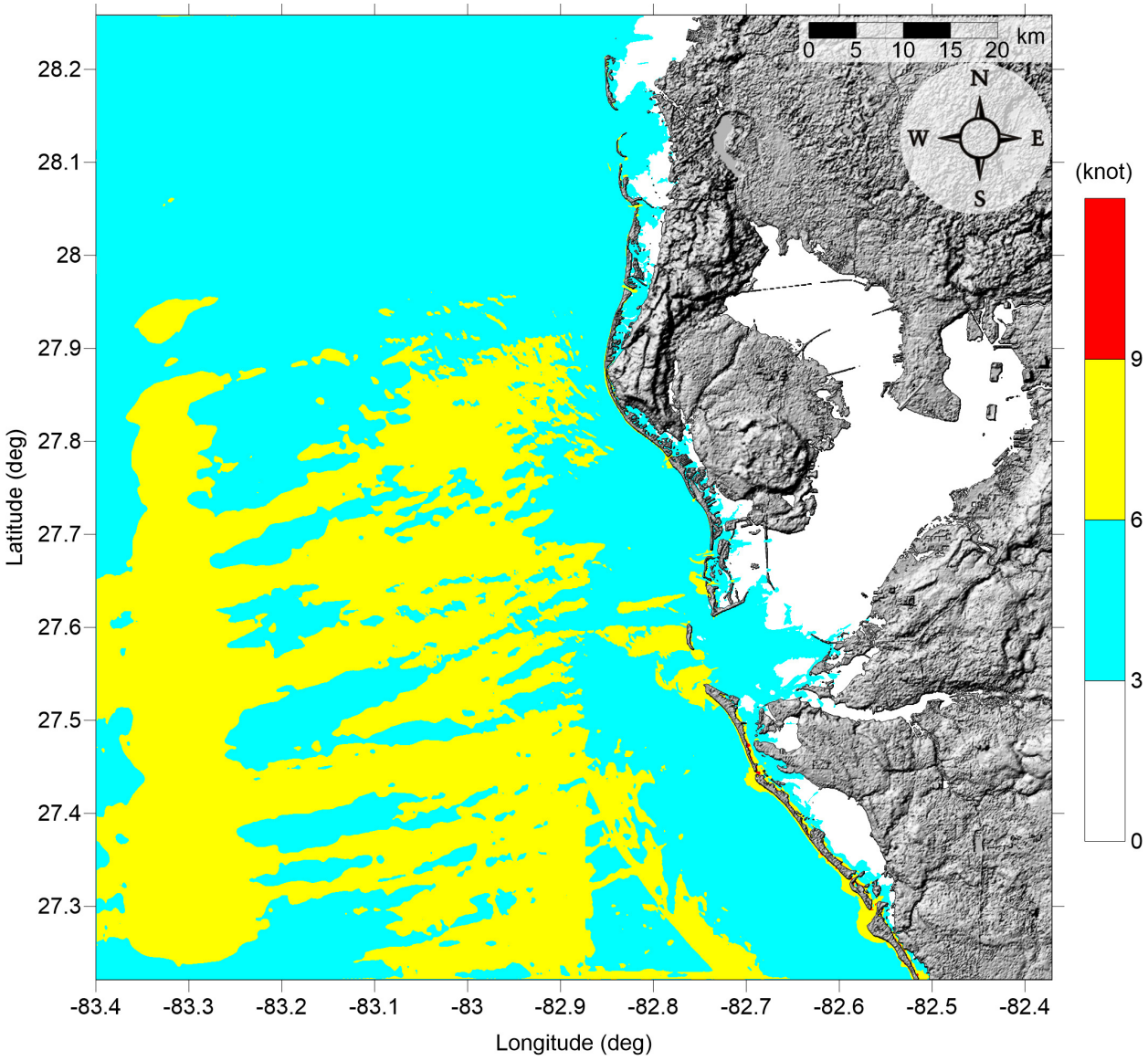

Figure 74: Maximum of maximum velocity magnitude contour in South Tampa Bay, FL (Grid 2 - 3 arcsecond) for all landslide scenarios.

South Tampa Bay, FL
All Sources
Maximum of Maximum Velocity Magnitude

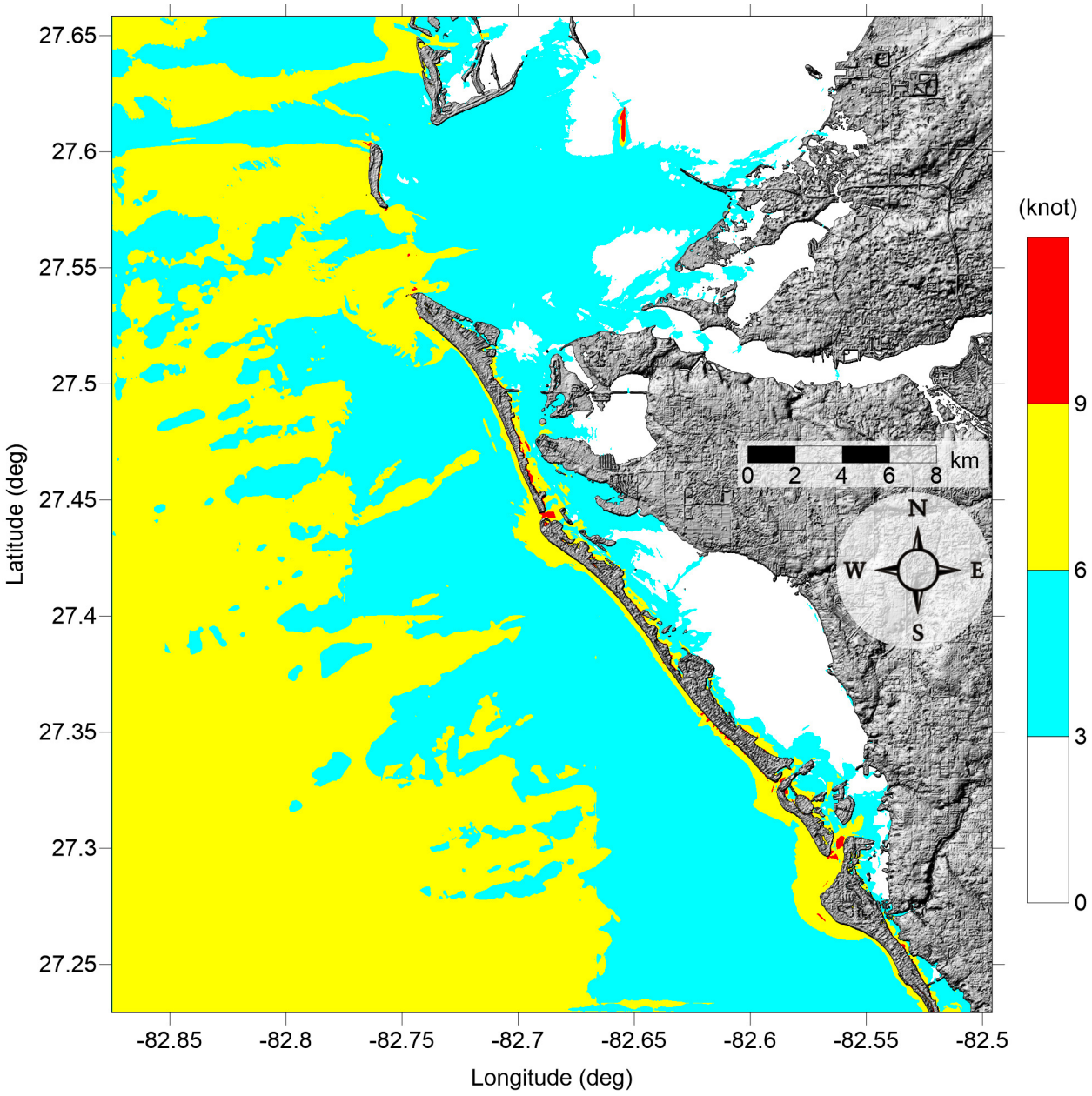

Figure 75: Maximum of maximum velocity magnitude contour in South Tampa Bay, FL (Grid 3 - 1 arcsecond) for all landslide scenarios.

South Tampa Bay, FL
All Sources
Maximum of Maximum Velocity Magnitude

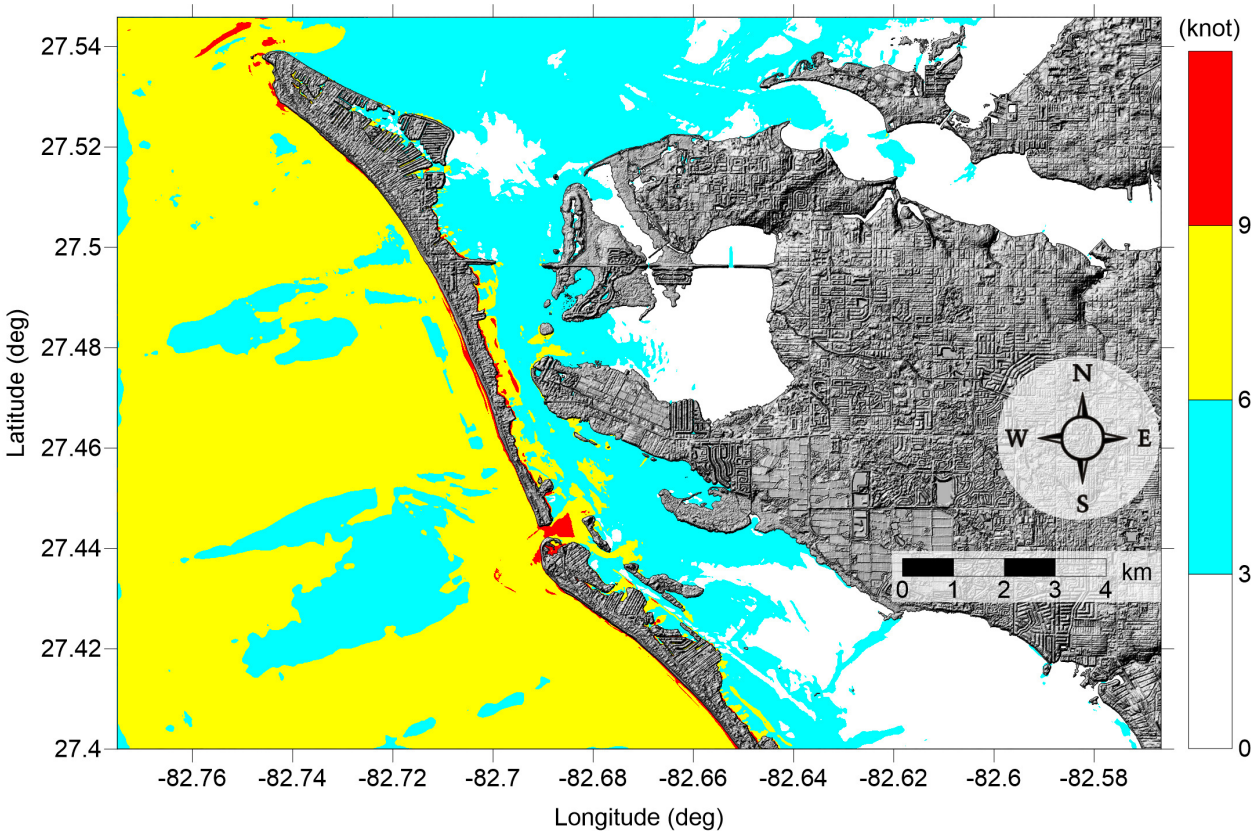

Figure 76: Maximum of maximum velocity magnitude contour in Anna Maria Island, FL (Grid 4 - 1/3 arcsecond) for all landslide scenarios.

South Tampa Bay, FL
All Sources
Maximum of Maximum Velocity Magnitude

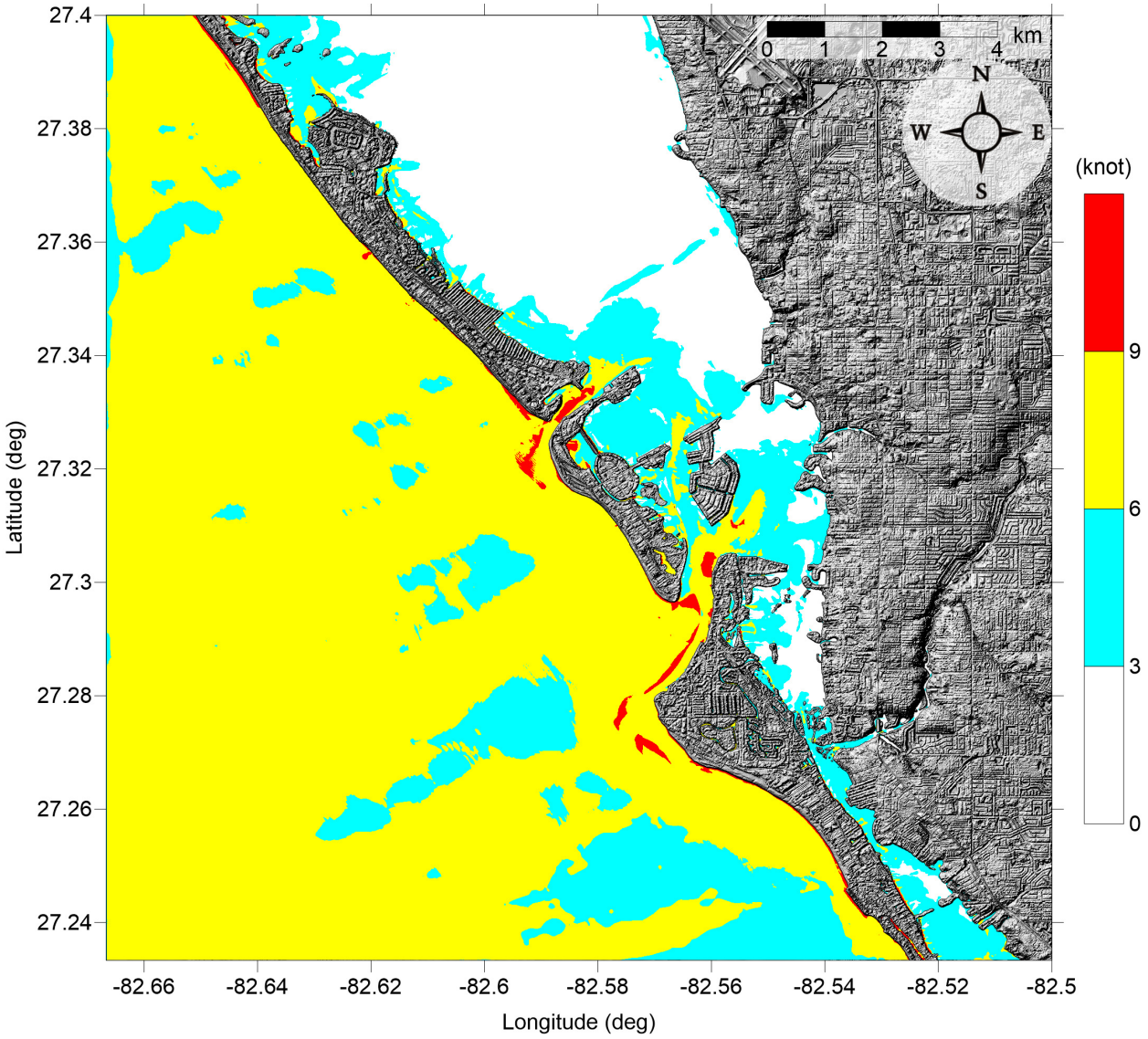

Figure 77: Maximum of maximum velocity magnitude contour in Siesta Key, FL (Grid 5 - 1/3 arcsecond) for all landslide scenarios.

South Tampa Bay, FL
All Sources
Maximum of Maximum Vorticity Magnitude

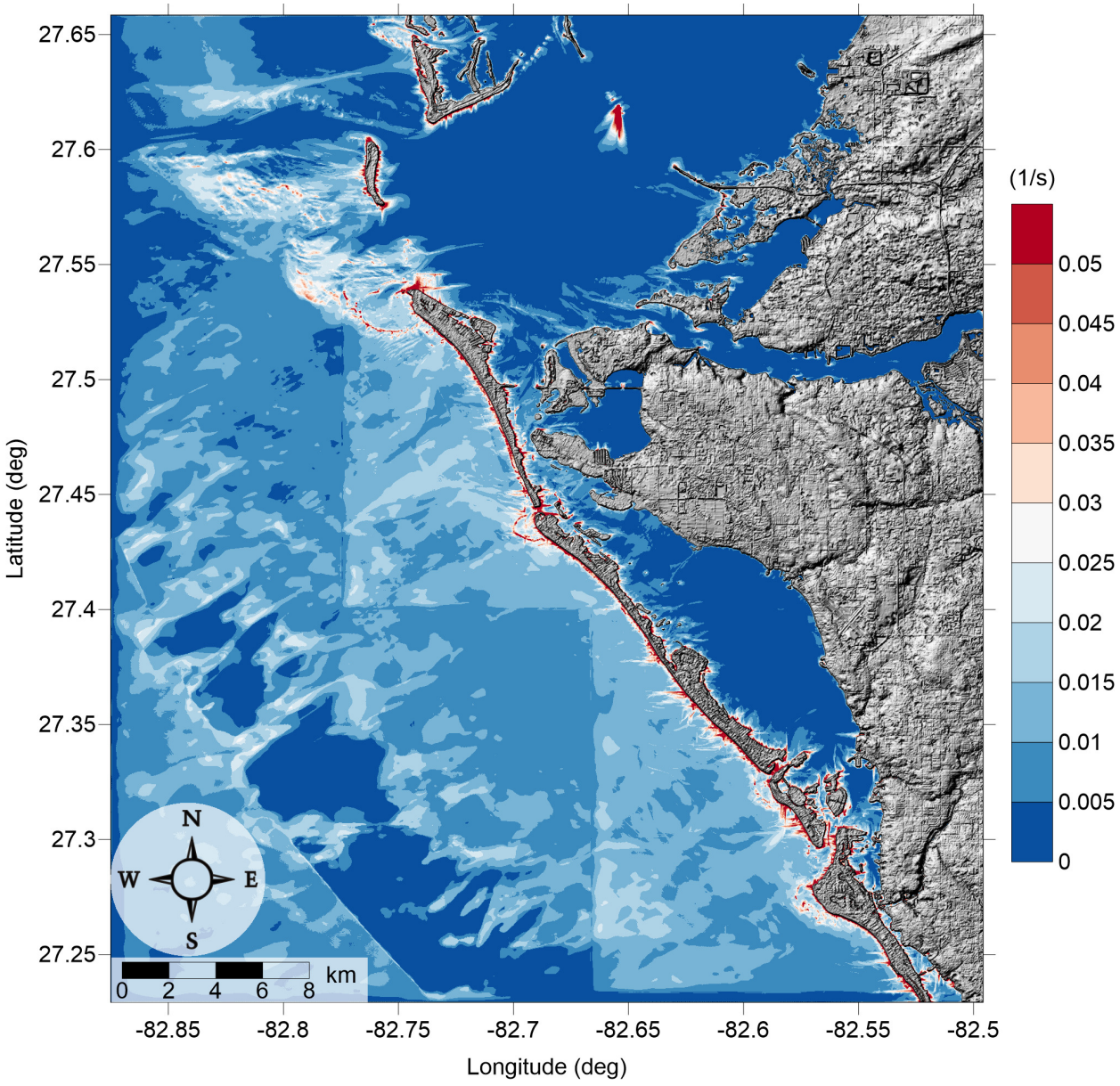

Figure 78: Maximum of maximum vorticity magnitude contour in South Tampa Bay, FL Grid 3 (1 arcsecond) for all landslide scenarios.

South Tampa Bay, FL
All Sources
Maximum of Maximum Vorticity Magnitude

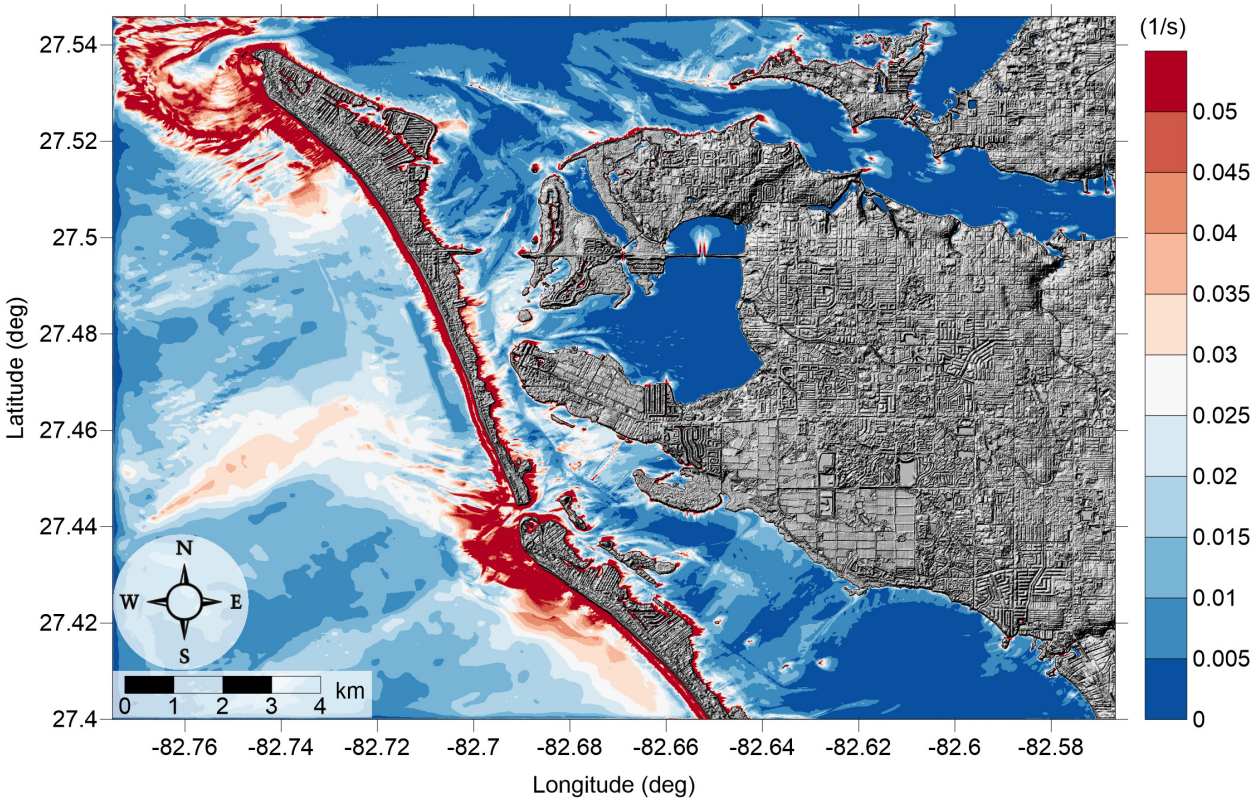

Figure 79: Maximum of maximum vorticity magnitude contour in Anna Maria Island, FL Grid 4 (1/3 arcsecond) for all landslide scenarios.

South Tampa Bay, FL
All Sources
Maximum of Maximum Vorticity Magnitude

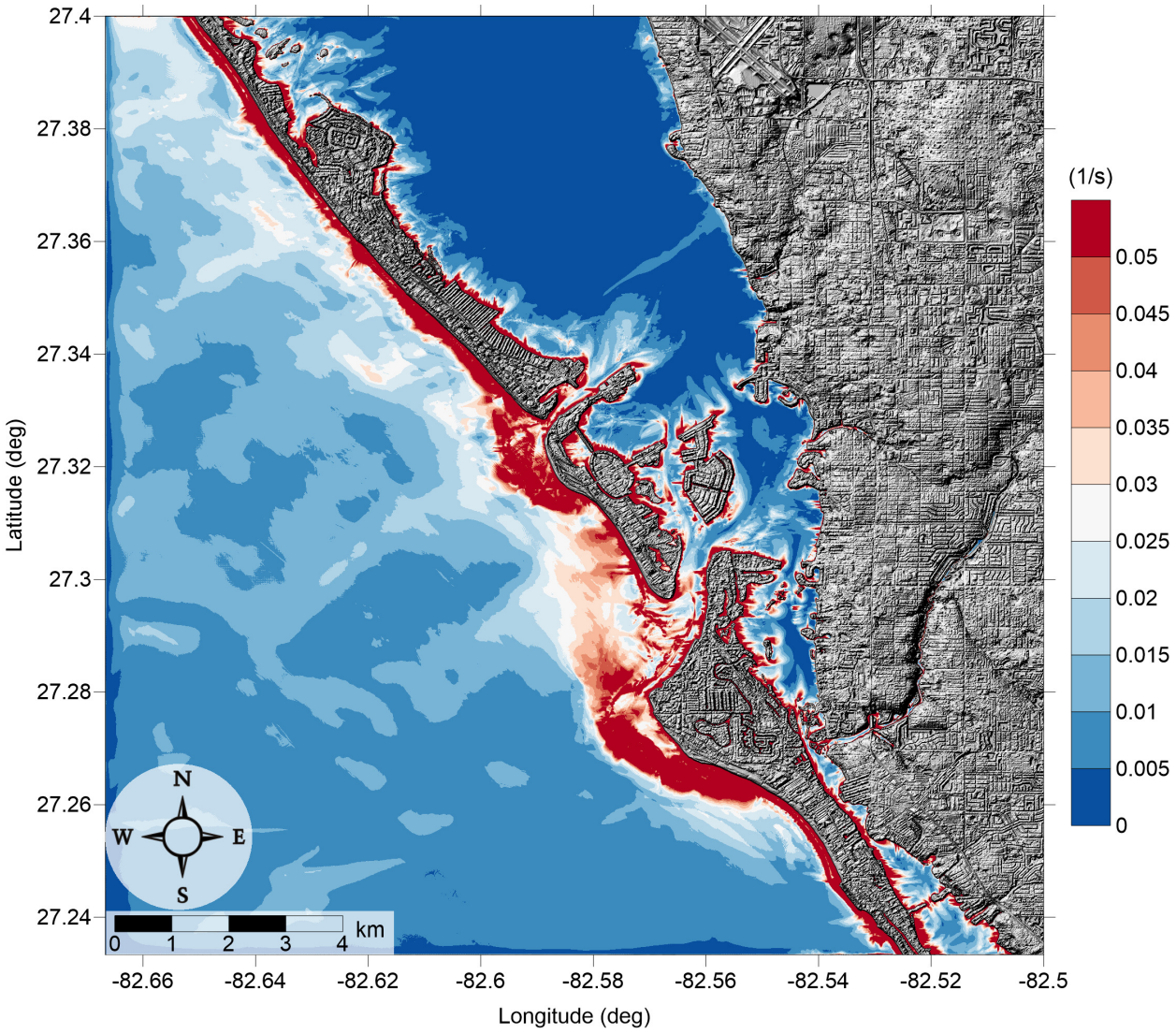

Figure 80: Maximum of maximum vorticity magnitude contour in Siesta Key, FL Grid 5 (1/3 arcsecond) for all landslide scenarios.

7 Meteosunami

Meteotsunami are atmospherically forced long waves typically associated with storms, squalls, frontal passages, etc. While being similar to earthquake tsunamis in terms of wave characteristics and nearshore wave transformations, meteotsunamis are unique in that they are usually generated by air disturbances having large pressure/wind gradient moving over the continental shelf where waves are amplified due to resonant mechanisms. Although relatively rare, meteotsunamis are capable of causing coastal infrastructure damage and eventually casualties. Analyses of recorded water level in the US show that meteotsunamis occur more frequently than expected, and therefore, it is important to include meteotsunami assessment in coastal hazard mitigation efforts. In this study, we conducted numerical experiments to investigate the generation and propagation of meteotsunami waves and assessed hazards on a broad scale in the northeastern Gulf of Mexico. The numerical experiments used a simple 2D depth-averaged hydrostatic shallow water model forced by an idealized atmospheric pressure disturbance on a set of trajectories and directions covering the whole Florida shelf. Results help identify pressure disturbance scenarios that most likely generate higher meteotsunami waves and vulnerable coastal regions.

7.1 Introduction

Meteotsunamis are long waves having meteorological origins such as atmospheric gravity waves, frontal passages, squalls, and storms, which typically exhibit large pressure and/or wind gradient [Monserrat et al., 2006]. Similar to ordinary tsunamis, i.e. those generated by earthquakes or landslides, etc., meteotsunamis have periods from a few minutes to 2-3 hours. Meteotsunamis cannot be distinguished from ordinary tsunamis in terms of coastal transformation and amplification within bays and harbors [Rabinovich and Monserrat, 1996], however, they differ in that meteotsunami wave generation requires resonant coupling between the atmospheric pressure disturbance and the shelf, otherwise sea level fluctuations would be on the order of a few centimeters solely due to the inverse barometric effects. The enhancement mechanisms have been thoroughly studied, including the Proudman resonance [Proudman, 1929], Greenspan resonance [Greenspan, 1956], and shelf resonance [Monserrat et al., 2006].

Proudman resonance occurs when the pressure disturbance forward speed matches the local shallow water wave celerity, ideally traveling over a long distance. In this regard, meteotsunamis are analogous to tsunamis generated by landslides, since the source (either atmospheric disturbances or landslides) moves in tandem with the wave, and the generation and propagation is not separated before it becomes free wave [Monserrat et al., 2006]. Energy transfer is most efficient when there is exact match between the speed of air disturbance and shallow water wave, and even a small deviation from this resonant speed would result in dramatic decrease in wave growth [Šepić et al., 2015]. Reflection and refraction within the continental shelf generates edge waves. When the atmospheric disturbance speed is close to one of the edge modes of the shore, wave can be amplified. This process is called the Greenspan resonance, and the resonant amplification is related to pressure disturbance amplitude and sea bed slope [Greenspan, 1956, Pattiaratchi and Wijeratne, 2015]. Shelf

resonance takes place if the meteotsunami wave period matches the oscillation mode of the shelf region. In addition to the resonant coupling between the air disturbance and shelf, the generated meteotsunami could be further enhanced by shoaling effects and local harbor resonance. Based on historical events, harbor resonance is required for a meteotsunami to become hazardous [Monserrat et al., 2006]. Harbor resonance occurs when the dominant period of the incoming waves matches that of the fundamental basin mode, resulting in positive superposition of the incoming and reflected waves [Orlić et al., 2010, Šepić et al., 2015].

Meteotsunami events have been reported to occur in oceans around the globe. Most prominent places include Mediterranean Sea, for example the Adriatic Sea and Balearic Sea; Nagasaki Bay, Japan and Longkou, China; in North America, the Great Lakes and the Atlantic coasts [Monserrat et al., 2006, Vilibić et al., 2014b, Pattiaratchi and Wijeratne, 2015]. Although meteotsunami cannot reach the level of destruction of seismic tsunamis [Pattiaratchi and Wijeratne, 2015], their damaging potential should not be ignored. On June 26, 1954, at least seven people were killed by meteotsunami near Chicago caused by a southeast moving squall line, and maximum Lake Michigan water level reached ∼10 ft/3 m [Ewing et al., 1954] with up to 50 m inundation inland at many beaches [Bechle and Wu, 2014]. In the east coast, a 4 m wave was witnessed at Boothbay, Maine on October 28 2008. The wave was generated by a cold front that damaged boats and structures [Vilibić et al., 2014a]. Churchill et al. [1995] documented a 3m wave in Daytona Beach, Florida caused by a squall line passing South Atlantic Bight at 15 m/s on July 3-4, 1992. The unexpected wave resulted in at least 75 injuries and some vehicular damage at the beach. Regarding the Gulf of Mexico (GOM), there is one well documented meteotsunami case that occurred on March 25, 1995, when eye witnesses at Tampa Bay, Florida reported a solitary wave up to 3 m high moving southeastward followed by a line of clouds 15 min later [Paxton and Sobien, 1998]. The wave ran up the beach to a height of 2-3 m after an initial withdraw of water. This wave is clearly generated by a large-amplitude atmospheric gravity wave which originated from a thunderstorm over east Texas and then headed southeastward over the Gulf of Mexico off the Florida Panhandle. The pressure perturbation travelled at a speed of approximately 25 m/s, allowing resonance of shallow water wave at around 60 m water depth over 250 km on the GOM eastern continental shelf.

In addition to these notable events, meteotsunami occurs much more frequently than expected. Bechle et al. [2016] analyzed 20 year records from 32 locations across the Great Lakes region, and identified meteotsunami events where the water level exceeded 0.3 m with period less than 2 h and the nearby weather station shows strong wind and/or pressure perturbations. Calculations of extreme meteotsunami occurrence show that there is an annual water level of 0.83 m and 10-year return water level of 1.3 m, which demonstrated that meteotsunamis as severe as the 1954 Chicago event occur more frequently than is normally thought. Along the U.S. east coast, a total of 548 meteotsunamis were recorded from 1996 to 2017 with wave height of 30 cases exceeding 0.6 m. These cases have strong seasonal occurrence patterns and often coincide with storms Dusek et al. [2019]. Olabarrieta et al. [2017] analyzed water level, atmospheric pressure, wind speed/direction and radar reflectivity data of three open water NOAA gauges (Panama City Beach #8729210, Clearwater Beach #8726724 and Naples #8725110) from 1996 to 2016, and discovered that there are around

20 meteotsunami events on average in the above three locations. This result should not come as a surprise as the GOM is a region where tropical cyclones and winter storms occur frequently. However, only 1 - 3 of the 20 events exceeds 0.5 m. In addition, Shi et al. [2020] showed that meteotsunamis are frequently triggered by Tropical Cyclone Rainbands via a study of Atlantic hurricanes landfalling in the GOM over a 20 year span.

Since these studies of past events all utilize NOAA tide gauges which are mostly not positioned in open oceans, they may not always capture a meteotsunami event (with the exception of Olabarrieta et al. [2017] where all three gauges are in open water). Moreover, these gauges may not have recorded the maximum wave Dusek et al. [2019] because of their sparsity. Numerical modeling is often employed to bridge the gap when there is not enough data, in order to gain a better understanding of the generation, propagation, and inundation processes during meteotsunami events, which can help recreate historical events, predict potential vulnerable locations, and ultimately contribute to hazard mitigation.

There has been a plethora of numerical meteotsunami studies within the Mediterranean Sea, for example: Vilibić et al. [2004] used a 2D nonlinear finite difference hydrodynamic model together with air pressure and wind speed/direction measurement data to recreate the east Adriatic strong sea level oscillations on June 27, 2003 related to gravity disturbance. In order to mitigate meteotsunami hazards, Šepić and Vilibić [2011] created a meteotsunami warning system by constructing a warning matrix based on previous events, theoretical estimations and numerical modelling. When rate of air pressure change exceeds a certain threshold at a station, disturbance speed and direction can be measured once it reaches other stations within the network, then all the parameters are feed into the location specific matrix to read the meteotsunami hazard level. To investigate the generation, amplification and propagation properties of meteotsunamis in the Balearic Sea, Ličer et al. [2017] applied nested ocean modelling system (ROMS) forced by synthetic atmospheric gravity waves, and quantify the contribution of Mallorca shelves and Menorca Channel to meteotsunami intensity, and analyzed subcritical and supercritical propagation conditions.

In the U.S., there is more modeling development in the Great Lakes since this region has relatively high meteotsunami occurrence. Anderson et al. [2015] showed the importance of wave reflection and focusing and edge wave formation in enclosed basin via numerical reconstruction of the May 27, 2012 Lake Erie event. Later, Linares et al. [2016] conducted numerical experiments with different disturbance speed and direction on northern Lake Michigan using a 3D Reynolds-averaged Navier-Stokes model, and found out that wind and pressure have similar contribution to meteotsunami hazard, and that a heuristic approach combining initial water surface amplitude, resonance function, wave transformation pathway, and location-specific scaling factor yield good approximation comparing to field and numerical results.

For the U.S east coast, the destructive 2008 Boothbay event sparked interests from the research community [Vilibić et al., 2014b]. Whitmore and Knight [2014] and Vilibić et al. [2014a] both simulated the Boothbay meteotsunami with their respective numerical models (WHICH MODELS)for the purpose of the development of a meteotsunami warning system. Similar effort on numerical development was carried out in the GOM, Shi et al. [2019] employed the COAWST modeling system and showed that tropical cyclone induced meteotsunami waves are more influenced by wind stress, and in contrast, during winter storms

atmospheric pressure fluctuations dominate wave generation, especially at depth deeper than 40 m.

To continue with the meteotsunami effort in the GOM, we aim to study the generation and propagation/amplification patterns of meteotsunami waves in eastern GOM and identify coastal communities vulnerable to meteotsunami inundation through a suite of idealized numerical experiments using parameters based on a real event. This section is organized as the following. Section 7.2 introduces our meteotsunami numerical scheme, grid setup, and gauges. Section 7.3 derives air pressure disturbance parameters from a historical meteotsunami event in the GOM using an idealized exponential decay function, and examines the generation and propagation of the resultant waves. Section 7.5 conducts a series of numerical experiments by shifting longitudinally the disturbance trajectory from Section 7.3 to cover the whole eastern GOM (No. of trajectories = 15) and including the full range of forward speed (10 m/s - 40 m/s, at 5 m/s intervals) that could potentially resonates with the continental shelf. Maximum anomaly tracking is used to explain the difference in propagation pattern and gauge results. Section 7.6 further extends the parameter space by changing incident direction of the disturbance, for a total number of $15 \times 7 \times 12 = 1260$ runs. This suite of maximum gauge water level results depicts the meteotsunami hazard distribution in the eastern GOM by incorporating favorable directions for each gauge location. Statistical analysis shows the directions and velocities that cause large meteotsunami impacts. Finally, a summary of the findings from the numerical experiments is in Section 7.7.

7.2 Numerical model description

The numerical model utilized in this study is a 2D hydrostatic model in spherical coordinates built on the nonlinear shallow water equations. The governing equations, staggered grid setup, and numerical solution scheme are outlined in Kowalik et al. [2005]. In order to simulate meteotsunamis driven by atmospheric pressure disturbances, the momentum equations are modified to include spatially-dependent surface air pressure in addition to the hydrostatic pressure. Wind stress and astronomical tide contributions are not included in the equations.

The governing equations for the depth-integrated, MT model , are derived from the incompressible Navier-Stokes equation and the incompressibility condition of the continuity equation in a spherical coordinates system in which λ is the longitude, ϕ is the latitude, and z denotes the normal distance from the still water level (SWL). The resulting momentum equations along λ and ϕ directions are:

$$\begin{aligned} \frac{\partial U}{\partial t} + \frac{U}{R\cos\phi}\frac{\partial U}{\partial \lambda} + \frac{V}{R}\frac{\partial U}{\partial \phi} - \left(2\Omega + \frac{U}{R\cos\phi}\right) V\sin\phi \;\; = \\ -\frac{g}{R\cos\phi}\frac{\partial \zeta}{\partial \lambda} - \frac{1}{\rho R\cos\phi}\frac{\partial p}{\partial \lambda} - n^2\frac{g}{D^{1/3}}\frac{U\sqrt{U^2+V^2}}{D} \end{aligned} \tag{2}$$

$$\frac{\partial V}{\partial t} + \frac{U}{R\cos\phi}\frac{\partial V}{\partial \lambda} + \frac{V}{R}\frac{\partial V}{\partial \phi} + \left(2\Omega + \frac{U}{R\cos\phi}\right) U\sin\phi \;\; = \\ -\frac{g}{R}\frac{\partial \zeta}{\partial \phi} - \frac{1}{\rho R}\frac{\partial p}{\partial \phi} - n^2\frac{g}{D^{1/3}}\frac{V\sqrt{U^2+V^2}}{D} \tag{3}$$

and the continuity equation reads

$$\frac{\partial \zeta}{\partial t} + \frac{1}{R\cos\phi}\frac{\partial (UD)}{\partial \lambda} + \frac{1}{R\cos\phi}\frac{\partial (VD\cos\phi)}{\partial \phi} = 0 \tag{4}$$

where U and V are depth-averaged velocity components in the λ and ϕ directions respectively. The variable t is the time, ζ is the free surface elevation from the SWL, R is the earth's radius, Ω is the earth's angular velocity, ρ is the water density, g is the gravitational acceleration and n is the Manning's coefficient for the sea-bottom friction ($0.025\ sm^{1/3}$). The total depth is defined as $D = \zeta + h_b$, where h_b is the water depth (from SWL to seafloor) and p is the atmospheric disturbance pressure.

To investigate meteotsunami effects on a global scale, and identify meteotsunami source areas affecting the northeastern area of the GOM, a model domain that encompasses the entire GOM (18.1 to 30.75 N, -97.9 to -80.2 W) is used. The bathymetry data was created with the NOAA Etopo1 dataset [Amante and Eakins, 2009] and referenced to the mean high water. Longitudinal and latitudinal grid spacing are both one arc-minute which achieves reasonable simulation time and resolves the meteotsunami wavelength well.A coastal wall is set at a water depth of 0.3 m to avoid runup on the wide cells on land. Outflow boundary conditions are applied to all the boundaries of the model domain. Through numerous model runs, we found that meteotsunamis affecting mostly the northeastern GOM originate from the same region, therefore, we decided to focus this study on the northeastern GOM to investigate regional meteotsunamis only. A model grid with higher resolution (15 arc-seconds) is created to reproduce the 2010 February Clearwater Beach meteotsunami event, where three NOAA gauges, Panama City (#8729108), Clearwater Beach (#8726724) and Naples (#8725110), Florida, are set up in the model to compare with field measurements. These gauges are chosen because they are placed in open water, i.e., they are not obstructed by coastal morphology such as barrier islands or structure, which would greatly influence the waves. In addition, 62 numerical gauges are set up at approximately 5 m deep open water locations along the coastline of northeastern GOM. All gauges record water level and air pressure every 20 seconds.

7.3 Air pressure definition

In February 2010, one of the most intense meteotsunami was recorded in Clearwater Beach, Florida. The $\sim$ 1 m wave height long wave was triggered by a dry season storm, which is common during winter in GOM where low pressure systems usually move eastward and squall lines develop ahead of cold fronts [Olabarrieta et al., 2017]. This squall line came off the Florida coast near Panama City and moved toward southeast along the isobath of the southwestern Florida shelf. A numerical representation of this event is shown in Fig. 81 a).

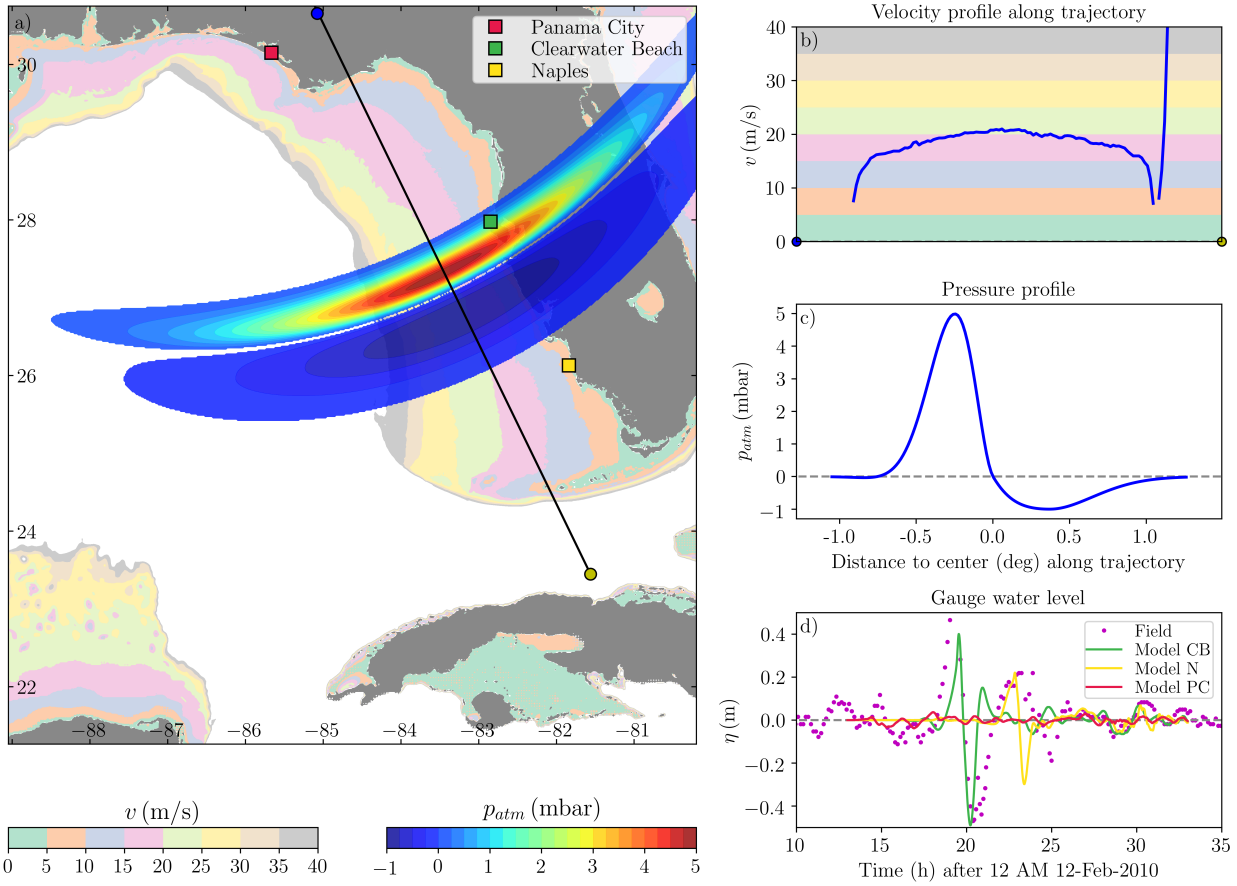

Figure 81: Model setup and Clearwater Beach gauge water level results for the Feb 12 2010 northern GOM meteotsunami. a) Meteotsunami atmospheric pressure contour plot and trajectory. Black solid straight line shows the trajectory on which pressure disturbance moves from the blue star toward the yellow. Pressure contour is plotted with a lower cut-off at 0.05 mbar for both crest and trough, underneath which lies the contour plot of the continental slope bathymetry expressed in terms of shallow water wave celerity $C = \sqrt{gh}$ from $0 \sim 40$ m/s, where h is depth of ocean floor. Three gauges in Panama City, Clearwater Beach, and Naples, Florida, are marked by red, green, and blue square, respectively. b) Velocity profile along the trajectory. In this case, it more or less follows the $20 \sim 25$ m/s contour line. c) Air pressure profile along the trajectory, where the leading trough amplitude is 1 mbar and the crest amplitude 5 mbar. d) Water level records at three numerical (solid lines) gauge and NOAA Clearwater Beach gauge (dots) starting at Feb 12 2010 10 AM UTC. Note that three numerical gauges' text are shortened to PC, CB and N and the line colors match those in a).

Based on radar reflectivity data from NOAA, (see Fig. 11 in reference Olabarrieta et al. [2017]), we constructed an idealized surface air pressure function where the amplitude of the crest A_c and trough A_t decay exponentially along both the length and width of the squall,

see Fig. 81 a) and Eq. 5.

$$P(x,y) = \begin{cases} A_c \cdot x \cdot exp(-(y)^2 - \left(\frac{x}{L_c}\right)^2), & x < 0 \\ A_t \cdot x \cdot exp(-(y)^2 - \left(\frac{x}{L_t}\right)^2), & x > 0 \end{cases} \tag{5}$$

where (x, y) are the longitude and latitude excursions along length L and L_c and L_t are the wavelength of the pressure crest and trough, respectively. The translation of the pressure disturbance is here simplified to a linear trajectory (single direction). Additionally, the pressure function is bent backwards (opposite of moving direction) to more realistically represent the geometry seen in the event, and is smoothed where crest and trough meet with quadratic stretching.

It is worth noting that a customized ramping function (Eq. 6) is applied to the beginning and ending the meteotsunami forcing to avoid an abrupt entry or exit of the pressure disturbance. We found that 8 minutes (480 seconds) of ramping time was enough to get a smooth transition. The inverse tangent function in Eq. 6 is employed because of its asymptotic nature toward $x \to \pm\infty$.

$$\begin{aligned} f_{ramp} &= \frac{1}{2}\left(1 + \frac{tan^{-1}(12\frac{t'}{480} - 6)}{tan^{-1}(6)}\right) \\ t' &= \begin{cases} t, & 0 < t < 480 \\ t_{end} - t, & t_{end} - 480 < t < t_{end} \end{cases} \end{aligned} \tag{6}$$

where t is in seconds, and t_{end} is the end time for air pressure presence.

7.4 Model results for the 2010 February Clearwater Beach meteotsunami

For this test case, the Etopo1 bathymetry is interpolated to a grid resolution of 15 arc-seconds to better resolve the generated waves.Fig. 81 presents the model setup and gauge results of the attempt to simulate the 2010 Feb storm-induced meteotsunami.

The pressure disturbance profile parameters are estimated by smoothing the Clearwater Beach meteorological data from Feb 12th 12 a.m. to Feb 14th 12 a.m. 2010, where crest amplitude A_c is 5 mbar and trough amplitude A_t is 1 mbar based on the average pressure; length of crest L_c is 0.7 deg; and length of trough L_t is 1.05 deg. Other parameters are estimated from radar reflectivity data (see Fig. 81 a): Arc length R is 5 deg with 8 deg radius, and start (blue dot) and end (yellow dot) coordinates of the pressure disturbance trajectory are (30.747, -85.107) and (23.448, -81.562). Pressure disturbance forward speed is estimated to be 20 m/s and it takes $\sim$ 13.5 hours to travel from start to end. The total run time is set to 20 hours to ensure that water level fluctuations at all the gauges have settle down.

The disturbance pressure and its trajectory is shown on Fig. 81 a). The continental slope bathymetry are also plotted, which is expressed in terms of shallow water wave celerity

$C = \sqrt{gh}$ from 0 m/s to 40 m/s, at 5 m/s intervals. The trajectory is placed along the 15 m/s - 25 m/s band and the velocity profile and the pressure profile along the trajectory are presented in Fig. 81 b) and c), respectively. The numerical gauge recordings at Clearwater Beach is denoted with (green line) in Fig. 81 d) alongside with NOAA de-tided water level data (dots), starting at 10 a.m. Feb. 12th, 2010. The numerical results at Panama City and Naples, Florida are shown with red and yellow lines. Our simulation resulted in a long wave with $\sim$ 0.9 m wave height at Clearwater Beach, similar to the actual event. However, the period does not match well. The mismatch in wave period can be attributed to several factors. First, the pressure wave lengths and amplitudes are based on data collected at the station, instead of at the "source". The concept of a source is different from ordinary tsunamis in that meteotsunami waves are constantly receiving energy from air pressure disturbance throughout resonant regions, as explained thoroughly by Monserrat et al. [2006]. Second, radar reflectivity mosaic demonstrates great variability in squall line shape for the few hours leading up to the first wave. It is possible that the pressure wave length was much greater than was recorded at Clearwater Beach. Moreover, the squall line can be seen changing directions. Lastly, this simulation is designed to show that the model is capable of producing meteotsunami waves from the simplified pressure disturbance, and it was not intended to recreate the exact water level response. For a better recreation of this event, it requires a comprehensive model system that couples atmospheric, ocean, wave models, with high resolution bathymetry data.

The formation and propagation of meteotsunami waves are demonstrated with sea level snapshots at 1.5 hour intervals in Fig. 82. As soon as the pressure disturbance enters the GOM region, ocean surface starts to deform due to the inverse barometric effects off the Panama City coast (Fig. 82 a). Since the disturbance is moving at a constant velocity of 20 m/s, wave continuously builds up near the 40 m isobath with matching shallow water celerity (Proudman resonance). Up until 6.0 h, the meteotsunami wave is headed toward the southeast, following the orientation of the coastline near Panama City (Fig. 82 b, c, d). During this period, it is noticeable that the wave is turning counterclockwise because of refraction. After Clearwater Beach is hit by the first meteotsunami wave crest at 6.0 h, the meteotsunami travels as an edge wave [Greenspan, 1956] between Clearwater Beach and Naples. It is worth noting again that resonance occurs throughout the whole time of active pressure disturbance, therefore, the meteotsunami wave is still gaining/maintaining momentum near the trajectory before eventually hit the Florida Keys (Fig. 82 h). The last panel (Fig. 82 l) shows the maximum positive anomaly, where it can be observed that Clearwater Beach and Key West are the two hardest hit areas.

7.5 Meteotsunami propagation pattern and maximum coastal water level distribution

Meteotsunami wave propagation shown in Fig. 82 revealed that Clearwater Beach and Florida Keys are the focus of impact under this particular pressure disturbance and trajectory scenario. One explanation for this is that these two locations are at the end of extended straight isobaths along which Proudman resonance occurs consistently and thus

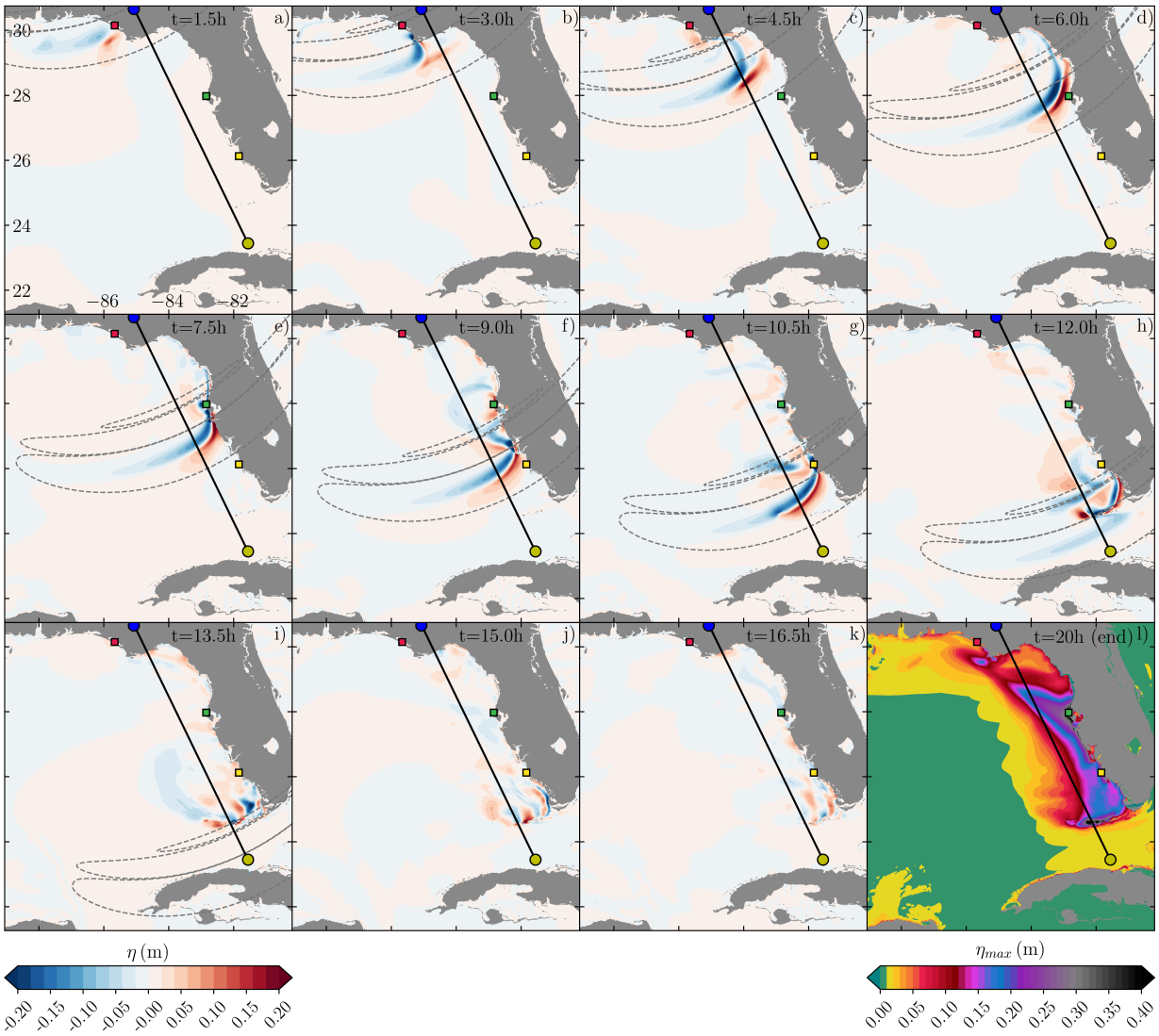

Figure 82: a) - k) Water level anomaly field snapshots for the Feb 12 2010 northern GOM meteotsunami from 1.5 h to 16.5 h at 1.5 h intervals. Dashed outline marks the extents of the pressure disturbance. l) Maximum water level anomaly at 20 h. Three gauges in Panama City, Clearwater Beach, and Naples, Florida, are marked by red, green, and blue square, respectively.

meteotsunami wave could gain enough momentum/height. In order to further investigate how the coastline is affected by meteotsunami wave under different scenarios, we designed a suite of numerical experiments where we vary the trajectory location and forward speed.

The parameter space used in this experiment is shown in Fig. 83 a). 15 trajectories are laid out parallel with and centered around the one used in Section 7.3, with the westernmost and easternmost 1.5 deg apart. Seven velocities, from 10 m/s to 40 m/s at 5 m/s intervals, are employed to drive the same pressure disturbance. Therefore there are a total of 105 cases. As a result, the disturbances take different time to reach the end (arrow), hence each

run is set to finish at 30 hours to allow enough time even for the slowest case. Also on display in Fig. 83 a) are 62 numerical gauges that are distributed along the northeastern GOM coastline.

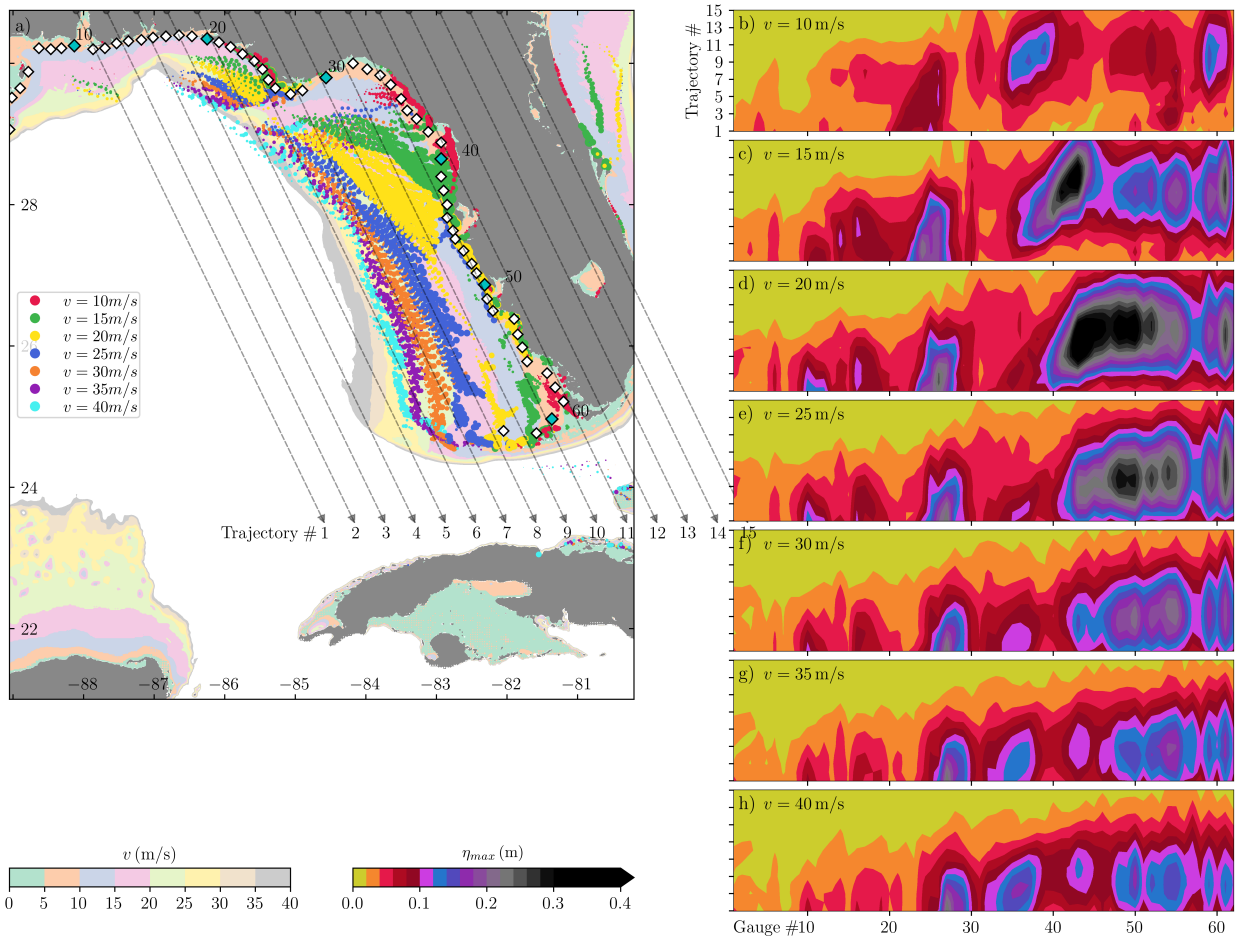

Figure 83: Florida GOM coastal gauge maximum water level distribution versus pressure disturbance trajectory location and forward speed. a) Map view of trajectory locations (dashed line and arrow for direction of travel) and contour plot of the continental slope bathymetry expressed in terms of shallow water wave celerity $C = \sqrt{gh}$ from 0 $\sim$ 40 m/s, where h is depth of ocean floor. Colored dots represent maximum anomaly tracking at $\sim$ 7 m intervals for all runs. b) through h) show, for each forward speed from 10 m/s to 40 m/s, maximum water level versus gauge location and trajectory location.

Maximum anomaly tracking of sea level can offer insight into the interaction between atmospheric forcing and bathymetry, especially for large number of cases. Scattered dots in in Fig. 83 a) represents maximum anomaly tracking at $\sim$ 7 min intervals for all cases, with color representing different velocities and size of dots indicating magnitude. Anomaly with amplitude less than 5 cm is not shown here. The maximum anomaly tracking color zones follow the order of velocities (or depth) where slower velocities appear closer to the coast and vice versa. 15 m/s and 20 m/s zones take up a large portion because the 10 m/s to 25

m/s shallow water celerity range account for the majority of the continental shelf (see Fig. 81 a). This resemblance should be expected, since the primary mechanism of meteotsunami wave generation is the Proudman resonance. In general, the maximum anomaly zones do not overlap with the zones of shallow water celerity everywhere: initially the maximum anomaly is generated within its corresponding velocity zones, but eventually they decouple from the isobath (shallow water celerity). This result indicates that bathymetry pattern has control over the direction of major meteotsunami waves. Trajectories are not differentiated within the colored dots because it has less influence than velocity, although it can be readily deduced that, e.g., western trajectories (#1, #2, #3, ...) result in maximum anomaly tracking to the west within the same tracking color zones. Nonetheless, the orientation of the trajectories can play an important role in meteotsunami wave propagation, which will be explained with more experiments in the next section.

The aforementioned propagation pattern is directly associated with the distribution of impact at coastal communities shown with maximum water level from all 62 numerical gauges in Fig. 83 b) through h). Inside each pane, the horizontal axis is the gauge #1 - #62 and vertical axis is the trajectory #1 - #15. The most pronounced feature is that velocities 15 m/s - 25 m/s generate the highest water level (¿ 0.4 m) near gauge #40 - #50 (from Hernando to Charlotte County, Florida). Other hotspots include gauge #26 and #27 (St. Joseph Peninsula in Gulf County, Florida) due to the protruding coastal morphology, and gauge #61 (Key West, Florida) due to its position at the edge of the shelf facing direct propagation of meteotsunami waves and their reflection off the Florida coasts. As for trajectory location, it is obvious that the middle ones (e.g. Fig. 83 d), near the trajectory used in Section 7.3) result in higher water levels because of more intense resonance with the shelf. In addition, as pressure disturbance velocities increases, i.e., from Fig. 83 b) to h), the highest impact coastlines shift toward southern Florida.

Proudman length is a more quantitative approach to examine the trajectory and velocity combination [Ličer et al., 2017] that is hazard-prone for a region, which is calculated as the percentage of the trajectory where the bathymetry shallow water celerity falls within 5% of the forward speed of the disturbance. Fig. 84 shows the Proudman length result form the same scenarios of Fig. 83, which corroborates previous findings, i.e., trajectories on the continental shelf that has forward speed between 15 m/s and 25 m/s more efficiently generate meteotsunami due to greater Proudman length.

7.6 Northeastern GOM meteotsunami risk assessment

Maximum anomaly tracking has proven to be valuable in linking the forward speed and trajectory with coastal impact. However, so far we have only experimented with cases where the trajectories are more or less parallel to the continental slope. In order to study the influence of different incident directions and assess meteotsunami hazard under all possible scenarios, the parameter space is further expanded to cover the entire northeastern GOM with 12 incident directions that are illustrated in Fig. 85 a). The 12 directions are 0°, 30°, 60°, ..., and 330°, where 0° means the pressure originates from south and 90° means from west, etc., in a clockwise order. Under each incident direction scenario the same 15 trajectories and 7 velocities as Section 7.5 are used, thus there are a total of 1260 ($12 \times 15 \times 7$)

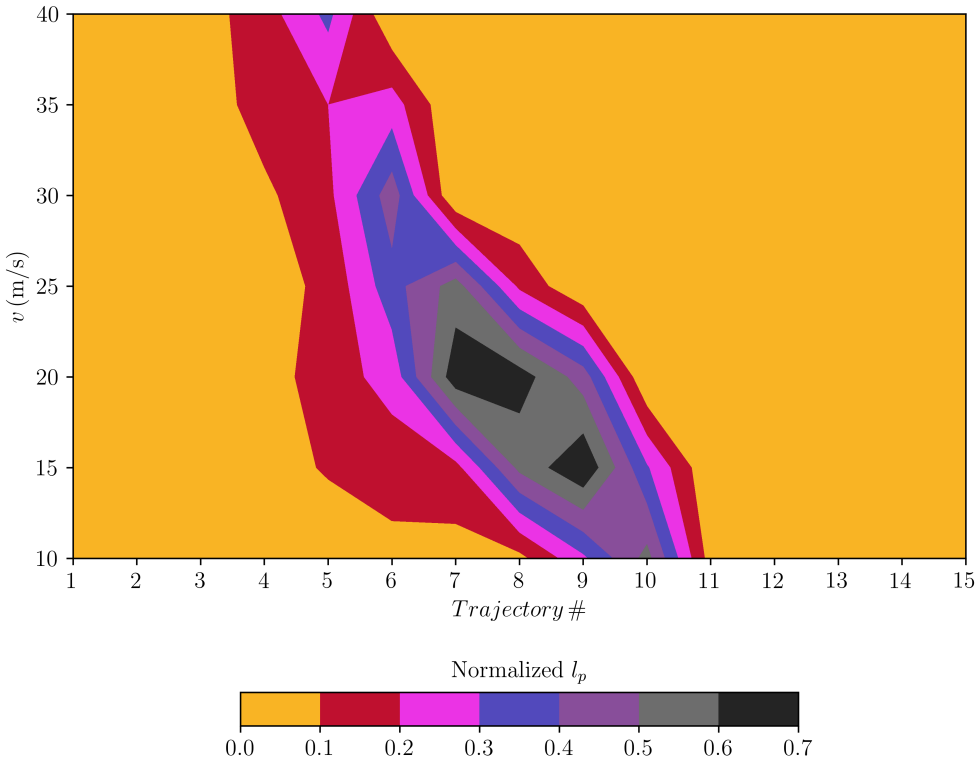

Figure 84: Normalized Proudman length versus atmospheric disturbance trajectory and forward speed.

cases, with the only difference being that the trajectories are elongated when necessary to cover the full region under all incident directions.

Starting at gauge #8, data of all 1260 cases at every 5th gauge is compiled into a rose diagram, which plots the maximum water level of the 105 (15×7) cases under each incident direction. Take gauge #13 for instance, there is less than 0.15 m wave resulting from pressure disturbance coming from north, whereas it can reach over 0.4 m from the east and the rest lie in the middle at around 0.3 m. Similarly for gauge #58, since it is situated at the southeast corner of the shelf, there is no room for meteotsunami wave to develop from pressure disturbance coming from south or east (the second quadrant). The coastal region from Hernando to Charlotte County, FL, i.e. from gauge #43 to #53, seem to suffer from high meteotsunami waves from all directions except from the land. This high risk zone should not come as a surprise because of the protruding morphology of its coastline, and as explained in Section 7.5, because of long straight continental shelf isobath starting from the Florida panhandle (around gauge #8 to # 28) favorable for wave resonance. Furthermore, this zone also faces higher waves (> 0.3 m) propagating perpendicularly to the coastline, comparing to the Florida panhandle area (< 0.3 m), likely due to the wider continental shelf allowing more air-water energy transfer. In contrast, the coastal area around Taylor, Dixie and Levy counties, FL, i.e., around gauge #33 to #38, having concave coastlines, is generally shielded from meteotsunamis, expecting less than 0.3 m waves.

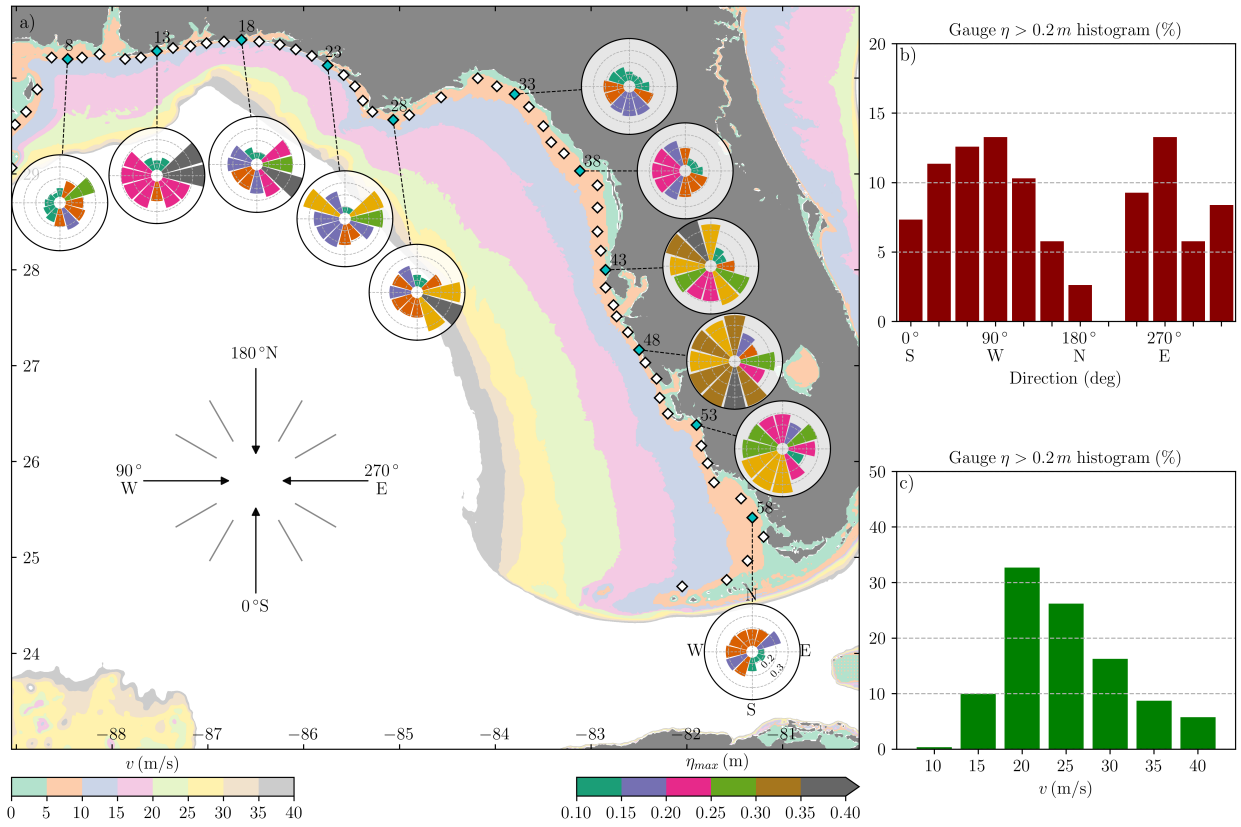

Figure 85: a) Rose diagram of select Florida gauges each showing the maximum water level (η_{max}) recorded for each direction from a parameter study of 1260 cases (12 incident directions, each with 15 trajectories and 7 pressure disturbance forward speeds). Rose diagram radial scale (η_{max} from 0.1 m to 0.4 m) and directions (NWSE) is marked in gauge #58, which are the same for all the gauges. Contour plot of the continental slope bathymetry is expressed in terms of shallow water wave celerity $C = \sqrt{gh}$ from $0 \sim 40$ m/s, where h is depth of ocean floor. Incident direction is illustrated with arrows where 0° means the pressure disturbance originates from south and 90° means from west, etc., in a clockwise order. b) Incident direction distribution of cases whose recorded water level exceeds 0.2 m (each gauge count separately). c) Pressure disturbance forward speed distribution of cases whose recorded water level exceeds 0.2 m (each gauge count separately).

The maximum water level data from all cases (each gauge counts separately) is further compiled into histograms in search for directions and velocities with higher meteotsunami risk in the eastern GOM. Fig. 85 b) shows the distribution in incident direction where gauge water level exceeds 0.2 m and it indicates that the most favorable direction for higher water level are 0° - 90° (south to west, 3rd quadrant), and also around 270° (east), with each direction bin accounting for more than 10%. According to the rose diagrams in Fig. 85 a), pressure disturbances coming from the south to west (0° - 90°) direction result in higher water level near south Florida region, while the east (270°) direction to the panhandle region. Similarly, Fig. 85 c) shows the distribution in forward speed where gauge water level

exceeds 0.2 m. The result shows that 20 m/s and 25 m/s are the forward speeds with the most potential, together accounting for more than 50% of the cases. 30 m/s is more than 15%, the third most common speed for higher water level.

7.7 Summary

We conducted numerical experiments to investigate the generation and propagation of meteotsunami and assessed its hazard on a broad scale in the northeastern Gulf of Mexico (GOM). The experiments used a simple 2D depth-averaged hydrostatic shallow water model supplemented by an idealized air pressure disturbance derived from the Florida meteotsunami event in Feb 2010. By varying incident direction, prescribed pressure disturbance trajectory location and pressure disturbance forward speed, 1260 runs were performed. Results show that forward speed has more influence on maximum water level than the trajectory location. Statistics indicates that the most favorable direction for higher water level are 0° - 90° (south to west, 3rd quadrant), and also around 270° (east), with each direction bin accounting for more than 10%, where gauge water level exceeds 0.2 m. Pressure disturbances coming from the south to west (0° - 90°) direction result in higher water level near south Florida region, while the east (270°) direction to the panhandle region. Similarly, the forward speed distribution result shows that 20 m/s and 25 m/s are the forward speeds with the most potential, together accounting for more than 50% of the cases. 30 m/s is more than 15%, the third most common speed for higher water level. Results help identify the most vulnerable coastal communities and the most common air pressure disturbance scenarios that produce higher water level. Maximum water level anomaly tracking and Proudman length analysis both demonstrate that Florida's long straight continental slope in the eastern GOM is favorable of producing higher meteotsunami provided that there is stable air pressure disturbance moving with resonant velocities. Overall, the numerical study could aid in predicting meteotsunami trajectory, identifying vulnerable coastal communities, estimating water levels, and hopefully helping to mitigate meteotsunami hazard.

8 Conclusions

This project focused on the implementation of recent developments in the tsunami science recommended by the National Tsunami Hazard Mitigation Program - Modeling Mapping Subcommittee - Strategic Plan (NTHMP-MMS-SP) into our current Gulf of Mexico (GOM) tsunami mitigation products. Four main developments for tsunami mitigation have been created under this project for two new communities in the GOM (Jamaica Beach, TX and South Tampa Bay, FL) that will provide guidance to state emergency managers for tsunami hazard mitigation and warning purposes. The first task is the development of tsunami inundation maps for the two selected communities with nine landslide sources. The second is the comparison between existing SLOSH hurricane flooding data and our tsunami inundation result for the two new communities in order to facilitate temporal-low-order estimate for tsunami hazard areas (community) where inundation studies have not yet been assigned/executed or where little bathymetric and elevation data exists. The third is to produce maritime products (maximum of maximum (MOM) velocity and velocity magnitude maritime maps) for both communities to help identify impact specifically on ship channels, bay inlets, harbors, marinas, and other infrastructures. The fourth task is a continuation of the study to obtain an understanding of meteotsunami through the characterization of physical parameters in a specific region susceptible to meteotsunami in the GOM. The generation and propagation/amplification patterns of meteotsunami waves in eastern GOM are studied using maximum water level anomaly tracking, and coastal communities vulnerable to meteotsunami inundation are identified through a suite of idealized numerical experiments covering the entire eastern GOM, with parameters from different pressure disturbance incident directions, forward speeds and trajectory locations.

Tsunami wave propagation and inundation in Jamaica Beach, TX and South Tampa Bay, FL was also modeled to obtain maximum inundation and extent, momentum flux, current velocity and vorticity maps considering the entire suite of nine landslide sources. In Jamaica Beach mapping area, MOM tsunami inundates most of the island facing the GOM. Overall water depth exhibits decreasing trend from oceanfront toward the bay, with maximum over 2 m. North half of City of Jamaica Beach and the communities around Lake Como and Eckert Bayou which are north of Steward Rd do not suffer from any inundation, though major evacuation route, San Luis Pass Rd is severely flooded. Since this area is far from both San Luis Pass and Galveston Bay entrance, tsunami energy has been significantly dissipated when waves reach the bay side of the island (lee side), therefore the West Bay, all three Deer Islands, Tiki Island and Flamingo Isles are well protected. In South Tampa Bay mapping area (Anna Maria Island, Longboat Key, Lido Key and Siesta Key), overall the barrier islands provide ample protection for the mainland against tsunami inundation. While inundation depth at the barrier island ranges from 1 to over 3 m from the lee side to the GOM, the mainland is mostly less than 2 m. Cortez, FL is relatively more flooded than other mainland cities due to its proximity to Longboat Pass, where the communities around Cortez Rd west of 119 St W see inundation as high as 2 m. Another high risk mainland area are the communities south of the Phillippi Creek, where inundation depth is mainly below 2 m but can reach to as high as 3 m. For both communities, MOM tsunami inundation is produced solely by the Mississippi Canyon failure. This geological failure is the largest in

both, area and volume of material removed, and therefore produces the highest amplitude wave of all simulated sources.

While high-resolution tsunami inundation studies have been completed for these 16 communities and are planned for additional locations, vulnerability assessments are still essential for coastal locations where inundation studies have not yet been performed or planned, or where there is a lack of high-resolution bathymetric and/or elevation data. Therefore, we aim to extend the results of the completed mapping studies in order to provide estimates of tsunami inundation zones for hazard mitigation efforts in unmapped locations. We anticipate that communities which lack detailed tsunami inundation maps, but which have modeled hurricane storm surge information, would be able to use the results presented here to estimate their potential tsunami hazard level based on their regional topographical/bathymetric features. We stress, however, that such results should be used only in a broad, regional sense given the differences seen among and within communities based on local details of bathymetry, topography, and geographical location within the GOM basin. There is no guarantee that comparison results will be identical in areas with similar topography, and comparisons should only be made after understanding the limitations and simplifications of the methodology presented here. Comparisons of MOM tsunami inundation results with the SLOSH MOM high tide storm surge inundation indicate that while the details of referencing tsunami inundation to hurricane storm surge is dependent on local topographic effects, general regional trends can be identified. In Jamaica Beach mapping area, the hurricane category that best matches tsunami inundation closely follows the MOM tsunami inundation trend, where Category 3 appears near the beach, Category 2 runs parallel and takes up the middle section of the island, and the rest is occupied by Category 1. The difference between hurricane flooding and tsunami inundation is mostly within ± 1 m. In South Tampa Bay mapping area (Anna Maria Island, Longboat Key, Lido Key and Siesta Key), the matching hurricane category distribution also closely reflects that of tsunami inundation. Category 3 is only seen on a thin strip near the barrier island beach, and the majority of the barrier islands are split between Category 2 and 1. Mainland coastal communities that are inundated have water depth mostly equivalent to Category 1, except for south of Phillippi Creek where Category 2 inundation is observed. The difference between hurricane flooding and tsunami inundation $\Delta\zeta$ is generally within $\pm$ 0.5 m for the barrier islands, however, at the mainland the difference reaches larger than 1 m, which means storm surge inundation depth is higher since tsunami waves generally cannot reach as far into the bays.

We produced the MOM velocity and vorticity magnitude maps for all the landslide scenarios, for Jamaica Beach, TX and South Tampa Bay, FL, based on a simplified current velocity damage scale where we associate 0 - 3 knots to unharmful currents, 3 - 6 knots to minor damage, 6 - 9 knots to moderate damage, and over 9 knots to major damage. The four damage levels are denoted with white, blue, yellow and red colors, respectively.

From the MOM velocity magnitude results in the entire Gulf of Mexico (Fig. 68), it can be observed that, potential damaging currents ($>$ 3 knots, blue, yellow and red areas) tend to be present in most of the area shallower than the minimum offshore safe depth (approximately 200 m or 100 fathoms). However, damaging currents could reach areas deeper than 200 m close to most of the landslide generation regions. Major damaging currents ($>$ 9 knots, red) can be expected in most of the landslide generation regions, in the continental shelf adjacent

to Mississippi Canyon, offshore northwest Florida, and Yucatán shelf. Moderate (> 6 knots and < 9 knots, yellow) damaging current areas are scattered over the continental shelf, but mostly close to areas with major damage currents. General trends can be observed from the different grid levels of the MOM velocity for Jamaica Beach, TX. Most of offshore region is expected to have minor damaging currents, with moderate damaging currents occurring along the coastline and jetties. For the Jamaica Beach area, moderate damaging currents (> 6 knots) can be expected adjacent to the Galveston island GOM coastline. There is no damaging currents inside the Galveston Bay, however, there is some minor damaging current in the bay entrance and the Galveston Ship Channel. In South Tampa Bay, FL, the situation is different from Jamaica Beach, TX. Moderate damaging currents (> 6 knots) can be seen more than 100 km offshore. Major damaging current (> 9 knots) area appears as a thin strip near the barrier islands and at bay entrances, e.g., Tampa Bay a. In the interior bays and channels, the tsunami currents are less severe which can be used as shelter to minimize tsunami impact. Vorticity distribution, on the other hand, displays similar patterns between the two locations, where high vorticity appears around the barrier island, and are more intense near the bay entrances.

Tsunami hazard maritime products such as tsunami current magnitude, vorticity, safe/hazard zones would be central for future developments of maritime hazard maps, maritime emergency response and as well as infrastructure planning.

In the meteotsunami pilot research from Horrillo et al. [2019], a shallow water model with the addition of a pressure term has shown to be capable of modeling meteotsunami generation. In this continuing meteotsunami study, we conducted numerical experiments to investigate the generation and propagation of meteotsunami and assessed its hazard on a broad scale in the northeastern Gulf of Mexico (GOM). The experiments used a simple 2D depth-averaged hydrostatic shallow water model supplemented by an idealized air pressure disturbance derived from the Florida meteotsunami event in Feb 2010. By varying incident direction, prescribed pressure disturbance trajectory location and pressure disturbance forward speed, 1260 runs were performed. Results show that forward speed has more influence on maximum water level than the trajectory location. Statistics indicates that the most favorable direction for higher water level are 0° - 90° (south to west, 3rd quadrant), and also around 270° (east), with each direction bin accounting for more than 10%, where gauge water level exceeds 0.2 m. Pressure disturbances coming from the south to west (0° - 90°) direction result in higher water level near south Florida region, while the east (270°) direction to the panhandle region. Similarly, the forward speed distribution result shows that 20 m/s and 25 m/s are the forward speeds with the most potential, together accounting for more than 50% of the cases. 30 m/s is more than 15%, the third most common speed for higher water level. Results help identify the most vulnerable coastal communities and the most common air pressure disturbance scenarios that produce higher water level. Maximum water level anomaly tracking and Proudman length analysis both demonstrate that Florida's long straight continental slope in the eastern GOM is favorable of producing higher meteotsunami provided that there is stable air pressure disturbance moving with resonant velocities. Overall, the meteotsunami numerical study could aid in predicting meteotsunami trajectory, identifying vulnerable coastal communities, estimating water levels, and hopefully helping to mitigate meteotsunami hazard.

Although the recurrence of destructive tsunami events have been verified to be quite low in the GOM, our work has confirmed that submarine landslide events with similar characteristics to those used here, have indeed the potential to cause severe damage to GOM coastal communities. GOM is a region where tropical cyclones and winter storms occur frequently. From 1996 to 2016, there are around 20 meteotsunami events on average in Florida. Our results indicate meteotsunami water level could reach as high as 0.5 m in some locations and has the potential to cause damage. Therefore, this work is intended to provide guidance to local emergency managers to help managing urban growth, evacuation planning, and public education with the final objective to mitigate potential landslide tsunami and meteotsunami hazards in the GOM.

Acknowledgments

This work was supported by the National Tsunami Hazard Mitigation Program (NTHMP) under awards NA19NWS4670015, "Development of two tsunami inundation maps and continuation of the meteotsunami characterization for the GOM". The authors wish to thank all NTHMP modeling and Mapping Subcommittee members and GOM's emergency manager representatives for their helpful insights. Special thanks go to Brad Baker for their helpful insight and support. Also thank Kelly Carignan and Kelly Stroker for providing the DEMs. High resolution inundation maps are available from `http://www.tamug.edu/tsunami/NTHMP/NTHMP.html` or by contacting corresponding author upon request.

References

C. Amante and B. Eakins. ETOPO1 1 Arc-Minute Global Relief Model: Procedures, Data Sources and Analysis. *NOAA Technical Memorandum NESDIS NGDC-24. National Geophysical Data Center, NOAA*, 2009. doi: 10.7289/V5C8276M. [accessed 01-March-2019].

E. J. Anderson, A. J. Bechle, C. H. Wu, D. J. Schwab, G. E. Mann, and K. A. Lombardy. Reconstruction of a meteotsunami in lake erie on 27 may 2012: Roles of atmospheric conditions on hydrodynamic response in enclosed basins. *Journal of Geophysical Research: Oceans*, 120(12):8020–8038, 2015.

D. Basco and C. Klentzman. On the classification of coastal storms using principles of momentum conservation. In *Proc. 31st Int. Conf. on Coastal Eng.* ASCE, 2006.

A. J. Bechle and C. H. Wu. The lake michigan meteotsunamis of 1954 revisited. In *Meteorological Tsunamis: The US East Coast and Other Coastal Regions*, pages 155–177. Springer, 2014.

A. J. Bechle, C. H. Wu, D. A. Kristovich, E. J. Anderson, D. J. Schwab, and A. B. Rabinovich. Meteotsunamis in the laurentian great lakes. *Scientific reports*, 6:37832, 2016.

J. D. Chaytor, E. L. Geist, C. K. Paull, D. W. Caress, R. Gwiazda, J. U. Fucugauchi, and M. R. Vieyra. Source characterization and tsunami modeling of submarine landslides along the yucatán shelf/campeche escarpment, southern gulf of mexico. *Pure and Applied Geophysics*, 173(12):4101–4116, Dec 2016. ISSN 1420-9136. doi: 10.1007/s00024-016-1363-3. URL `https://doi.org/10.1007/s00024-016-1363-3`.

D. D. Churchill, S. H. Houston, and N. A. Bond. The daytona beach wave of 3–4 july 1992: A shallow-water gravity wave forced by a propagating squall line. *Bulletin of the American Meteorological Society*, 76(1):21–32, 1995. doi: 10.1175/1520-0477(1995)076⟨0021:TDBWOJ⟩2.0.CO;2.

B. Dugan and J. Stigall. Origin of overpressure and slope failure in the Ursa region, northern Gulf of Mexico. In D. C. Mosher, R. C. Shipp, L. Moscardelli, J. D. Chaytor, C. D. P. Baxter, H. J. Lee, and R. Urgeles, editors, *Submarine Mass Movements and Their Consequences*, pages 167–178. Springer Netherlands, 2010.

P. K. Dunbar and C. S. Weaver. *U.S. States and Territories National Tsunami Hazard Assessment: Historical Record and Sources for Waves*. U.S. Department of Commerce,

National Oceanic and Atmospheric Administration, National Geophysical Data Center Tech. Rep.No. 3, 2008.

G. Dusek, C. DiVeglio, L. Licate, L. Heilman, K. Kirk, C. Paternostro, and A. Miller. A meteotsunami climatology along the us east coast. *Bulletin of the American Meteorological Society*, 100(7):1329–1345, 2019.

M. Ewing, F. Press, and W. L. Donn. An explanation of the lake michigan wave of 26 june 1954. *Science*, pages 684–686, 1954.

E. L. Geist, J. D. Chaytor, T. Parsons, and U. ten Brink. Estimation of submarine mass failure probability from a sequence of deposits with age dates. *Geosphere*, 9(2):287–298, 2013.

H. P. Greenspan. The generation of edge waves by moving pressure distributions. *Journal of Fluid Mechanics*, 1(6):574–592, 1956.

S. T. Grilli, O.-D. S. Taylor, C. D. P. Baxter, and S. Maretzki. A probabilistic approach for determining submarine landslide tsunami hazard along the upper east coast of the United States. *Mar. Geol.*, 264:74–97, 2009.

C. B. Harbitz, F. Løvholt, and H. Bungum. Submarine landslide tsunamis: How extreme and how likely? *Nat. Hazards*, 72(3):1341–1374, 2014.

T. Hibiya and K. Kajiura. Origin of theabiki phenomenon (a kind of seiche) in nagasaki bay. *Journal of the Oceanographical Society of Japan*, 38(3):172–182, 1982.

C. W. Hirt and B. D. Nichols. Volume of fluid method for the dynamics of free boundaries. *J. Comput. Phys.*, 39:201–225, 1981.

J. Horrillo. *Numerical Method for Tsunami calculations using Full Navier-Stokes equations and the Volume of Fluid method*. PhD thesis, University of Alaska Fairbanks, 2006.

J. Horrillo, A. Wood, C. Williams, A. Parambath, and G. Kim. Construction of tsunami inundation maps in the Gulf of Mexico. Technical report, Award Number: NA09NWS4670006 to the National Tsunami Hazard Mitigation Program (NTHMP), National Weather Service Program Office, NOAA, 2011. avail. from http://www.tamug.edu/tsunami/NTHMP.html.

J. Horrillo, A. Wood, G.-B. Kim, and A. Parambath. A simplified 3-D Navier-Stokes numerical model for landslide-tsunami: Application to the Gulf of Mexico. *J. Geophys. Res.-Oceans*, 118:6934–6950, 2013. doi:10.1002/2012JC008689.

J. Horrillo, A. Pampell-Manis, C. Sparagowski, L. Parambath, and Y. Shigihara. Construction of five tsunami inundation maps for the Gulf of Mexico. Technical report, Award Number: NA12NWS4670014 and NA13NWS4670018 to the National Tsunami Hazard Mitigation Program (NTHMP), National Weather Service Program Office, NOAA, 2015. avail. from http://www.tamug.edu/tsunami/NTHMP.html.

J. Horrillo, W. Cheng, A. Pampell-Manis, and J. Figlus. Implementing nthmp-mms strategic plan in tsunami hazard mitigation products for the Gulf of Mexico. Technical report, Award Number: NA14NWS4670049 to the National Tsunami Hazard Mitigation Program (NTHMP), National Weather Service Program Office, NOAA, 2016. avail. from http://www.tamug.edu/tsunami/NTHMP.html.

J. Horrillo, W. Cheng, and J. Figlus. Development of four additional tsunami inundation maps with revision of Port Aransas, TX and updating existing ones with maritime products. Technical report, Award Number: NA15NWS4670031 and NA16NWS4670039 to the National Tsunami Hazard Mitigation Program (NTHMP), National Weather Service Program Office, NOAA, 2017. avail. from http://www.tamug.edu/tsunami/NTHMP.html.

J. Horrillo, W. Cheng, and J. Figlus. Development of two tsunami inundation maps in the GOM and inclusion of the USGS' Yucatan landslide tsunami sources. Technical report, Award Number: NA17NWS4670015 to the National Tsunami Hazard Mitigation Program (NTHMP), National Weather Service Program Office, NOAA, 2018. avail. from http://www.tamug.edu/tsunami/NTHMP.html.

J. Horrillo, W. Cheng, J. Figlus, and K. W. Development of two tsunami inundation maps in the GOM and inclusion of the Meteotsunami characterization for Panama City, FL. Technical report, Award Number: NA18NWS4670078 to the National Tsunami Hazard Mitigation Program (NTHMP), National Weather Service Program Office, NOAA, 2019. avail. from http://www.tamug.edu/tsunami/NTHMP.html.

J. L. Irish and D. T. Resio. A hydrodynamics-based surge scale for hurricanes. *Ocean Eng.*, 37:69–81, 2010.

L. Kantha. Time to replace the Saffir-Simpson hurricane scale? *Eos, Transactions American Geophysical Union*, 87(1):3–6, 2006.

W. Knight. Model predictions of Gulf and Southern Atlantic Coast tsunami impacts from a distribution of sources. *Sci. of Tsunami Hazards*, 24:304–312, 2006.

Z. Kowalik, W. Knight, T. Logan, and P. Whitmore. Numerical modeling of the global tsunami: Indonesian tsunami of 26 december 2004. *Science of Tsunami Hazards*, 23(1): 40–56, 2005.

Á. Linares, A. J. Bechle, and C. H. Wu. Characterization and assessment of the meteotsunami hazard in northern l ake m ichigan. *Journal of Geophysical Research: Oceans*, 121(9): 7141–7158, 2016.

M. Ličer, B. Mourre, C. Troupin, A. Krietemeyer, A. Jansá, and J. Tintoré. Numerical study of balearic meteotsunami generation and propagation under synthetic gravity wave forcing. *Ocean Modelling*, 111:38 – 45, 2017. ISSN 1463-5003. doi: https://doi.org/10.1016/j.ocemod.2017.02.001.

A. M. López-Venegas, J. Horrillo, A. Pampell-Manis, V. Huérfano, and A. Mercado. Advanced tsunami numerical simulations and energy considerations by use of 3D - 2D coupled models: The October 11, 1918, Mona Passage tsunami. *Pure Appl. Geophys.*, 172(6):1679–1698, 2015.

P. J. Lynett, J. C. Borrero, R. Weiss, S. Son, D. Greer, and W. Renteria. Observations and modeling of tsunami-induced currents in ports and harbors. *Earth and Planetary Science Letters*, 327:68–74, 2012.

P. J. Lynett, J. Borrero, S. Son, R. Wilson, and K. Miller. Assessment of the tsunami-induced current hazard. *Geophysical Research Letters*, 41(6):2048–2055, 2014.

S. Maretzki, S. Grilli, and C. D. P. Baxter. Probabilistic SMF tsunami hazard assessment for the upper east coast of the United States. In V. Lykousis, D. Sakellariou, and J. Locat, editors, *Submarine Mass Movements and Their Consequences*, pages 377–385. Springer Netherlands, 2007.

D. Masson, C. Habitz, R. Wynn, G. Pederson, and F. Lovholt. Submarine landslides: Processes, triggers and hazard protection. *Philos. Trans. R. Soc. A*, 364:2009–2039, 2006.

S. Monserrat, I. Vilibić, and A. B. Rabinovich. Meteotsunamis: atmospherically induced destructive ocean waves in the tsunami frequency band. *Natural Hazards and Earth System Science*, 6(6):1035–1051, Dec. 2006. URL `https://hal.archives-ouvertes.fr/hal-00299394`.

M. Olabarrieta, A. Valle-Levinson, C. J. Martinez, C. Pattiaratchi, and L. Shi. Meteotsunamis in the northeastern gulf of mexico and their possible link to el niño southern oscillation. *Natural hazards*, 88(3):1325–1346, 2017.

M. Orlić, D. Belušić, I. Janeković, and M. Pasarić. Fresh evidence relating the great adriatic surge of 21 june 1978 to mesoscale atmospheric forcing. *Journal of Geophysical Research: Oceans*, 115(C6), 2010.

A. Pampell-Manis, J. Horrillo, Y. Shigihara, and L. Parambath. Probabilistic assessment of landslide tsunami hazard for the northern Gulf of Mexico. *J. Geophys. Res.-Oceans*, 2016. doi:10.1002/2015JC011261.

C. B. Pattiaratchi and E. Wijeratne. Are meteotsunamis an underrated hazard? *Philosophical Transactions of the Royal Society A: Mathematical, Physical and Engineering Sciences*, 373(2053):20140377, 2015.

C. K. Paull, D. W. Caress, R. Gwiazda, J. Urrutia-Fucugauchi, M. Rebolledo-Vieyra, E. Lundsten, K. Anderson, and E. J. Sumner. Cretaceous–paleogene boundary exposed: Campeche escarpment, gulf of mexico. *Marine Geology*, 357:392–400, 2014.

C. H. Paxton and D. A. Sobien. Resonant interaction between an atmospheric gravity wave and shallow water wave along florida's west coast. *Bulletin of the American Meteorological Society*, 79(12):2727–2732, 1998.

J. Proudman. The effects on the sea of changes in atmospheric pressure. *Geophysical Journal International*, 2:197–209, 1929.

A. Rabinovich and S. Monserrat. Meteorological tsunamis near the balearic and kuril islands: Descriptive and statistical analysis. *Natural Hazards*, 13(1):55–90, 1996.

J. Šepić and I. Vilibić. The development and implementation of a real-time meteotsunami warning network for the adriatic sea. *Natural Hazards and Earth System Sciences*, 11(1): 83–91, 2011.

J. Šepić, L. Denis, and I. Vilibić. Real-time procedure for detection of a meteotsunami within an early tsunami warning system. *Physics and Chemistry of the Earth, Parts A/B/C*, 34 (17-18):1023–1031, 2009.

J. Šepić, I. Vilibić, and I. Fine. Northern adriatic meteorological tsunamis: Assessment of their potential through ocean modeling experiments. *Journal of Geophysical Research: Oceans*, 120(4):2993–3010, 2015.

L. Shi, M. Olabarrieta, A. Valle-Levinson, and J. C. Warner. Relevance of wind stress and wave-dependent ocean surface roughness on the generation of winter meteotsunamis in the northern gulf of mexico. *Ocean Modelling*, 140:101408, 2019.

L. Shi, M. Olabarrieta, D. S. Nolan, and J. C. Warner. Tropical cyclone rainbands can trigger meteotsunamis. *Nature communications*, 11(1):1–14, 2020.

U. S. ten Brink, H. J. Lee, E. L. Geist, and D. Twichell. Assessment of tsunami hazard to the U.S. East Coast using relationships between submarine landslides and earthquakes. *Mar. Geol.*, 264:65–73, 2009a.

U. S. ten Brink, D. Twichell, P. Lynett, E. Geist, J. Chaytor, H. Lee, B. Buczkowski, and C. Flores. Regional assessment of tsunami potential in the Gulf of Mexico. *U. S. Geol. Surv. Admin. Rep.*, 2009b.

I. Vilibić, N. Domijan, M. Orlić, N. Leder, and M. Pasarić. Resonant coupling of a traveling air pressure disturbance with the east adriatic coastal waters. *Journal of Geophysical Research: Oceans*, 109(C10), 2004.

I. Vilibić, K. Horvath, N. Strelec Mahović, S. Monserrat, M. Marcos, Á. Amores, and I. Fine. Atmospheric processes responsible for generation of the 2008 boothbay meteotsunami. *Natural Hazards*, 74(1):25–53, Oct 2014a. ISSN 1573-0840. doi: 10.1007/s11069-013-0811-y.

I. Vilibić, S. Monserrat, and A. B. Rabinovich. Meteorological tsunamis on the us east coast and in other regions of the world ocean. *Natural Hazards*, 74(1):1–9, Oct 2014b. ISSN 1573-0840. doi: 10.1007/s11069-014-1350-x.

P. Whitmore and B. Knight. Meteotsunami forecasting: sensitivities demonstrated by the 2008 boothbay, maine, event. *Natural Hazards*, 74(1):11–23, Oct 2014. ISSN 1573-0840. doi: 10.1007/s11069-014-1056-0.

R. Wilson, C. Davenport, and B. Jaffe. Sediment scour and deposition within harbors in california (usa), caused by the march 11, 2011 tohoku-oki tsunami. *Sedimentary Geology*, 282:228–240, 2012.

R. I. Wilson, A. R. Admire, J. C. Borrero, L. A. Dengler, M. R. Legg, P. Lynett, T. P. McCrink, K. M. Miller, A. Ritchie, K. Sterling, et al. Observations and impacts from the 2010 chilean and 2011 japanese tsunamis in california (usa). *Pure and Applied Geophysics*, 170(6-8):1127–1147, 2013.

Y. Yamazaki, Z. Kowalik, and K. F. Cheung. Depth-integrated, non-hydrostatic model for wave breaking and run-up. *Int. J. Numer. Meth. Fl.*, 61:473–497, 2008.